Title
Unraveling How Dysfunction of the Microglial Gene TREM2 Increases Risk for Alzheimer's Disease

Author
Sayed, Faten A.

Publication Date
2019

Unraveling How Dysfunction of the Microglial Gene TREM2 Increases Risk for Alzheimer's Disease

by
Faten Sayed

DISSERTATION
Submitted in partial satisfaction of the requirements for degree of
DOCTOR OF PHILOSOPHY

in

Neuroscience

in the

GRADUATE DIVISION
of the
UNIVERSITY OF CALIFORNIA, SAN FRANCISCO

Approved:

DocuSigned by:
Susanna Rosi
211375A844174DF...

Susanna Rosi
Chair

DocuSigned by:
Eric Huang
DocuSigned by:
Jonah Chan
DocuSigned by:
Li Gan
3FD674FAC03D4B3...

Eric Huang

Jonah Chan

Li Gan

Committee Members

Acknowledgements

Firstly, I would like to thank my parents and my sister, who have supported me throughout my life. My parents instilled a love of learning in me and always believed in me, seeing potential in me when I could not and encouraging me to try. I am grateful for my dad's advice throughout the years and for his sense of humor. I am grateful for my mom's optimism and gentleness which helped me weather the turbulent Ph.D. ride. My sister was always willing to listen to the ups and downs of graduate school, and celebrate milestones with me. I could always count on her to make me laugh. It is thanks to them and their belief in me that I was able to get to where I am today. Thank you so much!

I am incredibly grateful to my husband, Shafqat Ahmed. Thank you for helping me through this journey. I appreciate all the times you listened to me practice my talks, cheered me up after a long day, and celebrated successes with me. Thank you for seeing my strengths and encouraging me to believe in myself. Here's to starting a new journey with you and our two furballs, Moori and Mushmush!

I would also like to thank my Ph.D. advisor, Li Gan. I came in with a background in Psychology and little knowledge about Biology, and yet she took me in. Thank you for helping me understand the world of academia, for working with me on fellowships and manuscripts, and for teaching me how to read a paper with a sharp, skeptical mind. Thank you for giving me the opportunities to present at conferences, for teaching me to think through all the appropriate controls for each experiment, and for teaching me about figure aesthetics. When I was rotating, you informed that you have high expectations for your team, and that the lab only goes after high-risk, high-reward projects. In trying to meet these goals, I ventured outside of my comfort zone, working on a fast-paced, competitive project. As a result, I grew an incredible amount as a scientist. Thank you for helping me achieve more than I thought I could.

I am immensely grateful to all the current and past members of the Gan lab: Yungui Zhou, Peter Sohn, Chao Wang, Lihong Zhang, Tara Tracy, Maria Telpoukhosvkaia, Erica Delin, Yaqiao Li, David Le, Lay Kodama, Cindy Huang, Claire Clelland, Xu Chen, Meredith Chabrier Reichert, Seo-Hyun Cho, Michael Ward, Sakura Minami, Grietje Krabbe, Iker Itchegaray, Marcus Chin, Jesus Madero-Perez, Joe Udeochu, Annemiek Marschalk, and Lis de Weerd. You became a second family to me over the past six years. We celebrated birthdays and weddings, posed for silly photos at the Gladstone Holiday Party photobooth, sang our hearts out at the Gladstone Retreat karaoke, hosted board game nights, and tackled high-risk, high-reward projects together. I have so much to thank you for – it could be a dissertation on its own! I will try to keep it brief.

To the scientists who took me in when I knew the least. Meredith, Grietje, Seo-Hyun and Michael, you were my first mentors in the lab. You patiently stayed by my side as I learned and for that I am incredibly grateful. Michael, I dove right into the deep end of molecular biology learning cloning with you. Meredith, thank you for showing me the ropes during my rotation and for launching the Trem2 project that turned into my dissertation work. I am also grateful for your advice and support as I learned the basics. Grietje, thank you for teaching me everything you knew about microglia-specific techniques and for being such a jovial person. Seo-Hyun, thank you for letting me contribute to your project and for being my first mentor after I joined the lab.

To the research associates who keep the lab afloat. Yungui Zhou, you are the lab mom – so sweet and gracious with your time. You taught me so many lab techniques, always helped me track down items in the lab, and genotyped thousands of mice for me. You juggled so many experiments for different people in the lab so effectively. Thank you for always making the time to answer my questions and to ask me how I am doing. I will miss your sweet self! Yaqiao, you are a staining guru. I am so lucky to have learned from the best! Thank you for all the hours you spent mounting sections and discussing image analysis with me. I could always take comfort in knowing I could talk to you about the challenges of analyzing MC1 and AT8 staining. Thank you

for also teaching me how to do stereotaxic injections, for being my *in vivo* imaging buddy, and an overall board game aficionado. David, I do not know where to start! You taught me an immense amount about mouse work, from husbandry to how to extract the brain to how to perform behavioral assays and analyses. You are hands down the best perfusion buddy. I could always count on you to make the incredibly long perfusions fly by with all of your stories. You kept the lab running like a well-oiled machine, always making sure all the essentials were stocked, our protocols were up to date, and that everyone received a welcoming tour after joining the lab. Thank you for all the lab outings you coordinated, all the bagels you brought for lab meetings, all the mice that you weaned and tailed (seriously such a colossal effort!) and for being a hard-working, kind, and funny labmate. The first time I gave a talk in front of the entire institute was the year you were in charge of IT. As you clipped on my microphone, you told me I was going to do a great job and I felt a little less nervous. Thank you for always believing in me.

To the postdocs who patiently answered so many questions. Xu, thank you for teaching me all the western blot tips and tricks. You are an incredibly capable scientist. You work so meticulously and efficiently and I am so grateful I had the chance to work with you and learn from you. Chao, you have been with me from the beginning until the very end. You are so knowledgeable, able to execute and troubleshoot new protocols rapidly. Thank you for fielding all my tau questions over the years. I have learned an immense amount from you. Cindy, thank you for being there through the highs and lows. I miss our evening science chats. Joe and Jesus, I wish you could have joined the lab earlier so that I could have had more time with you two! It was so brief, yet so memorable. Joe, I am thankful for the calm demeanor you carried with you, and am in awe of your breadth of scientific knowledge. You are a careful, astute scientist and I know you will go far! Jesus, you are one of the jolliest scientists I have ever met. Your enthusiasm for science and life and your upbeat personality brought so much joy to the lab. Maria, thank you for being one of the first friends I made in the lab. We started around the same time, and went through the adventure of together and I am so grateful to have had you by

my side! I loved doing primary microglia cultures with you, working side by side in a tiny hood chatting about everything and anything. Thank you for helping me practice for my qualifying exam, and for celebrating with me afterwards. I miss our walks home, talking about life, Yale and science. Claire, I can always count on you to support me. Thank you for encouraging me to write my first manuscript, for helping me strategize the figure layout and where to submit it to you, and for editing it. Without you, the manuscript would not exist! Thank you for your kindness and comfort during the tough times, and for welcoming me into your home. You have such a zest for science and I know you will go far.

To the visiting students. Annemiek and Lis, you were breaths of fresh air! It was uplifting to have more graduate students in the lab, even for a short while. Annemiek, thank you for your friendship! Your openness and willingness to talk was just what I needed during that time.

To the admin. Erica, thank you for being so proactive and helpful over the years. I could always count on you to know or quickly find the answers to my questions. You are so thoughtful and considerate and have helped keep the lab running. You have helped me work through and solve so many problems, scientific and otherwise. I am so grateful for our friendship!

To the labmate turned best friend. Lay, I am immensely grateful to have had you as my lab partner-in-crime and friend these past few years. I admire your approach to science and life. You tackle new protocols fearlessly and confidently and quickly gain mastery – you have become our very own bioinformatics core! You bounce back from setbacks rapidly, overcome obstacles easily, and masterfully juggle so many projects both in the lab and outside of the lab. I have learned so much from you. You inspire me to be more easygoing and to face new projects with ease. Thank you for your willingness to laugh at my jokes and listen to my struggles. It has been incredibly fun working with you on part of this dissertation; I really enjoyed having you to bounce ideas off of and discuss science with. But most of all, I am thrilled to have you as a friend! You are brilliant, and I know you will go far.

I would like to thank my mentees, Axel Hauduc, Emeline Kao, Emily Davis, and Jessie King. Teaching and mentoring fills me with incredible joy, and thanks to all of you, I had the opportunity to mentor throughout my years as a graduate student. I'd like to especially highlight Emily and Axel. Emily, you embarked on the Trem2 journey with me in its infancy – thank you. Axel, you were the first undergraduate student I mentored. I learned an incredible amount about mentoring and science by working with you and am thankful for the work that you did for my dissertation.

I am also incredibly grateful to my thesis committee members Jonah Chan, Susanna Rosi, and Eric Huang. Thank you for telling me when it was time to wrap up! I remember last year when you all mentioned I had enough to graduate. I felt so shocked, and so touched that three brilliant scientists felt I had met expectations. It is hard to shake off imposter syndrome, but those moments of positive feedback and support are incredibly powerful and reassuring, thank you. Eric Huang was instrumental in teaching me how to write a strong grant. Jonah Chan and Susanna Rosi were pillars of support, always willing to chat about science and life and cheer me on through the graduate school roller coaster ride. Jonah, thank you for all the advice you provided over the past few years and for being so easily accessible and willing to talk. Susanna, seeing the way you juggle your family and your lab so skillfully, and the joy you bring to those around you is inspirational. I would also like to thank Felice Dunn for being her intelligent, kind self and for taking me on as an unofficial mentee over the past few years, offering wonderful professional and scientific guidance. Moreover, I am grateful to the broader UCSF Neuroscience community who has supported me over the past few years, especially program administrators Pat Veitch and Lucita Nacionales, as well as Susan Voglmaier and Kaveh Ashrafi.

I would like to acknowledge my classmates and friends in the Neuroscience program. I'd like to highlight John Lin King, Hung Lin King, Lynn Wang, and Mario Zubia. We embarked on this adventure together and having your friendship and support over the years were

instrumental in helping me get this far. Thank you for all the home-cooked meals and beautiful desserts, for the long hours spent talking about anything and everything, for all the rides down to Asilomar and trips to conferences together, and for all the life milestones we celebrated together. You all made my Ph.D. experience fun and as painless as it could be. Thank you so much!

This work was supported by the J. David Gladstone Institute and the National Institutes of Health.

Contributions

Chapters 1, 4 and **5** of this dissertation were written by Faten Sayed.

Chapter 2 of this dissertation is reproduced in its entirety from:

> Sayed, F.A., Telpoukhovskaia, M., Kodama, L., Li, Y., Zhou, Y., Le, D., Hauduc, A., Ludwig, C., Gao, F., Clelland, C., Zhan, L., Cooper, Y.A., Davalos, D., Akassoglou, K., Coppola, G., Gan, L. (2018). Differential effects of partial and complete loss of TREM2 on microglial injury response and tauopathy. PNAS 115: 10172-10177.

Author Contributions: F.A.S. and L.G. designed the experiments; F.A.S., Y.Z., D.L., A.H., and D.D. performed research; M.T., C.L., L.Z., Y.A.C., K.A., and G.C. contributed new reagents/analytic tools; F.A.S., M.T., L.K., Y.L., A.H., F.G., and L.G. analyzed data; and F.A.S., C.C., and L.G. wrote the paper.

Chapter 3 of this dissertation was written by Faten Sayed, Lay Kodama, and Li Gan. The manuscript is in preparation for submission. Author Contributions: L.G. and F.A.S conceived and planned experiments. F.A.S., L.K. J.U., T.T., and L.G. designed experiments. F.A.S., L.K., J.U., D.L., H.M., X.J., L.M., Q.L., L.Z., and T.T. did experiments. L.K., H.M., Q.L., L.Z., X.N., L.M., F.G., M.T., Y.M.L., G.F., G.C., and L.H.T. contributed experimental and analytical tools. F.A.S., L.K., D.L., T.T., H.M., F.G., M.T., and X.N. analyzed data. J.H. provided human samples. Y.Z. and Y.Q.L. helped maintain the mouse colony. F.A.S., L.K., and L.G. wrote the manuscript with input from all other authors.

Unraveling How Dysfunction of the Microglial Gene TREM2 Increases Risk for Alzheimer's Disease

Faten Sayed

Abstract

A heterozygous single amino acid change in the *TREM2* gene significantly increases risk for developing late-onset Alzheimer's Disease (AD). In the brain, *Trem2* is uniquely expressed by microglia, strongly implicating microglia in AD pathogenesis. Trem2 is a receptor with numerous ligands and pleiotropic functions ranging from phagocytosis to inflammation and synapse pruning. There has been a significant amount of research on the consequences of Trem2 deficiency in amyloid mouse models. Trem2-deficient mice exhibit reduced microglial clustering around amyloid-beta plaques and reduced levels of inflammatory transcripts. The consequence of Trem2 deficiency in the context of tau pathology, on the other hand, is not well understood. To address this gap, we investigated the effects of *Trem2* haploinsufficiency and deficiency on microglial function in the healthy brain and in the context of tauopathy. We found that removing one copy of *Trem2* significantly impaired microglia's ability to respond to injury *in vivo* to a greater extent than removing both copies of *Trem2*. Moreover, *Trem2* haploinsufficient mice exhibited an increase in tau load, whereas tau load in *Trem2* deficient mice was unimpacted or slightly reduced. The increase in tau load in *Trem2* haploinsufficient mice correlated with increased levels of pro-inflammatory transcripts and neurodegeneration. *Trem2* deficient mice, on the other hand, exhibited reduced levels of pro-inflammatory transcripts and less neurodegeneration. To determine how a single amino acid change in *TREM2* increases risk for AD, we used CRISPR to generate two novel mouse models expressing one copy of wild-type or R47H human *TREM2* (R47H-hTREM2) driven by the endogenous mouse *Trem2* promoter. We found that R47H-hTREM2 caused aberrant hippocampal synaptic transmission

and impaired spatial memory. In the context of tauopathy, it exacerbated spatial learning and memory as well, and resulted in higher levels of pro-inflammatory and disease-associated microglial transcripts. Moreover, R47H-hTREM2 microglia caused transcriptional changes in neurons and oligodendrocytes, pertaining to metabolism and oxidative phosphorylation. Lastly, there was significant overlap between our R47H-hTREM2 mouse model and AD patients with the R47H mutation. The most significant overlap was in oligodendrocyte transcripts related to mitochondrial dysfunction and oxidative phosphorylation. In sum, the work highlighted in this dissertation highlights how losing one copy of a gene can be more detrimental than losing both copies and how a single amino acid change in one cell type in the brain can have widespread non-cell autonomous ramifications resulting in cognitive deficits. Hopefully, the pathways highlighted in this work can help guide the development of therapeutic strategies targeted at microglial dysfunction in AD.

Table of Contents

List of Figures

Chapter 2

Chapter 3

Chapter 1: Introduction

1.1 Human Genetics Studies Implicate Microglia in Alzheimer's Disease Pathogenesis

Alzheimer's disease (AD) is the most common form of dementia in elderly patients. 5.8 million Americans are currently suffering from the disease and every 65 seconds, someone in the United States develops AD[1]. It is currently the 6th leading cause of death in the U.S. and costs the nation $290 billion, most of which is due to the billions of hours that caregivers work to take care of seniors with AD[1]. Given these alarming facts, it is critical to identify therapeutics that slow or even halt disease progression.

Alzheimer's disease is a neurodegenerative disorder identified neuropathologically by the presence of two abnormal protein aggregates: extracellular amyloid-beta plaques and intraneuronal tau tangles. In addition, AD is also characterized by increased activation of microglia, the immune cells in the brain[2]. This aberrant microglial phenotype was largely considered a response to the buildup of protein aggregates, and not a cause of disease. However, recent human genetics studies have shifted the paradigm in the field, highlighting microglia as causal factors in pathology.

Microglia, as the brain's immune cells, are tasked with constantly surveying the brain[3,4] for damage or pathogens. They are phagocytic, eliminating debris and under-utilized synapses[5-9]. Unlike other brain cells which arise from neuroepithelial progenitors, microglia come from hematopoietic stem cells in the primitive yolk sac[10,11] and replenish their numbers through self-renewal[12], as opposed to other myeloid cells which are renewed by monocytes circulating in the blood.

In AD brain tissue, microglia are found surrounding amyloid-beta plaques. Their proximity to the plaques led to the hypothesis that microglia are clearing up the aggregates and limiting their spread. Indeed, portions of the plaques that are not covered by microglial

processes are less compact and are associated with greater axonal dystrophy[13]. While this suggests that microglia are attempting to protect the brain, recent genome-wide association studies have identified numerous microglial genes that, when mutated, increase risk for late-onset AD (LOAD)[14-18]. These findings move microglia from the sidelines into the spotlight, as they suggest that aberrant microglial function can increase susceptibility to disease, and even contribute to AD pathogenesis.

1.2 Trem2 Expression Pattern and Localization in the Brain

While ~1-5% of patients develop early-onset AD due to mutations in the genes *APP, PSEN1*, and *PSEN2*, the majority of AD patients develop sporadic, late-onset AD. The strongest and most common genetic risk factor is the E4 allele of apolipoprotein E (ApoE4), with an odds ratio of 3-4[19,20]. Aside from ApoE4, which was identified back in 1993, the field lacked strong genetic handles on the disease – until 2013. In 2013, researchers identified the strongest immune gene risk factor to date: *TREM2*[17,18]. A heterozygous single amino acid change from an arginine to a histidine at position 47 (R47H) is associated with a 2-4-fold increase in risk for developing late-onset AD[17,18,21]. This increase in risk is comparable to that of ApoE4 heterozygosity. While the R47H-TREM2 variant is incredibly rare, its high odds ratio suggests that it regulates microglial functions that may be key to unlocking microglia's role in disease pathogenesis.

Triggering receptor expressed on myeloid cells-2 (Trem2) is a single-transmembrane receptor, consisting of a signal peptide (residues 1-18), an ectodomain that can be cleaved and shed from the cell surface as soluble TREM2 (sTrem2) (residues 19-174), a transmembrane domain (residues 175-195), and a short, cytoplasmic tail (residues 196-23). It requires an adaptor protein, DNAX-activating protein of 12 kilodaltons (Dap12), to stabilize Trem2 on the

cell surface and initiate a signaling cascade[22]. Trem2 was initially discovered through a screen for receptors that would induce cell surface expression of Dap12 on macrophages[23].

Trem2 is only found on cells from the myeloid lineage. In the periphery, Trem2 is expressed by osteoclasts, dendritic cells and macrophages[24]. TREM2 expression was found on macrophages infiltrating tissue, but not on peripheral blood cells or bone marrow cells, suggesting that its expression may be stimulated by cytokines or by the transition from the periphery into tissues[25]. In the brain parenchyma, Trem2 expression is restricted to microglia[26-29]. Of note, baseline Trem2 protein expression in the healthy brain appears to be quite low. Trem2 expression was undetectable using immunohistochemistry in adult mouse tissue[30]. Using a Trem2-GFP reporter mouse, it was found that only 5.8% of cortical microglia and 8.7% of hippocampal microglia expressed Trem2[31]. On the other hand, 95-97% of microglia are positive for Trem2 when stained in culture or sorted using fluorescence-activated cell sorting (FACS)[26,27], suggesting that stressful conditions that activate microglia, such as being cultured or sorted, can increase Trem2 levels. While Trem2 expression has been found on neurons in both mouse and human tissue[32], it is now believed that this is due to sTrem2 binding to neurons[33], and not due to neuronal production of Trem2. The nuclei of Trem2+ neurons do not appear pyknotic or fragmented[33], suggesting that sTrem2 binds to healthy neurons. Moreover, neuronal sTrem2 staining is very minimal in healthy mice, but increases significantly in amyloid mouse models[33]. Its function in neurons remains unknown. In sum, Trem2 mRNA and protein are restricted to microglia in the healthy mouse brain, albeit at low levels, and Trem2 ectodomain staining is also found on neurons in an AD mouse model. Trem2 expression is context-specific, increasing under stressful conditions or after cells infiltrate tissue.

Trem2 mRNA may be differentially expressed across brain regions. In healthy human brain tissue, Trem2 mRNA is higher in white matter than in gray matter, and high expression levels can be found in the corpus callosum, medulla, hippocampus, thalamus, and basal ganglia[24,34]. In the healthy mouse brain, Trem2 expression appears to be developmentally-

regulated. The highest expression occurs early on and by postnatal day 10, staining for Trem2 can only be found in the corpus callosum[35]. However, western blot of 6-week-old mice identified high Trem2 protein levels in the hippocampus[32], suggesting that staining may not be sensitive enough to detect the already low levels of Trem2 in the healthy brain. Overall, these studies suggest that Trem2 expression is not uniformly distributed across the brain, with highest expression in the white matter over the gray matter, and more specifically, in the corpus callosum, basal ganglia, hippocampus, medulla and thalamus.

1.3 Trem2 Exhibits Pleiotropic Functions in the Healthy Brain

Trem2 binds numerous ligands: bacteria, lipids, healthy and apoptotic neurons, anionic ligands, apolipoproteins, and amyloid-beta[26,33,36-45]. Its *in vivo* ligands remain unknown, though Apoe may be one of them. Out of its numerous ligands, its role as a lipid sensor has taken center stage in AD research due to the accumulation of lipids around plaques. Trem2 signaling is stimulated by negatively charged phospholipids that associate with amyloid-beta plaques, membrane phospholipids exposed by dying neurons, and anionic non-phosphate lipids released by damaged myelin[41,45], all of which are found in disease states.

Alongside its role as a lipid sensor, Trem2 also promotes microglial chemotaxis[46-48]. Stimulation of Trem2 in primary microglia promotes their migration towards chemokines, and Trem2 deficiency impairs microglia's ability to migrate toward dying tissue *in vitro* and *in vivo*[46-48]. It is hypothesized that Trem2 binds lipids and signals to microglia to move towards the lipid-dense region, such as an amyloid plaque. Indeed, Trem2-deficient microglia show impaired migration towards amyloid-beta *in vitro*[44].

Trem2 is a phagocytic receptor. Expression of Trem2 is sufficient to induce phagocytosis in non-phagocytic cells, such as Chinese Hamster Ovary cells[49]. Trem2 stimulation increases F-actin levels, a critical part of the phagocytic process, and promotes

phagocytosis of apoptotic neurons by primary microglia[27]. However, loss of Trem2 does not always impair phagocytosis. In the absence of any other mutation, Trem2 knockout primary microglia phagocytose amyloid-beta normally[50]. When amyloid-beta is lipidated, though, Trem2-knockout primary microglia exhibit impaired uptake and degradation[42], indicating that Trem2 may be especially critical for lipid-related phagocytosis. Moreover, when microglia are activated, such as in an amyloid mouse model, Trem2 may not be necessary for phagocytosis. Trem2 knockdown reduces phagocytosis of apoptotic neurons in primary microglia[27]. However, Trem2 knockout microglia from an amyloid mouse model phagocytosed apoptotic cells just as well as Trem2 wild-type microglia from the same amyloid mouse model[41]. These contradictory findings suggest that in highly activated microglia, such as in the context of amyloid pathology, other phagocytic receptors may be upregulated and able to compensate for the lack of Trem2. In sum, while stimulation of Trem2 promotes phagocytosis, and expression of Trem2 is sufficient to confer phagocytic capability, Trem2 may not be required for phagocytosis, particularly when microglia are activated.

In addition to promoting phagocytosis, Trem2 also promotes proliferation[41,45,51-53]. Microglia are highly proliferative cells, increasing in number during disease states and during aging[54]. Trem2 knockout and Trem2 wild-type microglia start off at similar densities in the mouse brain at 0.5 years of age. In wild-type mice, the number of microglia doubles by 2 years of age. In Trem2 knockout mice, though, the number of microglia stays the same from 0.5-2 years of age, suggesting impaired proliferation[45]. A similar phenomenon of blunted proliferation with age is seen in Trem2-deficient microglia in an amyloid mouse model[55]. Indeed, there are fewer BrdU+ microglia in Trem2-knockout mice, further indicating impaired proliferation[52].

In addition to age, Trem2 knockout microglia also show a blunted response to other challenges, such as treatment with cuprizone or kainic acid. Cuprizone is a copper-chelating agent that produces demyelination in the brain. During treatment with cuprizone, wild-type microglia quadruple in number, then return to baseline numbers during recovery. Trem2

knockout microglia, on the other hand, only double in number and stay at that level even during recovery[45]. Trem2 knockout microglia also exhibit blunted proliferation in response to kainic acid, which induces excitotoxity and neuronal death[56]. In sum, Trem2 promotes microglial proliferation in response to stimuli. In its absence, microglia proliferate less, which may impede recovery from the challenge.

Trem2's role in cell proliferation may be mediated, in part, by regulation of the Wnt signaling pathway. The majority of Trem2-deficient microglia are in the G0/G1 phase of the cell cycle, with few microglia in S phase, suggesting cell cycle arrest[52]. Trem2 is thought to promote survival by stabilizing ß-catenin, a key part of the Wnt signaling pathway[52]. However, Wnt activation does not fully rescue the proliferation deficits seen in Trem2 knockout microglia[52], suggesting that there are other pathways at play that remain to be identified.

In addition to promoting cell proliferation, Trem2 also stimulates cell survival. Trem2 knockout plaque-associated microglia have increased TUNEL staining compared to Trem2 wild-type microglia surrounding plaques, suggesting increased apoptosis[41,55]. A key regulator of microglia survival is the CSF1 ligand secreted by neurons, which binds to CSF1R on microglia[57]. Trem2 promotes microglial survival under conditions of limited CSF1; in Trem2's absence, microglia viability is severely reduced[41]. One hypothesis in the field is that CSF1 levels may be limited in plaque-dense areas, thus making Trem2-deficient microglia less fit to survive and consequently, less able to respond to the injury.

Trem2 was recently implicated in developmental synapse pruning. Neurons from Trem2-deficient mice (aged postnatal day 18-20) exhibit an increase in miniature excitatory postsynaptic current (mEPSC) frequency in the hippocampus, and an increased density of synaptic markers PSD95 and VGLUT1[58]. This was due to a non-cell autonomous effect of Trem2-deficient microglia on neurons, as wild-type neurons co-cultured with Trem2 knockout microglia also show aberrant synaptic transmission, while synaptic transmission is normal in Trem2 deficient neurons. However, in slightly older (1-month-old) mice, Trem2-deficiency

results in a reduction in mEPSC frequency and PSD95 levels in the same region of the hippocampus[59]. It is possible that Trem2's effect on synaptic transmission is age-dependent. However, aged Trem2-deficient mice exhibit an increase in PSD95[60], similar to the findings in mice aged postnatal day 18-20. While these studies indicate that Trem2 can regulate synapse pruning, future studies are needed to determine how it regulates synapse pruning throughout a mouse's lifetime.

Trem2 has been implicated as a regulator of inflammation, albeit with conflicting results. Classically, Trem2 in the periphery is considered anti-inflammatory, as stimulating Trem2 macrophages *in vitro* increases levels of anti-inflammatory transcripts[25]. However, *in vivo* in the brain, Trem2 may be pro-inflammatory, as Trem2 knockout mice express reduced levels of pro-inflammatory cytokines in the aging brain and in amyloid and tau mouse models[46,55,60,61]. *In vivo*, Trem2 may be needed to promote microgliosis, or the activated state of microglia, in response to a stimulus. Through RNA-sequencing, multiple studies have found that Trem2-deficient microglia fail to mount the typical pro-inflammatory response to amyloid pathology, and instead seem frozen in a homeostatic state[41,47,62]. Indeed, this dichotomy between *in vivo* versus *in vitro* effects of Trem2 on inflammation can be seen in one study by Wang *et al*. *In vitro*, Trem2 knockout primary microglia exhibited increased levels of pro-inflammatory transcripts in response to lipopolysaccharide, suggesting that Trem2 is anti-inflammatory. However, *in vivo* in an amyloid mouse model, Trem2-deficient microglia's transcriptome resembled that of non-transgenic microglia, suggesting that Trem2 is pro-inflammatory[41]. The reason behind this context-dependent effect of Trem2 on inflammation remains unknown.

1.4 Complex Effects of Trem2 Deficiency in the Context of Amyloid Pathology

Trem2 mutations have been implicated in several neurodegenerative disorders[63-66]. Loss of Trem2 function causes Nasu-Hakola disease, a rare pre-senile dementia associated with

bone cysts[34]. Interestingly, the corpus callosum and basal ganglia are especially impacted in these patients[67], which may be related to Trem2's high expression levels in these two brain regions[24,34]. These patients also exhibit demyelination, axon loss, cerebral atrophy and microgliosis – predominantly in the white matter[34,67]. These patients do not have any intraneuronal or glial inclusions, but do exhibit white matter lesions[67], which has led to a theory of failed lipid metabolism underpinning this symptom[68]. Interestingly, 2-year-old Trem2 knockout mice do not show any hallmarks of Nasu-Hakola disease[45], indicating that knocking out Trem2 in mice is not sufficient to induce this disease as it is in humans.

Based on Trem2's causal role in Nasu-Hakola disease, pioneering work on Trem2 in the mouse brain started with demyelination experiments. Cuprizone treatment results in similar levels of demyelination in Trem2 wild-type and knockout mice 4 weeks into treatment. However, 12 weeks into treatment, the corpus callosum of wild-type mice started showing signs of remyelination, while the corpus callosum in Trem2 knockout mice remained largely demyelinated[45]. This suggests that while Trem2 does not impact initial demyelination, it may play a role in remyelination. Indeed, as noted previously, microglia from Trem2-deficient mice are unable to proliferate to the same extent as wild-type microglia, which may limit their ability to respond to the challenge and clean up myelin debris to allow for remyelination. This phenotype of prolonged demyelination led to the hypothesis of Trem2 as a lipid sensor, which has now been validated by multiple labs.

Since 2013 when Trem2 was identified as a strong risk factor for AD, numerous mouse studies have investigated Trem2's role in amyloid pathology. There have been two reproducible finding across mouse models and across different ages of mice: (1) reduced clustering and proliferation of microglia around plaques, which is seen in both Trem2 haploinsufficient and Trem2 deficient mice[30,41,55,69,70] and (2) reduced intensity of Iba1 (a microglial marker) in Trem2 deficient mice[41,46,61].

The reduction in microglial clustering around plaques is observed early on, at 4 months of age in the 5xFAD amyloid mouse model[55]. While overall microglia number is no different between wild-type and Trem2-deficient mice, Trem2-deficient microglia exhibit reduced Ki67+ staining and increased TUNEL staining and around plaques, suggesting impaired proliferation and increased apoptosis, respectively[41,55,70]. One theory behind the reduction in plaque-associated microglia in Trem2 knockout mice pertains to CSF1R signaling. As mentioned previously, CSF1 levels may be limited around plaques. Since Trem2 signaling is necessary for survival under low CSF1 conditions[41], Trem2-deficient microglia may be less able to survive, let alone proliferate, around plaques.

Trem2-deficient mice also show an increase in plaque area that is not covered by microglial processes[70]. Notably, the reduction in the number of microglia around plaques is not large enough to explain this reduction in plaque surface coverage by microglial processes[70]. Upon closer inspection, Trem2-deficient microglial processes appear to have more loops, instead of being fully extended around plaques[70]. This indicates that the reduction in plaque coverage may be due to an impairment in Trem2-deficient microglia's ability to extend their processes towards the plaques. Indeed, early work in the field showed that stimulating Trem2 increases F-actin levels[27]. In the absence of Trem2, microglia may be less able to mobilize actin in order to extend their processes towards the plaques. However, this does not explain why Trem2-deficient microglial processes have more loops, which suggests an inability to organize microtubules linearly to reach the plaque.

Oddly, overexpression of Trem2 using a bacterial artificial chromosome (BAC) also reduced microglia clustering around plaques[31]. This surprising finding may suggest that microglia are very sensitive to Trem2 levels – too much or too little and they are unable to function properly in certain contexts. In sum, Trem2-defiicent microglia around plaques exhibit reduced clustering, reduced proliferation and increased apoptosis, potentially due to impaired

CSF1-CSF1R signaling. They also have fewer processes covering the plaques, possibly due to an impaired ability to recruit actin or organize the microtubules for cytoskeletal rearrangements.

In addition to impaired proliferation and survival, Trem2-deficient microglia in an amyloid mouse model also exhibit increased autophagy[71]. Importantly, this is also true for human AD patients with TREM2 risk variants[71]. Autophagy typically signals an adaptive response to stress that occurs when cells are unable to meet an increased demand for energy and protein synthesis. Multiple lines of evidence support reduced energetics in Trem2-deficient mice. Mammalian target of rapamycin (mTOR) signaling promotes energetic and anabolic metabolism, cell growth and proliferation. In an amyloid mouse model, Trem2-deficient mice exhibit reduced mTOR activation[71], suggesting reduced energetics. Secondly, Trem2-deficient mice demonstrate increased catabolism and reduced ATP levels under low CSF1 conditions[71]. Lastly, they have reduced mitochondrial mass[71]. Whether the deficiency in mTOR signaling, reduced mitochondrial mass, and low levels of ATP all occur prior to the increase in the number of autophagic vesicles is unclear. However, treatment with cyclocreatine, a creatine analog that can generate a long-acting phosphagen to sustain ATP levels during high energy demands, reduced the number of autophagic vesicles in microglia and dystrophic neurites around plaques, doubles microglial density around plaques, and reduces apoptotic markers in microglia[71]. This suggests that correcting the metabolic deficiency in Trem2 knockout mice can rescue certain pathological phenotypes. The authors hypothesize that Trem2-deficient microglia under stress upregulate apoptotic markers because they lack Trem2-dependent survival signals that typically compensate for the stressed state. Trem2 may be pivotal for microglial functioning by helping to prevent a dysfunctional, low-energy state brought on by disease or stress.

In addition to impaired microglial clustering around plaques in Trem2-deficent mice, the other reproducible finding in the field is reduced Iba1 intensity. The reduction in Iba1 intensity in Trem2-deficient mice suggests reduced microglial activation. Indeed, RNA-sequencing studies have reproducibly found that loss of Trem2 in amyloid mouse models shifts the microglial

transcriptome towards that of purely wild-type microglia. Trem2 deficiency reduces expression of pro-inflammatory transcripts and increases expression of homeostatic transcripts[41,47,62,72]. These results suggest that Trem2 is required for microglial activation; in its absence, microglia are trapped in a homeostatic transcriptional state.

While it is evident that Trem2 regulates microglial proliferation, survival, and inflammatory state, Trem2's effect on amyloid plaque load remains under debate. Some studies find that Trem2 deficiency reduces plaque load[30,55], while others have noticed an increase in plaque load[41,51], or no difference in total plaque load[69]. These contradictory findings may be due to differential effects of Trem2 over the course of the disease. Early on, Trem2 deficiency reduces plaque load[30,55], while later on in the disease, Trem2 deficiency increases plaque load[41,51]. This hypothesis does not explain one study that found no difference in plaque area at early or late stages of disease[69], though.

An alternative, or additional, explanation for the discrepancies may be the type of antibody used to label plaques. Trem2 haploinsufficient and Trem2 deficient mice have a different proportion of compact versus filamentous plaques[70]. These different types of plaques are labeled with different antibodies or have different appearances when stained with the same antibody (such as a dense core versus a diffuse core). A careful profiling of these different types of plaques identified that Trem2 deficient mice have more filamentous plaques, and these plaques are associated with increased neuritic dystrophy early on, even prior to any differences in overall plaque load[55,70]. This was also observed in human AD patients with the R47H-TREM2 variant[70]. These findings indicate that Trem2 may play a role in plaque compaction. Microglia are thought to form a physical barrier around plaques, limiting the expansion of the plaques and the extent of damage to nearby neurons[13]. In amyloid mouse models, Trem2 expression is polarized, with expression highest on the leading edges of microglial processes that are directly contacting plaques[70]. Thus, Trem2 may promote microglial compaction of plaques into dense

cores that are less toxic. Reporting plaque morphology in addition to overall plaque number may help disambiguate Trem2's role in plaque load.

Overall, these findings show how Trem2's basic functions regulating microglial survival, proliferation, cytoskeletal rearrangements, and inflammatory state go awry in its absence during disease. Given Trem2's pleiotropic beneficial functions, could increasing Trem2 levels in amyloid mouse models improve pathology? Overexpression of Trem2 in an aggressive amyloid mouse model reduces plaque area and the number of dystrophic neurites[31]. Surprisingly, it also reduces Iba1 intensity and the number of microglia around plaques[31]. The reasons behind these counterintuitive findings remain unknown. Increasing soluble Trem2 levels in the same amyloid mouse model is also beneficial. It reduces plaque load and neuritic dystrophy overall, while improving long-term potentiation[56]. It also increases levels of pro-inflammatory transcripts and the number of plaque-associated and Ki67+ microglia[56]. These advantageous effects of sTrem2 require microglia, as microglia depletion along with sTREM2 treatment does not show these benefits, neither does treating primary neuronal cultures directly with sTREM2[56].

In sum, Trem2 deficiency increases plaque load in late stages of disease, alters plaque morphology from compact to filamentous, increases neuritic dystrophy, reduces inflammation, and impairs microglia survival and proliferation. Of note, the bulk of these studies focused on complete loss of Trem2, which is causal for Nasu-Hakola disease. It is Trem2 heterozygosity that increases risk for AD. The few studies that included Trem2 haploinsufficient mice found that they either behaved like wild-type mice, or had an intermediate phenotype between wild-type and Trem2-knockout mice[41,55,69,73].

1.5 Complex Effects of Trem2 Deficiency in the Context of Tau Pathology

Alzheimer's disease consists of both amyloid and tau aggregates. However, only three studies to date, including the next chapter of this thesis, have focused on Trem2's role in

tauopathy. Similar to amyloid pathology, there is also controversy over Trem2's role in tau pathology, which may be attributed to the different mouse models used. One study used a mouse model that expresses wild-type human tau and found that Trem2 deficiency worsens tau pathology[74]. Another study that used a mouse model expressing mutant human tau found that Trem2 deficiency has no effect on tau pathology, but instead reduces neurodegeneration, increases synapse density and reduces gliosis[61]. Whether these contradictory findings are due to the presence of mutant versus wild-type tau, or the different stages at which these mice were analyzed is unclear. In the presence of mutant human tau, though, both we and others find that Trem2-deficiency is beneficial, unlike its detrimental role in amyloid mouse models.

Trem2 is not the first protein to show divergent effects on amyloid and tau pathology. Deletion of CX3CR1, the microglial chemokine receptor for CX3CL1, reduces amyloid plaque load but exacerbates tau pathology[75]. These differential effects of microglial proteins on amyloid and tau may be because of the temporal differences in when these aggregates manifest: amyloid appears early on in the disease, while tau appears later. Thus, microglia's putative beneficial response to amyloid plaques may prime them to be more neurotoxic once tau pathology appears. Alternatively, localization of these protein aggregates may explain the differential effect of microglia: amyloid plaques are extracellular, while tau is intraneuronal. Thus, microglia likely interact with these aggregates using different mechanisms. Microglial inflammation may be helpful in clearing out extracellular aggregates, but toxic when dealing with neuronal aggregates. Pro-inflammatory molecules can be neurotoxic, particularly in cases of chronic inflammation[76]. Since Trem2 deficiency reduces inflammation *in vivo*, this may explain why it is beneficial for dealing with intraneuronal tau pathology.

As mentioned before, Trem2 haploinsufficiency is associated with increased AD risk. Yet no studies thus far have looked at Trem2 haploinsufficiency's effect on tau pathology. To address this gap in the field, we used the mutant tau mouse model (P301S) expressing both,

one or no copies of Trem2 and investigated the consequences on microgliosis and tauopathy. These findings were published in *PNAS* in 2018 and can be found in chapter two of this thesis.

1.6 R47H-Trem2 Impairs Ligand Binding

Thus far, studies have focused on loss of Trem2 to understand its role in microglial function in health and disease. However, the heterozygous R47H variant of Trem2 is what increases risk for AD[17,18]. More recently, the field has moved into addressing the consequences of this point mutation on Trem2 function.

R47 is located on the protein surface in the ligand-binding area of the ectodomain[40]. Overall, *in vitro* studies find that R47H reduces ligand-binding[36,37,40-42,44,77,78]. This phenotype is unlike mutations causal for Nasu-Hakola Disease, which are found buried within the protein and impact protein folding and stability, resulting in reduced protein expression at the cell surface [40]. Moreover, while Nasu-Hakola disease mutations are unable to bind lipoproteins, R47H still exhibits some binding and uptake[42]. This aligns with the fact that the R47H mutation increases risk for AD, while the Nasu-Hakola Disease mutations are causal for disease and therefore are expected to have more severe phenotypes. Of note, phosphatidylcholine and sphingomyelin, which were found to activate a Trem2 reporter cell line the most effectively out of all lipids tested[41], still bind to R47H almost as effectively as wild-type Trem2[41,78]. These two lipids may have an especially strong affinity for Trem2, such that the mutant form is still able to bind them. Or, they may have a different binding pocket in the protein that is not impacted by R47H. Since R47H can bind some lipids, it may retain some functionality and is therefore likely only a partial loss-of-function mutation.

Aside from reduced ligand binding, R47H-Trem2 behaves similarly to wild-type Trem2, exhibiting weak or no phenotype with respect to impairments in sTrem2 shedding, Trem2 maturation, and phagocytosis[40,50,79]. R47H-Trem2 has similar cell surface expression as wild-

type, it does not accumulate intracellularly in the endoplasmic reticulum like known loss-of-function Trem2 mutations, and is able to phagocytose bacteria normally (though it is impaired in bead phagocytosis, suggesting that its impairments may be substrate-specific)[50]. There are conflicting results regarding its effect on the secretion of soluble Trem2, with one study finding reduced secretion[50], while another study found no effect on secretion[44]. Both studies used human embryonic kidney cells overexpressing the mutation. The difference in findings may be due to culture conditions, i.e. the presence of high levels of CSF1, which can mask the Trem2 phenotype.

All the aforementioned studies overexpressed R47H-Trem2 in cell lines, or studied recombinant R47H-Trem2. In the human AD, though, patients still have one wild-type copy of *TREM2*. Only one study to date studied heterozygous R47H-Trem2. *In vitro*, heterozygous R47H-Trem2 does not impact macrophage cell survival nor did it induce transcriptomic changes, unlike Trem2 deficiency[80], suggesting that in the heterozygous condition, one functioning copy of Trem2 may be sufficient to induce Trem2 signaling in many cases.

Several of the *in vitro* findings align with observations from AD patients with the R47H mutation. R47H-carriers have similar levels of TREM2 protein in the brain as AD non-carriers, suggesting that TREM2 expression is not impacted by the mutation[81]. Moreover, the ratio between immature non-glycosylated, and mature glycosylated TREM2 is unaffected in R47H-AD carriers, indicating intact intracellular trafficking of the receptor[81]. In sum, in humans, R47H-TREM2 does not impact protein levels or maturation, suggesting that the impairment may occur at the levels of ligand-binding and downstream signaling.

Overall, studies of overexpressed R47H-Trem2 highlight a deficit in ligand binding. However, studies of heterozygous R47H-Trem2 have not identified any strong phenotypes that could explain its associated risk with AD. One possible explanation for its association with AD may be that in the aging, diseased brain, microglia require the maximum amount of Trem2 signaling. The reduction in signaling caused by only having one fully functioning copy of Trem2

and one somewhat impaired copy is significant enough over time to exacerbate disease pathogenesis. Studies utilizing endogenously expressed heterozygous R47H-Trem2 are required to understand the extent to what the mutation impacts Trem2 signaling, particularly over time and after numerous challenges when Trem2 signaling may be especially critical.

1.7 R47h-Trem2 Exhibits Mild Phenotypes in the Context of Amyloid Pathology

In vivo studies have found that R47H results in only a partial loss-of-function, with subtle deficits compared to Trem2 deficiency. *In vivo*, overexpression of R47H-human TREM2 on a mouse Trem2 knockout background reduces sTrem2 levels, microgliosis, and microglial clustering around plaques[33]. These phenotypes are similar to what is observed in Trem2-deficient mice. However, R47H human TREM2 does not affect amyloid beta levels[33]. Future studies are needed to determine whether this variant affects plaque morphology or plaque load at different time points. Curiously, R47H human TREM2 mice exhibit significantly reduced staining for the extracellular domain of Trem2 on neurons and plaques[33]. The functional consequences of sTrem2 binding to neurons and plaques remain to be determined.

Another study used CRISPR to knock-in the R47H variant into the mouse Trem2 gene[82]. These mice have fewer microglia around plaques and reduced microglial proliferation. However, the mutation also reduced Trem2 levels by 50%, making it a heterozygote. A follow-up study discovered that mouse Trem2 has a cryptic splice site that becomes active with the R47H variant[83]. This splice site is not present in humans, though[83]. This surprising finding suggests caution when interpreting results from studies expressing R47H in mouse Trem2, as the observed phenotypes may reflect the consequences of Trem2 haploinsufficiency rather than that of the mutation. Oddly, though, a contemporary study out of Amgen that also used CRISPR to knock-in the R47H variant into the mouse Trem2 gene did not observe any reduction in Trem2 mRNA levels in the brain[80]. One possibility is that the silent mutations they introduced

along with the R47H mutation masked the splice site. Further work is needed to resolve these conflicting findings.

These studies are merely the beginnings of the field's attempt at unraveling the mystery behind R47H-TREM2's pathogenicity. They suggest that R47H-TREM2 results in mild phenotypes in the context of amyloid, which aligns with its identification as a risk factor, and not a causal factor, for AD. However, given the potential opposing roles of Trem2 on amyloid and tau, one major gap in the field is whether R47H-TREM2 is toxic in the context of tau pathology. Moreover, no study to date has addressed the functional consequences of the heterozygous R47H variant *in vivo*. To address these gaps, we generated novel wild-type and heterozygous R47H human TREM2 knock-in mouse models and crossed them to a tauopathy mouse model to determine whether R47H-TREM2 on its own would be pathological, and whether it would exacerbate tau pathology. These findings are presented in chapter three of this thesis.

Chapter 2: Differential Effects of Trem2 Haploinsufficiency and Deficiency on Microglial Function in Health and Disease

2.1 Abstract

Alzheimer's disease (AD), the most common form of dementia, is characterized by the abnormal accumulation of amyloid plaques and hyperphosphorylated tau aggregates, as well as microgliosis. Hemizygous missense variants in Triggering Receptor Expressed on Myeloid Cells 2 (*TREM2*) are associated with elevated risk for developing late-onset AD. These variants are hypothesized to result in loss-of-function, mimicking TREM2 haploinsufficiency. Yet, the consequences of TREM2 haploinsufficiency on tau pathology and microglial function remain unknown. We report the effects of partial and complete loss of TREM2 on microglial function and tau-associated deficits. *In vivo* imaging revealed that microglia from aged TREM2 haploinsufficient mice show a greater impairment in their injury response compared to microglia from aged TREM2 knockout mice. In transgenic mice expressing mutant human tau, TREM2 haploinsufficiency, but not complete loss of TREM2, increased tau pathology. In addition, while complete TREM2 deficiency protected against tau-mediated microglial activation and atrophy, TREM2 haploinsufficiency elevated expression of pro-inflammatory markers and exacerbated atrophy at a late stage of disease. The differential effects of partial and complete loss of TREM2 on microglial function and tau pathology provide important insights into the critical role of TREM2 in AD pathogenesis.

2.2 Significance

Late-onset Alzheimer's disease is the most common form of dementia. A rare hemizygous variant in a microglial-expressed gene, Triggering Receptor Expressed on Myeloid Cells 2 (*TREM2*), significantly increases risk for late-onset Alzheimer's disease. This variant is

thought to cause loss of function, inducing TREM2 haploinsufficiency. The ramifications of TREM2 haploinsufficiency on microglial function and tau pathology are major gaps in the field. We find that in contrast to the protective effects of complete TREM2 deficiency, TREM2 haploinsufficiency exacerbates tau pathology, inflammation, and atrophy at a late stage of disease in a mouse model of tauopathy. The differential effects of partial and complete loss of TREM2 are important considerations for TREM2-targeted therapeutic strategies.

2.3 Introduction

Alzheimer's disease (AD), the most common form of dementia, is characterized pathologically by the abnormal accumulation of amyloid plaques, hyperphosphorylated tau aggregates, and microgliosis. The recent genetic implication of a microglial-expressed gene, Triggering Receptor Expressed on Myeloid Cells 2 (*TREM2*), in late-onset AD suggests a pivotal role for microglia in AD pathogenesis. Although mutations in *TREM2* are rare, this gene is nonetheless the strongest immune gene-specific risk factor for AD discovered thus far[1-3]. *TREM2* encodes a transmembrane receptor that is expressed by microglia in the brain[4,5]. TREM2 has been implicated in neuroinflammation and in the metabolic fitness, proliferation, survival, and phagocytic capacity of microglia[6-16].

The most common AD-associated *TREM2* variant, R47H, is associated with an approximately 3-fold increased risk for developing late-onset AD[1-3]. It is thought to result in a TREM2 loss-of-function phenotype[10,17,18]. Compared to non-carriers, R47H carriers have higher levels of phosphorylated tau around plaques[19] and more neurofibrillary tangles[20]. In addition, R47H carriers have higher levels of cerebrospinal fluid (CSF) soluble TREM2, and CSF soluble TREM2 levels were significantly correlated with higher levels of CSF phosphorylated tau[21]. These observations in human patients suggest a detrimental effect of TREM2 haploinsufficiency on tau pathology. Surprisingly, in a tauopathy mouse model, complete loss of TREM2 function

had no effect on tau pathology, while protecting against brain atrophy[22]. These findings highlight the need to assess the effects of TREM2 haploinsufficiency in AD models.

We investigated how TREM2 haploinsufficiency, a model relevant to AD cases carrying hemizygous risk variants, affects microglial function and tau pathology. Using *in vivo* two-photon microscopy to visualize microglial motility, we found that TREM2 haploinsufficiency resulted in an age-dependent impairment in microglial injury response without affecting baseline motility. Interestingly, complete loss of TREM2 resulted in a milder impairment in injury-induced motility compared to TREM2 haploinsufficiency. We then investigated the effects of TREM2 haploinsufficiency and complete deficiency on tau pathology in mice expressing mutant human tau (P301S). Our findings demonstrated a robust increase in tau pathology in TREM2 haploinsufficient mice, an effect that was not observed in TREM2 knockout mice. We further investigated how TREM2 haploinsufficiency and complete deficiency affect tau-mediated deficits.

2.4 Results

TREM2 Haploinsufficiency Causes an Age-Dependent Impairment in Microglia's Injury Response

Microglia carry out critical functions of surveying the brain and responding to injury[23,24]. To address the effect of TREM2 on microglial surveillance, we used *in vivo* two-photon imaging to examine microglial motility in 3–5-month-old *TREM2*$^{+/+}$, *TREM2*$^{+/-}$ and *TREM2*$^{-/-}$ mice crossed to *Cx3cr1*$^{GFP/+}$ mice, in which microglia express enhanced green fluorescent protein (eGFP) driven by the *Cx3cr1* promoter[25]. Analysis of a 10-minute time-lapse recording of cortical microglia showed no differences in the baseline properties of microglia across the three genotypes, including average speed of process extension and retraction and total change in process length (Fig. 1 *A*–*B*). TREM2 also had no effect on microglial cell density or cell body

size at baseline (SI Appendix, Fig. S1 *A*–*B*). Moreover, in response to a laser-induced focal tissue injury, microglia from young *TREM2*$^{+/+}$, *TREM2*$^{+/-}$ and *TREM2*$^{-/-}$ mice exhibited no difference in cell density (Fig. 1 *C*), cell body size (SI Appendix, Fig. S1*C*), or the density of microglial processes extending towards the injury site (Fig. 1 *D*-*E*, Movie S*1*).

Given the established association of TREM2 with age-related diseases[1-3,26], we next examined the effects of TREM2 on microglial motility in 9–14-month-old *TREM2*$^{+/+}$, *TREM2*$^{+/-}$ and *TREM2*$^{-/-}$ mice. At baseline, the average speed and total change in process length did not differ across genotypes (Fig. 1 *F*–*G*). Microglial cell density or cell body size also remained similar (SI Appendix, Fig. S1 *D*-*E*). Strikingly, in response to focal tissue injury, microglia from older *TREM2*$^{+/-}$ mice demonstrated a significantly reduced response to injury compared to wild-type microglia, as evidenced by fewer microglial processes extending towards the site of injury at any given time point (Fig. 1 *I*-*J*, Movie S*2*). *TREM2*$^{-/-}$ microglia showed a significant, yet milder attenuation in response size compared to *TREM2*$^{+/-}$ (Fig. 1 *I*-*J,* Movie S*2*). *TREM2*$^{+/-}$ microglia were the slowest to respond, extended the fewest processes towards the site of injury, and did not reach the injury site within 60 minutes (Fig. 1 *I*, Movie S*2*). *TREM2*$^{-/-}$ microglia, on the other hand, were able to reach the injury site within 60 minutes, similar to wild-type microglia (Fig. 1 *I*, Movie S*2*). The impairment in *TREM2*$^{+/-}$ and *TREM2*$^{-/-}$ microglia's responses were not associated with differences in microglial density (Fig. 1 *H*) or activation state, as evidenced by the unaltered cell body size (SI Appendix, Fig. S1*F*). Moreover, there was no correlation between ablation size and response (SI Appendix, Fig. S1*G*), indicating that the reduced response sizes in TREM2-deficient microglia were not due to smaller injuries. Thus, surprisingly, TREM2 haploinsufficiency attenuates the *in vivo* microglial response to tissue injury in an age-dependent manner and to a greater extent than complete TREM2 deficiency.

TREM2 Haploinsufficiency and Complete Deficiency Differentially Regulate the Microglial Transcriptome in the Presence and Absence of Tauopathy

Next, to identify microglial pathways regulated by *TREM2* in an unbiased fashion, we performed RNA sequencing (RNAseq) of adult microglia isolated using CD11b magnetic beads from young *TREM2*$^{+/+}$, *TREM2*$^{+/-}$ and *TREM2*$^{-/-}$ mice. We confirmed the purity of our adult-isolated microglia, as their transcriptome closely matched a previously published microglial transcriptome[27] (Fig. 2 *A*). TREM2 haploinsufficiency and complete deficiency altered the microglial transcriptome in unique ways (Fig. 2 *B*). 107 transcripts were significantly different between *TREM2*$^{+/-}$ and *TREM2*$^{-/-}$ (Fig. 2 *C*). Ingenuity pathway analysis (IPA^{TM}) revealed cellular movement as the most significantly altered biological pathway in *TREM2*$^{+/-}$ microglia compared to *TREM2*$^{-/-}$ (Fig. 2 *D*), consistent with our *in vivo* imaging finding that *TREM2*$^{+/-}$ microglia exhibited greater impairment in their injury response than *TREM2*$^{-/-}$ (Fig. 1 *J*). Interestingly, these transcriptomic alterations in young *TREM2*$^{+/-}$ microglia preceded the impaired injury response seen in aged *TREM2*$^{+/-}$ microglia. In addition, multiple pathways pertaining to inflammation were significantly altered between *TREM2*$^{+/-}$ and *TREM2*$^{-/-}$ microglia, such as immune cell trafficking and inflammatory response (Fig. 2 *D*), suggesting differential regulation of inflammation in TREM2$^{+/-}$ versus *TREM2*$^{-/-}$ microglia.

The rare R47H missense variant in *TREM2* is associated with increased risk for tauopathies[2,3,26,28] and hyperphosphorylation of tau in AD carriers[19]. We next investigated how TREM2 affects tau pathology and tau-associated deficits in the P301S tauopathy mouse model (Prnp-MAPT*P301S)[29]. The effects of TREM2 haploinsufficiency and complete loss of TREM2 on tau-induced transcriptional changes were examined at 8-9 months of age (SI Appendix, Fig. S2*A*), when P301S mice exhibit significant tau inclusions, microgliosis, and neuronal loss[29]. Compared with P301S+ *TREM2*$^{+/+}$ mice, there were 232 differentially expressed transcripts in P301S+ *TREM2*$^{+/-}$ mice (Fig. 3 *A*). These transcripts were significantly enriched for pathways pertaining to microglial development, such as TGFβ signaling[4], and inflammation, such as IL2

STAT5 signaling and TNFα signaling via NF-κB (SI Appendix, Fig. S2*B*). To validate these pathways, we performed quantitative real-time PCR of pro- and anti-inflammatory markers. Consistent with tau-mediated inflammatory responses, expression of P301S human tau significantly increased levels of pro-inflammatory cytokines TNF-α, IL-1α, and IL-1β (SI Appendix, Fig. S3). Importantly, *TREM2*$^{+/-}$ resulted in significantly elevated levels of TNF-α and IL-1α compared to P301S+ *TREM2*$^{+/+}$ mice, but had no effects on anti-inflammatory markers VEGF1, Cox2, or IL-34 (SI Appendix, Fig. S3). Differentially expressed genes in P301S+ *TREM2*$^{-/-}$, on the other hand, were significantly enriched for genes related to metabolism, such as oxidative phosphorylation, glycolysis, and MTORC1 signaling (SI Appendix, Fig. S2*C*). Direct comparison of P301S+ *TREM2*$^{+/-}$ and P301S+ *TREM2*$^{-/-}$ revealed that of the 389 differentially expressed transcripts, there was a significant enrichment of complement-related genes and inflammatory response genes (Fig. 3 *B*).

TREM2 Haploinsufficiency Exacerbates Tau Pathology in P301S Mice

We then assessed how partial and complete loss of TREM2 affects tau aggregation. Immunohistochemistry with the AT8 antibody, which recognizes two phosphorylation sites on tau (pS202, pT205), revealed a significant increase in the AT8+ area in the cortex of P301S+ *TREM2*$^{+/-}$ mice compared to P301S+ *TREM2*$^{+/+}$ and P301S+ *TREM2*$^{-/-}$ (Fig. 4 *A*-*B*) and a trend towards increased AT8 pathology in the hippocampus (Fig. 4 *C*-*D*). In contrast, there was no difference in AT8 load between P301S+ *TREM2*$^{-/-}$ and P301S+ *TREM2*$^{+/+}$ mice in hippocampus and cortex (Fig. 4 *A*-*D*), consistent with a recent finding by Leyns *et al* [22]. We also performed immunohistochemistry with the MC1 antibody, which detects a pathological conformation of tau [30]. Consistent with the differential effects induced by *TREM2*$^{+/-}$ and *TREM2*$^{-/-}$ on AT8 pathology, P301S+ *TREM2*$^{+/-}$ mice had significantly greater MC1+ area than P301S+ *TREM2*$^{-/-}$ in cortex (Fig. 4 *E*-*F*) and in hippocampus (Fig. 4 *G*-*H*). Similarly, the MC1+ area in the hippocampus of

P301S+ *TREM2*$^{+/-}$ mice, most notably in the mossy fibers, was significantly greater than in P301S+ *TREM2*$^{+/+}$ mice (Fig. 4 *G-H*). A similar trend was observed in the cortex (Fig. 4 *E-F*). In sharp contrast, the MC1+ area trended towards a decrease in P301S+ *TREM2*$^{-/-}$ mice compared to P301S+ *TREM2*$^{+/+}$ mice (Fig. 4 *F* and *H*). Thus, TREM2 haploinsufficiency, but not complete loss of TREM2, enhances tau pathology.

Differential Effects of Partial and Complete TREM2 Deficiency on Atrophy and Microgliosis in P301S Mice

Next, we investigated how TREM2 haploinsufficiency and complete deficiency affect tau-induced neurodegeneration. At 8-9 months of age, there were similar levels of hippocampal neuronal loss in P301S mice regardless of TREM2 genotype (SI Appendix, Fig. S4*A-B*) and tau-induced atrophy could not yet be detected in cortex (SI Appendix, Fig. S4*C*). However, complete TREM2 deficiency resulted in a protection against hippocampal atrophy, as evidenced by the smaller lateral ventricle area (Fig. 5 *A-B*), and a trend towards increased hippocampal area (Fig. 5 *C*). This result is in agreement with a previous report that showed that complete TREM2 deficiency protected against brain atrophy in P301S mice [22]. Compared to P301S+ *TREM2*$^{+/+}$, TREM2 haploinsufficiency did not significantly affect atrophy at 8-9 months (Fig. 5 *A-C*) or at 10-11 months of age (Fig. 5 *D-E*). However, compared to wild-type mice, *P301S*+ *TREM2*$^{+/-}$, but not *P301S*+ *TREM2*$^{+/+}$ mice exhibited significantly more severe atrophy (Fig. 5 *D-E*).

We next evaluated how TREM2 levels affect tau-induced microgliosis, a canonical hallmark of AD pathology recapitulated in P301S mice [29]. Analysis of Iba1 immunoreactivity in the hippocampus revealed an expected significant increase in microglial number induced by P301S tau (Fig. 6 *A-B*). Interestingly, compared to P301S+ *TREM2*$^{+/+}$, complete TREM2 deficiency, but not haploinsuffciency, resulted in a trend towards reduced microglial density, (Fig. 6 *A-B*). Moreover, the number of microglia positively correlated with MC1+ area (Fig. 6 *C*),

supporting the idea that elevated tau pathology is associated with inflammatory responses in microglia.

To further characterize how TREM2 levels affect tau-mediated microglial activation, we performed morphological analyses using 3D renderings of confocal images (Fig. 6 *D*). Compared to *TREM2*$^{+/+}$, TREM2 haploinsufficiency in P301S mice induced significantly shortened processes (Fig. 6 *E*) and fewer branches (Fig. 6 *F*), indicating strong tau-mediated microglial activation. In contrast, complete loss of TREM2 in P301S mice resulted in a failure to induce morphological changes associated with microglial activation; microglia from *P301S*+ *TREM2*$^{-/-}$ mice exhibited similar process length and arborization as non-activated microglia from wild-type (*TREM*$^{+/+}$) mice (Fig. 6 *D-F*).

2.5 Discussion

Our study highlights multiple findings in which TREM2 haploinsufficiency resulted in stronger or different phenotypes than complete TREM2 deficiency. TREM2 haploinsufficiency led to a greater age-dependent impairment in microglia's response to injury compared to complete TREM2 deficiency. Moreover, TREM2 haploinsufficiency exacerbated tau pathology, atrophy and inflammation. On the contrary, complete loss of TREM2 protected against atrophy and reduced microgliosis. Interestingly, complete loss of TREM2 was also associated with trends towards reduced MC1+ pathology. These results highlight multiple TREM2 phenotypes that are gene-dose independent. Since hemizygous TREM2 variants are associated with elevated risk for AD, TREM2 haploinsufficiency may be a more relevant model to study how TREM2 contributes to AD pathogenesis. Indeed, complete loss of TREM2 in humans results in Nasu-Hakola disease[31], which could be driven by mechanisms that are distinct from those of AD.

As the resident immune cells in the brain, microglia need to respond robustly to injury, especially in neurodegenerative brains that have increased neuronal death and accumulation of abnormal protein aggregates. Using *in vivo* imaging, we showed that TREM2 haploinsufficiency impairs microglia's injury-induced response in an age-dependent manner and to a greater degree than complete loss of TREM2 (Fig. 1 *J*, Movie S2). It is interesting that this result is present in aged, but not young mice. This finding mirrors the role of TREM2 in the development of late-onset AD. Notably, there was no impairment in baseline motility (Fig. 1 *F-G*), suggesting that TREM2 modulates microglial pathways specifically related to injury response. This injury-specific modulation of motility may contribute to TREM2's implication in neurodegeneration, where neuronal injury is abundant. This type of differential modulation of baseline and injury-induced motility has been observed previously in the microglia field. For example, the purinergic receptor P2RY12 was found to slow down microglia's response to ATP/ADP released during injury without affecting baseline motility[32].

Aged TREM2 haploinsufficient microglia were significantly slower to respond to injury and extended fewer processes towards the site of injury throughout the 60-minute imaging session (Movie S*2*). Interestingly, TREM2 deficient microglia showed an intermediate phenotype between TREM2 haploinsufficient and wild-type microglia. On average, they extended more processes towards the site of injury than TREM2 haploinsufficient microglia, and they were able to reach the site of injury within 60 minutes (Movie S*2*). This gene-dose independent phenomenon may be driven by compensatory mechanisms in microglia completely lacking TREM2 from development, while TREM2 haploinsufficiency could elicit different types of compensatory changes via modulation of TREM2 expression from the existing allele. Our RNAseq analyses of *TREM2*$^{+/-}$ and *TREM2*$^{-/-}$ microglia revealed a significant difference in the cellular movement pathway induced by TREM2 deficiency (Fig 2. *D*), consistent with a previous study that looked at *TREM2*$^{+/+}$ and *TREM2*$^{-/-}$ microglia[33]. Interestingly, the transcriptional changes in TREM2 haploinsufficient microglia occurred prior to the development of the impaired

injury response. These observations are consistent with a two-hit hypothesis: young TREM2 haploinsufficient microglia can maintain normal function, but those challenged by age or pathological conditions, such as tauopathy, are unable to do so.

Remarkably, TREM2 haploinsufficiency exacerbated tau pathology, whereas complete TREM2 deficiency did not (Fig. 4), yet another phenotype that was not gene-dose dependent. Of note, patients with the R47H TREM2 variant have increased tau pathology[13], similar to TREM2 haploinsufficient tauopathy mice. One likely explanation for the lack of effect of complete TREM2 deficiency on multiple phenotypes is that complete loss of TREM2 may result in compensatory changes. Indeed, a previous study showed that in the absence of TREM2, expression of homeostatic microglial genes was not suppressed, but rather fully preserved and even slightly increased, supporting the possibility of compensation [33]. Moreover, we observed transcriptional changes between *TREM2*$^{+/-}$ and *TREM2*$^{-/-}$ microglia that may underlie gene-dose independent phenotypes. Inflammatory pathways were altered at the transcriptional level between *TREM2*$^{+/-}$ and *TREM2*$^{-/-}$ microglia from young mice (Fig. 2 *D*), highlighting early-onset, inherent TREM2-dependent changes in microglial activation that persisted in older, disease states (Fig S3, Fig. 6).

The P301S mouse model begins to show neuronal loss at 9-10 months of age[29]. Neither TREM2 haploinsufficiency nor complete deficiency exacerbated neuronal loss at 8-9 months of age. However, complete loss of TREM2 protected against tau-induced atrophy (Fig. 5 *A*-*C*). Our results suggest that the increase in cortical volume seen by Leyns *et al*[22] may not be due to a protection against neuronal loss, per se, as P301S+ *TREM2*$^{-/-}$ mice had a similar number of neurons as P301S+ *TREM2*$^{+/+}$ mice (Fig. S4*C*). Instead, complete loss of TREM2 may increase cortical volume through other mechanisms, such as protection against loss of neuronal processes or, given TREM2's implication in lipid sensing[10], through an increase in the brain's lipid content. In contrast to the neuroprotective effect of complete loss of TREM2, partial loss of TREM2 appears to be detrimental, highlighted by the significant increase in lateral ventricle area

at 10-11 months of age compared to wild-type mice (Fig. 5 *E*). It is interesting to note that complete loss of TREM2 resulted in a trend towards reduced late-stage tau pathology and reduced atrophy, while TREM2 haploinsufficiency exacerbated tau pathology and exacerbated atrophy. It remains to be determined whether tau pathology and microglial activation work together or independently to cause brain atrophy.

We also detected increased expression of pro-inflammatory cytokines in P301S+ *TREM2*$^{+/-}$ mice (Fig. S3), a finding consistent with the cytokine profiles in R47H carriers with AD[20]. However, it is unclear whether the increased inflammatory state is a cause or consequence of the increased tau pathology present in both *TREM2*$^{+/-}$ mice and patients with the R47H variant[19]. Interestingly, in amyloid mouse models, TREM2 haploinsufficiency did not affect the expression of pro- or anti-inflammatory markers at early or later stages of amyloid pathology[8], but reduced microglia number[10]. These studies, in conjunction with our data, suggest that TREM2 haploinsufficiency differentially modulates inflammation in the contexts of amyloid and tau pathology. On the other hand, P301S+ mice completely lacking *TREM2* have been shown to have lower levels of pro-inflammatory markers[22], as well as reduced microglial density and a resting state morphology. Together, these results, along with our RNAseq data (Fig. 2 *D*, Fig. 3 *B,* Fig. S2*B*), suggest inflammation as a possible mechanism by which TREM2 haploinsufficiency versus complete deficiency result in apparent opposing phenotypes, such as their effects on tau pathology. Microglia have been implicated in the spread of tau pathology[34] and their activation state could contribute to how they respond in the context of tauopathy. Indeed, we found a significant positive correlation between microglial density and tau pathology (Fig. 6 *C*).

Our surprising discovery that TREM2 haploinsufficiency exerts a more robust impairment in microglial function and exacerbation of tau pathology compared to complete loss of TREM2 highlights the plasticity of microglia in response to TREM2 deficiency. The potential detrimental

effects of TREM2 haploinsufficiency can provide insight into how TREM2 contributes to AD pathogenesis, and inform potential TREM2-targeted therapeutic strategies.

2.6 Methods

Detailed procedures for all methods below are described in the SI Appendix.

Mice. All animal procedures were carried out under protocols approved by the University of California, San Francisco, Institutional Animal Care and Use Committee.

In vivo imaging. Intravital imaging using two-photon microscopy was performed with thinned-skull windows as previously described[24].

Antibodies, immunohistochemistry and image analysis. Immunohistochemistry and image analysis were performed by experimenters blinded to the genotypes. The code was not broken until all analyses were completed.

Adult microglia isolation and quantitative reverse-transcription PCR. Adult microglia were isolated from *TREM2*$^{+/+}$, *TREM2*$^{+/-}$ and *TREM2*$^{-/-}$ mice as described previously[35].

RNA-sequencing and analysis. RNAseq libraries were prepared with either Ovation RNAseq system v2 kit (NuGEN) or Lexogen's QuantSeq 3' mRNA-Seq Library Prep Kit. All RNAseq data has been deposited within the Gene Expression Omnibus (GEO) repository (www.ncbi.nlm.nih.gov/geo), accession number GSE118630.

Statistical analysis. Data were analyzed with Graphpad Prism v.7 (GraphPad), STATA12 (StataCorp LP), or R (R Foundation for Statistical Computing). Multilevel mixed-effects linear regression model fit using STATA12 was used to compare curves for young and aged mice in response to injury. For cluster analyses of multiple measurements from individual mice, we used the R package lmer. Outliers were removed based on Graphpad's outlier analysis algorithm. All animals were included for statistical analyses unless otherwise noted.

2.7 Acknowledgements

We thank Victoria Rafalski for her contribution in discussing the *in vivo* imaging work. All *in vivo* imaging was conducted by F.A.S. at the Center for In Vivo Imaging Research at Gladstone Institutes. Library preparation and quality control for adult microglia RNA-sequencing was conducted by Jim McGuire, PhD, at the Gladstone Genomics Core. RNA-sequencing was conducted by the University of California San Francisco's Center for Advanced Technology. This study was supported by the National Institute of Aging Grants AG051390 and R01AG054214 (to L.G.), the National Institute of Neurological Diseases and Stroke Grant NS097976 (to K.A.), the American Heart Association Scientist Development Grant 13SDG17210051 (to D.D.), the National Institute of Neurological Diseases and Stroke Informatics Center for Neurogenetics and Neurogenomics Grant P30 NS062691 (to G.C.), as well as the National Institute of Aging Grant F31 AG058505 (to F.A.S.).

2.8 References

1 Cruchaga, C. *et al.* GWAS of cerebrospinal fluid tau levels identifies risk variants for Alzheimer's disease. *Neuron* **78**, 256-268, doi:10.1016/j.neuron.2013.02.026 (2013).

2 Jonsson, T. *et al.* Variant of TREM2 associated with the risk of Alzheimer's disease. *N Engl J Med* **368**, 107-116, doi:10.1056/NEJMoa1211103 (2013).

3 Guerreiro, R. *et al.* TREM2 variants in Alzheimer's disease. *N Engl J Med* **368**, 117-127, doi:10.1056/NEJMoa1211851 (2013).

4 Butovsky, O. *et al.* Identification of a unique TGF-beta-dependent molecular and functional signature in microglia. *Nat Neurosci* **17**, 131-143, doi:10.1038/nn.3599 (2014).

5 Hickman, S. E. *et al.* The microglial sensome revealed by direct RNA sequencing. *Nat Neurosci* **16**, 1896-1905, doi:nn.3554 [pii] 10.1038/nn.3554 (2013).

6 Neumann, H. & Takahashi, K. Essential role of the microglial triggering receptor expressed on myeloid cells-2 (TREM2) for central nervous tissue immune homeostasis. *J Neuroimmunol* **184**, 92-99, doi:10.1016/j.jneuroim.2006.11.032 (2007).

7 Hsieh, C. L. *et al.* A role for TREM2 ligands in the phagocytosis of apoptotic neuronal cells by microglia. *J Neurochem* **109**, 1144-1156, doi:10.1111/j.1471-4159.2009.06042.x (2009).

8 Ulrich, J. D. *et al.* Altered microglial response to Abeta plaques in APPPS1-21 mice heterozygous for TREM2. *Mol Neurodegener* **9**, 20, doi:10.1186/1750-1326-9-20 (2014).

9 Poliani, P. L. *et al.* TREM2 sustains microglial expansion during aging and response to demyelination. *J Clin Invest* **125**, 2161-2170, doi:10.1172/JCI77983 (2015).

10 Wang, Y. *et al.* TREM2 lipid sensing sustains the microglial response in an Alzheimer's disease model. *Cell* **160**, 1061-1071, doi:10.1016/j.cell.2015.01.049 (2015).

11 Zhong, L. *et al.* DAP12 stabilizes the C-terminal fragment of the triggering receptor expressed on myeloid cells-2 (TREM2) and protects against LPS-induced pro-

inflammatory response. *J Biol Chem* **290**, 15866-15877, doi:10.1074/jbc.M115.645986 (2015).

12 Wang, Y. *et al.* TREM2-mediated early microglial response limits diffusion and toxicity of amyloid plaques. *J Exp Med* **213**, 667-675, doi:10.1084/jem.20151948 (2016).

13 Yuan, P. *et al.* TREM2 Haplodeficiency in Mice and Humans Impairs the Microglia Barrier Function Leading to Decreased Amyloid Compaction and Severe Axonal Dystrophy. *Neuron* **92**, 252-264, doi:10.1016/j.neuron.2016.09.016 (2016).

14 Ulland, T. K. *et al.* TREM2 maintains microglial metabolic fitness in Alzheimer's Disease. *Cell* **170**, 649-663 e613, doi:10.1016/j.cell.2017.07.023 (2017).

15 Zheng, H. *et al.* TREM2 promotes microglial survival by activating wnt/beta-catenin pathway. *J Neurosci* **37**, 1772-1784, doi:10.1523/JNEUROSCI.2459-16.2017 (2017).

16 Zhong, L. *et al.* Soluble TREM2 induces inflammatory responses and enhances microglial survival. *J Exp Med* **214**, 597-607, doi:10.1084/jem.20160844 (2017).

17 Cheng-Hathaway, P. J. *et al.* The Trem2 R47H variant confers loss-of-function-like phenotypes in Alzheimer's disease. *Mol Neurodegener* **13**, 29, doi:10.1186/s13024-018-0262-8 (2018).

18 Song, W. M. *et al.* Humanized TREM2 mice reveal microglia-intrinsic and -extrinsic effects of R47H polymorphism. *J Exp Med* **215**, 745-760, doi:10.1084/jem.20171529 (2018).

19 Yuan, P. *et al.* TREM2 Haplodeficiency in Mice and Humans Impairs the Microglia Barrier Function Leading to Decreased Amyloid Compaction and Severe Axonal Dystrophy. *Neuron* **90**, 724-739, doi:10.1016/j.neuron.2016.05.003 (2016).

20 Roussos, P. *et al.* The triggering receptor expressed on myeloid cells 2 (TREM2) is associated with enhanced inflammation, neuropathological lesions and increased risk for Alzheimer's dementia. *Alzheimers Dement* **11**, 1163-1170, doi:10.1016/j.jalz.2014.10.013 (2015).

21 Piccio, L. *et al.* Cerebrospinal fluid soluble TREM2 is higher in Alzheimer disease and associated with mutation status. *Acta Neuropathol* **131**, 925-933, doi:10.1007/s00401-016-1533-5 (2016).

22 Leyns, C. E. G. *et al.* TREM2 deficiency attenuates neuroinflammation and protects against neurodegeneration in a mouse model of tauopathy. *Proceedings of the National Academy of Sciences of the United States of America* **114**, 11524-11529, doi:10.1073/pnas.1710311114 (2017).

23 Nimmerjahn, A., Kirchhoff, F. & Helmchen, F. Resting microglial cells are highly dynamic surveillants of brain parenchyma in vivo. *Science* **308**, 1314-1318, doi:1110647 [pii] 10.1126/science.1110647 (2005).

24 Davalos, D. *et al.* ATP mediates rapid microglial response to local brain injury in vivo. *Nat Neurosci* **8**, 752-758, doi:10.1038/nn1472 (2005).

25 Jung, S. *et al.* Analysis of fractalkine receptor CX(3)CR1 function by targeted deletion and green fluorescent protein reporter gene insertion. *Mol Cell Biol* **20**, 4106-4114 (2000).

26 Guerreiro, R. J. *et al.* Using exome sequencing to reveal mutations in TREM2 presenting as a frontotemporal dementia-like syndrome without bone involvement. *JAMA Neurol* **70**, 78-84, doi:10.1001/jamaneurol.2013.579 (2013).

27 Zhang, Y. *et al.* An RNA-sequencing transcriptome and splicing database of glia, neurons, and vascular cells of the cerebral cortex. *J Neurosci* **34**, 11929-11947, doi:10.1523/JNEUROSCI.1860-14.2014 (2014).

28 Rayaprolu, S. *et al.* TREM2 in neurodegeneration: evidence for association of the p.R47H variant with frontotemporal dementia and Parkinson's disease. *Mol Neurodegener* **8**, 19, doi:10.1186/1750-1326-8-19 (2013).

29 Yoshiyama, Y. *et al.* Synapse loss and microglial activation precede tangles in a P301S tauopathy mouse model. *Neuron* **53**, 337-351, doi:10.1016/j.neuron.2007.01.010 (2007).

30 Jicha, G. A., Bowser, R., Kazam, I. G. & Davies, P. Alz-50 and MC-1, a new monoclonal antibody raised to paired helical filaments, recognize conformational epitopes on recombinant tau. *Journal of neuroscience research* **48**, 128-132 (1997).

31 Paloneva, J. *et al.* Mutations in two genes encoding different subunits of a receptor signaling complex result in an identical disease phenotype. *Am J Hum Genet* **71**, 656-662, doi:10.1086/342259 (2002).

32 Haynes, S. E. *et al.* The P2Y12 receptor regulates microglial activation by extracellular nucleotides. *Nat Neurosci* **9**, 1512-1519, doi:10.1038/nn1805 (2006).

33 Mazaheri, F. *et al.* TREM2 deficiency impairs chemotaxis and microglial responses to neuronal injury. *EMBO Rep* **18**, 1186-1198, doi:10.15252/embr.201743922 (2017).

34 Asai, H. *et al.* Depletion of microglia and inhibition of exosome synthesis halt tau propagation. *Nat Neurosci* **18**, 1584-1593, doi:10.1038/nn.4132 (2015).

35 Krabbe, G. *et al.* Microglial NFkappaB-TNFalpha hyperactivation induces obsessive-compulsive behavior in mouse models of progranulin-deficient frontotemporal dementia. *Proceedings of the National Academy of Sciences of the United States of America* **114**, 5029-5034, doi:10.1073/pnas.1700477114 (2017).

2.9 Supplementary Text

Mice. *Cx3cr1*$^{GFP/GFP}$ (https://www.jax.org/strain/005582) were crossed with *TREM2*$^{+/-1}$ to obtain *Cx3cr1*$^{GFP/+}$ *TREM2*$^{+/+}$, *Cx3cr1*$^{GFP/+}$ *TREM2*$^{+/-}$, and *Cx3cr1*$^{GFP/+}$ *TREM2*$^{-/-}$ mice. P301S transgenic mice (https://www.jax.org/strain/008169) were crossed with *TREM2*$^{+/-}$ to generate P301S+ *TREM2*$^{+/+}$, P301S+ *TREM2*$^{+/-}$, P301S+ *TREM2*$^{-/-}$ and *TREM2*$^{+/+}$ mice. Mice of both genders were used. All animal procedures were carried out under protocols approved by the University of California, San Francisco, Institutional Animal Care and Use Committee.

Primary antibodies. Monoclonal antibodies were as follows: MC1 (a kind gift from P. Davies, 1:500) and AT8 (MN1020, Thermo Scientific, 1:500). Polyclonal antibodies were as follows: anti-Iba1 (019-19741, Wako, 1:500) and anti-NeuN (MAB377, Millipore, 1:500). Immunoreactivity was detected using Alexa Fluor goat anti-mouse or rabbit secondary antibodies in the 488- or 555-nm range (Jackson ImmunoResearch, 1:500).

In vivo imaging. For intravital imaging using two-photon microscopy, thinned-skull windows were made in *Cx3cr1*$^{GFP/+}$ *TREM2*$^{+/+}$, *Cx3cr1*$^{GFP/+}$ *TREM2*$^{+/-}$, and *Cx3cr1*$^{GFP/+}$ *TREM2*$^{-/-}$ as previously described [2]. Briefly, mice were anesthetized using ketamine-xylazine, the skull was exposed, and a small area over somatosensory cortex was thinned manually and with a high-speed drill (K.1070 High Speed Rotary Micromotor drill; Foredom). Mice were fixed onto a custom-made head plate and imaged with an Ultima IV multiphoton microscope (Bruker) equipped with MaiTai DeepSee-eHP lasers (Spectra Physics) tuned to 915 nm. Z-stacks of images spanning 50-70μm from the pial surface were obtained with a Nikon 40x 0.8 N.A. water-immersion lens. Z-stacks of images were acquired every 30 seconds (for baseline motility recordings) or every 3 minutes (for laser-induced injury recordings). Time-lapse movies were generated by projecting images of each time point along the z-axis and aligning them over time

with the StackReg plug-in in ImageJ software (NIH). Extensions and retractions of processes during baseline recordings were manually traced using the mTrackJ plugin. The movement of microglial processes toward a laser ablation was analyzed as described previously [2,3], by normalizing the number of processes near the site of injury at each time point to the overall microglial density at that time point.

Immunohistochemistry and image analysis. Mice were transcardially perfused with PBS. Hemibrains were flash frozen at -80°C for biochemical analyses; the other half was placed in 4% paraformaldehyde for 48 h, followed by 30% sucrose for 48 h at 4°C. A freezing microtome (Leica) was used to make 30μm-thick brain sections. 6-8 free-floating sections per mouse were washed in PBS, permeabilized with PBS containing 0.5% Triton X-100 for 10 min then blocked in PBS containing 10% normal goat serum (NGS) for 1 hour. Sections were then placed in PBS with 5% normal goat serum and primary antibodies overnight at 4°C. The following day, sections were washed in PBS containing 0.1% Triton X-100, incubated with Alexa-conjugated secondary antibodies in PBS with 5% normal goat serum and washed in PBS containing 0.1% Triton X-100. Images were acquired on a Keyence BZ-X700 microscope using a 10x objective. Quantification was performed using ImageJ software (NIH). For quantification of NeuN staining, images were analyzed with Keyence BZ Analyzer software for deconvoluted fluorescence quantification. Experimenters quantifying immunoreactivity were blinded. For 3D reconstruction of microglia, 40x line-scanning confocal images were taken of the CA3 hippocampal region, 1 field of view per mouse. 3D reconstruction was done using Imaris software.

RNA isolation and quantitative reverse-transcription PCR. Cortices that had been flash frozen were dissected and homogenized with a 21G needle in RLT buffer with 1% β-mercaptoethanol. RNA was isolated with the RNeasy Mini-Kit (Qiagen), and the remaining DNA was removed by incubation with RNase-free DNase (Qiagen). Purified mRNA was then

converted to cDNA using the iScript Reverse Transcription Supermix (BioRad). Quantitative RT-PCR was performed on the ABI 7900 HT sequence detector (Applied Biosystems) with SYBR Green PCR master mix (Applied Biosystems). The average value of three replicates for each sample was expressed as a threshold cycle (C_t), at which the fluorescence signal starts to increase rapidly. Then, the difference (ΔC_t) between C_t values for the transcript of interest and for mouse GAPDH was calculated for each sample. The relative gene expression for each sample was determined by $2^{-\Delta Ct}$ and expressed as fold change compared to *TREM2*$^{+/+}$. The following primers were used for quantitative RT-PCR: TNFα (forward: CATCAGTTCTATGGCCCAGA; reverse: TGCTCCTCCACTTGGTGGTT); IL-1α (forward: CACCTTACACCTACCAGAGTGATTTG; reverse: TGTTGCAGGTCATTTAACCAAGTG)**;** IL-1β (forward: TGCCACCTTTTGACAGTGATG; reverse: TGATGTGCTGCTGCGAGATT)**;** TGFβ (forward: AACCCCCATTGCTGTCCCGTG; reverse: GCGCTGAATCGAAAGCCCTGT)**;** VEGF1 (forward: GCTGCACCCACGACAGAAGGA; reverse: TCGTTACAGCAGCCTGCACAGC)**;** Cox2 (forward: GTACCGCAAACGCTTCTCCCTG; reverse: CCTCCAAAGGTGCTCGGCTTCCA)**;** IL-34 (forward: CTTTGGGAAACGAGAATTTGGAGA; reverse: GCAATCCTGTAGTTGATGGGGAAG)**;** GAPDH (forward: TGGCCTTCCGTGTTCCTAC; reverse: GAGTTGCTGTTGAAGTCGCA)

Adult microglia isolation. Adult microglia were isolated from *TREM2*$^{+/+}$, *TREM2*$^{+/-}$ and *TREM2*$^{-/-}$ as described previously[4]. Briefly, brains were perfused with ice-cold PBS and minced with a razor blade in RPMI 1640 containing 2 mM l-glutamine (Mediatech), 40 U/mL dispase, and 6% collagenase type 3 (Worthington Biochemicals). After incubation for 15 min with DNase I (10 U; Roche Applied Science) at 37 °C, enzymes were inactivated with an equal volume of PBS containing 2 mM EDTA and 2% FBS. Brains were triturated thoroughly, passed through a 70-μm filter, centrifuged at 300 × *g* for 5 min at 18 °C, and resuspended in fluorescence-activated cell sorting (FACS) buffer (500 mM EDTA, 0.5% BSA, 0.09% sodium azide in PBS). Myelin-

removal beads (Miltenyi Biotec) were added for 15 min at 4 °C, and the cells were centrifuged at 300 × *g* and resuspended in FACS buffer. Cells were magnetically separated and selected for CD11b as described above. $CD11b^+$ cells were centrifuged, and RNA was extracted (Qiagen RNeasy Kit) for RNA-sequencing.

RNA-sequencing and analysis. RNA-seq libraries were prepared with Ovation RNA-seq system v2 kit (NuGEN) from 4 replicates per genotype (total: 12 samples). Briefly, total RNA is reverse-transcribed to synthesize the first-strand cDNA using a combination of random hexamers and a poly-T chimeric primer. The RNA template is then partially degraded by heating and the second strand cDNA is synthesized using DNA polymerase. The double-stranded DNA is then amplified using single primer isothermal amplification (SPIA). SPIA is a linear cDNA amplification process in which RNase H degrades RNA in DNA/RNA heteroduplex at the 5′-end of the double-stranded DNA, after which the SPIA primer binds to the cDNA and the polymerase starts replication at the 3′-end of the primer by displacement of the existing forward strand. Random hexamers are then used to amplify the second-strand cDNA linearly. Finally, libraries from the SPIA amplified cDNA were made using the Ultralow DR library kit (NuGEN). After quality control analysis with a Bioanalyzer, the libraries were sequenced using a HiSeq 4000 instrument (Illumina), generating between 58 and 141 (average: 91) million reads/sample. Quality control was performed on base qualities and nucleotide composition of sequences. Alignment to the M. musculus (mm10) refSeq (refFlat) reference gene annotation was performed using the STAR spliced read aligner[5] with default parameters. Additional quality control was performed after the alignment to examine: the level of mismatch rate, mapping rate to the whole genome, repeats, chromosomes, key transcriptomic regions (exons, introns, UTRs, genes), insert sizes, AT/GC dropout, transcript coverage and GC bias. Between 87 and 90% (average: 89.3%) of the reads mapped uniquely to the mouse genome. Total counts of read-fragments aligned to candidate gene regions were derived using the HTSeq program

(www.huber.embl.de/users/anders/HTSeq/doc/overview.html) with mouse mm10 (Dec. 2011) refSeq (refFlat table) as a reference and used as a basis for the quantification of gene expression. Only uniquely mapped reads were used for subsequent analyses. Two samples (one *TREM2*$^{+/-}$ and one *TREM2*$^{-/-}$) with the lowest alignment rates and that clustered away from the remaining samples were excluded from subsequent analyses. After regressing by sex, Bioconductor packages edgeR[6] and limma-voom[7] were used for differential expression analysis, which included four *TREM2*$^{+/+}$, three *TREM2*$^{+/-}$, and three *TREM2*$^{-/-}$ replicates. The trimmed mean normalization (TMM) method was used to normalize the counts after excluding genes with 0 count across all samples/libraries. Statistical significance of the differential expression was determined at a p-value < 0.005. For figure 3, libraries were prepared using Lexogen's QuantSeq 3' mRNA-Seq Library Prep Kit, 4 replicates per genotype (total: 16 samples). Sequencing and analysis was performed in a similar manner as detailed above. RNAseq data has been deposited within the Gene Expression Omnibus (GEO) repository (www.ncbi.nlm.nih.gov/geo), accession number GSE107293.

Statistical analysis.

Data were analyzed with Graphpad Prism v.7 (GraphPad), STATA12 (StataCorp LP), or R (R Foundation for Statistical Computing). Multilevel mixed-effects linear regression model fit using STATA12 was used to compare curves for young and aged mice in response to injury. For cluster analyses of multiple measurements from individual mice, we used the R package lmer. Outliers were removed based on Graphpad's outlier analysis algorithm. All animals were included for statistical analyses unless otherwise noted.

2.10 References for Supplementary Text

1 Turnbull, I. R. *et al.* Cutting edge: TREM-2 attenuates macrophage activation. *J Immunol* **177**, 3520-3524 (2006).

2 Davalos, D. *et al.* ATP mediates rapid microglial response to local brain injury in vivo. *Nat Neurosci* **8**, 752-758, doi:10.1038/nn1472 (2005).

3 Krabbe, G. *et al.* Microglial NFkappaB-TNFalpha hyperactivation induces obsessive-compulsive behavior in mouse models of progranulin-deficient frontotemporal dementia. *Proceedings of the National Academy of Sciences of the United States of America*, doi:10.1073/pnas.1700477114 (2017).

4 Cho, S. H. *et al.* SIRT1 Deficiency in Microglia Contributes to Cognitive Decline in Aging and Neurodegeneration via Epigenetic Regulation of IL-1beta. *The Journal of neuroscience : the official journal of the Society for Neuroscience* **35**, 807-818, doi:10.1523/jneurosci.2939-14.2015 (2015).

5 Dobin, A. *et al.* STAR: ultrafast universal RNA-seq aligner. *Bioinformatics* **29**, 15-21, doi:10.1093/bioinformatics/bts635 (2013).

6 Robinson, M. D., McCarthy, D. J. & Smyth, G. K. edgeR: a Bioconductor package for differential expression analysis of digital gene expression data. *Bioinformatics* **26**, 139-140, doi:10.1093/bioinformatics/btp616 (2010).

7 Ritchie, M. E. *et al.* limma powers differential expression analyses for RNA-sequencing and microarray studies. *Nucleic Acids Res* **43**, e47, doi:10.1093/nar/gkv007 (2015).

2.11 Legends for Supplementary Movies

Movie S1 Video file showing microglial responses to a localized laser-induced injury *in vivo* in young *TREM2*$^{+/+}$, *TREM2*$^{+/-}$ and *TREM2*$^{-/-}$ mice over a 60-minute time period.

Movie S2 Video file showing microglial responses to a localized laser-induced injury *in vivo* in aged *TREM2*$^{+/+}$, *TREM2*$^{+/-}$ and *TREM2*$^{-/-}$ mice over a 60-minute time period.

2.12 Main Figures

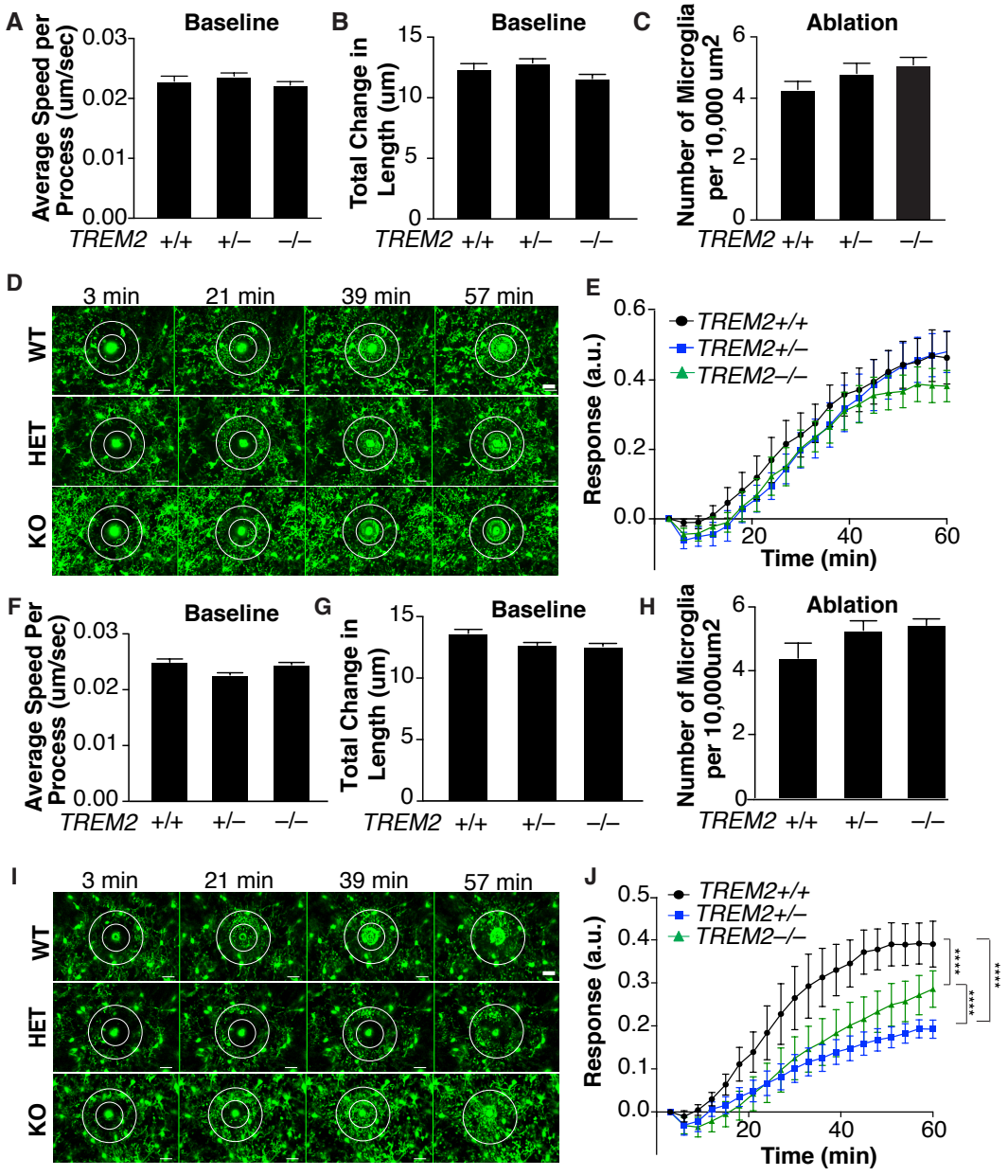

Figure 2.1 TREM2 haploinsufficiency causes an age-dependent impairment of microglia's injury response *in vivo*. (A–E) Quantification of microglial motility in 3-5-month old mice. Quantification of the average speed per microglial process (A) and total change in length of microglial processes (B) during 10-minute baseline recordings from 3- to 5-month-old mice. *TREM2*$^{+/+}$, n=7 recordings from 7 mice; *TREM2*$^{+/–}$, n=9 recordings from 9 mice; *TREM2*$^{–/–}$, n=10 recordings from 10 mice. (C) Microglial density for young mice from laser-induced tissue injury videos. *TREM2*$^{+/+}$, n=10 recordings from 9 mice; *TREM2*$^{+/–}$, n=11 recordings from 10 mice; *TREM2*$^{–/–}$, n=12 recordings from 10 mice. (D) Representative still images at 3 min, 21 min, 39 min and 57 min from the microglial responses to injury in young

mice. Laser ablations are outlined with smaller white circles. The response was normalized to microglial density at each time point, denoted by larger white circles. Scale bar: 20μm. (E) Quantification of normalized microglial responses from young mice towards focal laser-induced tissue injury over a period of 60 minutes from time of injury. *TREM2*$^{+/+}$, n=7 injuries from 7 mice; *TREM2*$^{+/-}$, n=11 injuries from 10 mice; *TREM2*$^{-/-}$, n =12 injuries from 10 mice. (F–K) Quantification of microglial motility in 9- to 14-month old mice. (F) Quantification of the average speed per microglial process and (G) total change in length of processes during 10-minute baseline recordings from 9-14-month old mice. *TREM2*$^{+/+}$, n=10 recordings from 7 mice; *TREM2*$^{+/-}$, n=10 recordings from 9 mice; *TREM2*$^{-/-}$, n=10 recordings from 9 mice. (H) Microglial density for aged mice during laser-induced tissue injury experiments. *TREM2*$^{+/+}$, n=7 recordings from 6 mice; *TREM2*$^{+/-}$, n=13 recordings from 10 mice; *TREM2*$^{-/-}$, n=12 recordings from 9 mice. (I) Representative still images at 3 min, 21 min, 39 min and 57 min from the microglial responses to injury in aged mice. Laser ablations are outlined with smaller white circles. Response size was normalized to microglial density at each time point, denoted by larger white circles. Scale bar: 20μm. (J) Quantification of normalized microglial responses from aged mice towards focal laser-induced tissue injury was measured over a period of 60 minutes from time of injury. *TREM2*$^{+/+}$, n=6 injuries from 5 mice; *TREM2*$^{+/-}$, n =13 injuries from 10 mice; *TREM2*$^{-/-}$, n =12 injuries from 9 mice. (****p<0.0001, STATA mixed-effects modeling). Values are expressed as mean ± SEM. Data were analyzed using one-way ANOVA with Bonferroni *post-hoc* analyses for all panels except for (E) and (J), which were analyzed using STATA mixed-effects modeling.

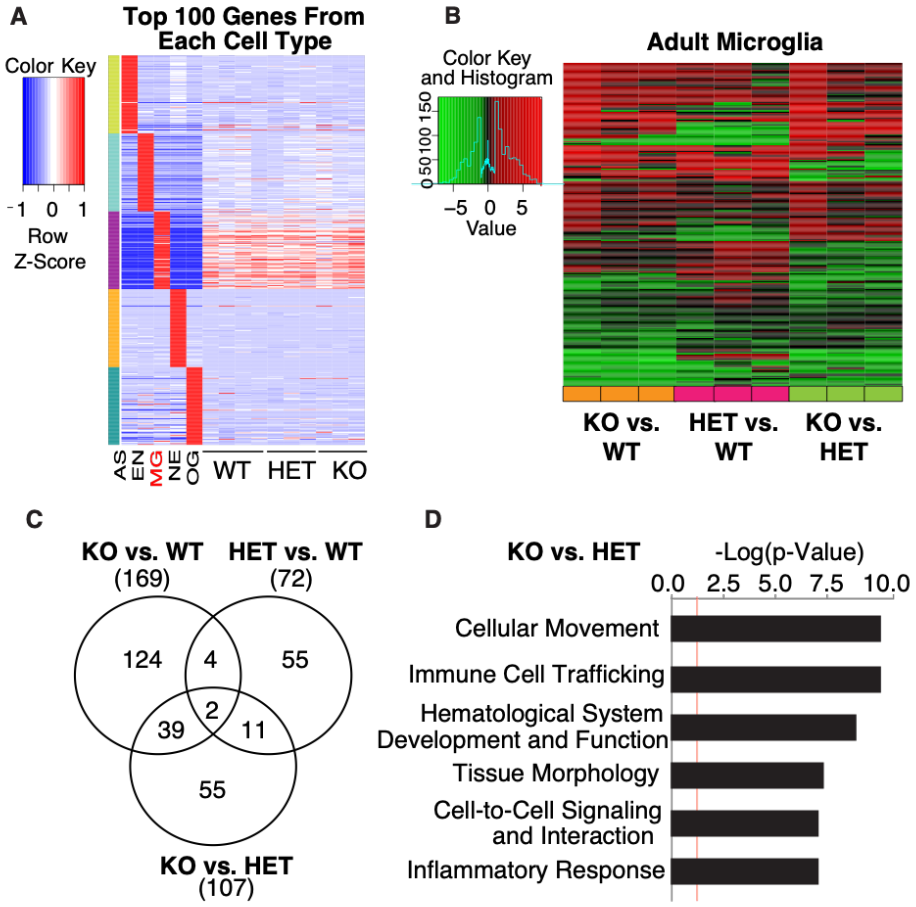

Figure 2.2 Differential effects of partial and complete loss of TREM2 on the microglial transcriptome. (A) RNA sequencing of microglia isolated from the forebrain of 3- to 4-month old mice (*TREM2*$^{+/+}$, n= 4 samples from 8 mice; *TREM2*$^{+/-}$, n= 3 samples from 6 mice; *TREM2*$^{-/-}$, n=3 samples from 6 mice). Expression levels of the top 100 most enriched transcripts in astrocytes (AS), endothelial cells (EN), microglia (MG), neurons (NE) and oligodendrocytes (OG), as identified by Zhang *et al.* (27). Columns 1-5: data from Zhang *et al.* Columns 6-15: expression data in microglia from *TREM2*$^{+/+}$, *TREM2*$^{+/-}$ and *TREM2*$^{-/-}$ mice. Shades of red correspond to increased levels compared to average gene expression and shades of blue correspond to decreased levels. (B) Heat map representing significantly altered transcripts ($p<0.005$) across all genotypes. Samples are in columns and genes are in rows. Shades of red represent upregulation, while shades of green represent downregulation. (C) Venn diagram illustrating the number and overlap of transcripts that were significantly altered between the two indicated genotypes ($p<0.005$). (D) Ingenuity pathway analysis (IPA^{TM}) of top six enriched disease and biological function pathways from 107 transcripts that were significantly altered in *TREM2*$^{-/-}$ microglia compared to *TREM2*$^{+/-}$ microglia ($p<0.005$). Bars indicate –log (p-value) of enrichment. Red dotted line corresponds to $p=0.05$.

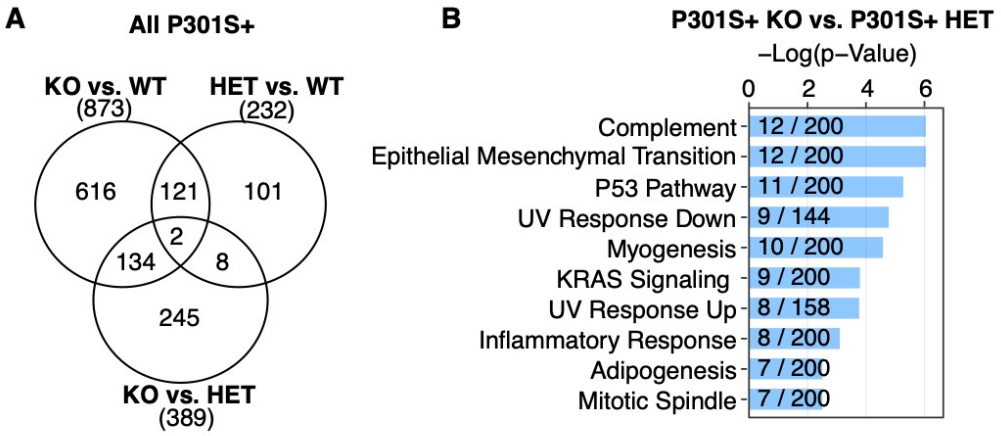

Figure 2.3 Differential effects of partial and complete loss of TREM2 on P301S-induced transcriptional changes. (A) Venn diagram illustrating the number and overlap of transcripts that were significantly altered between the two indicated P301S+ genotypes from 8- to 9-month-old mice ($p<0.005$, 4 mice/genotype, 1 mouse/sample). (B) GSEA analysis using the hallmark database on significant differentially expressed transcripts between partial versus complete loss of TREM2 in P301S mice. The top 10 most enriched pathways are shown. The fraction on the bar graph indicates the total number of genes curated in the database for the specified term (denominator) and the number of overlapping genes in the inputted RNAseq dataset (numerator).

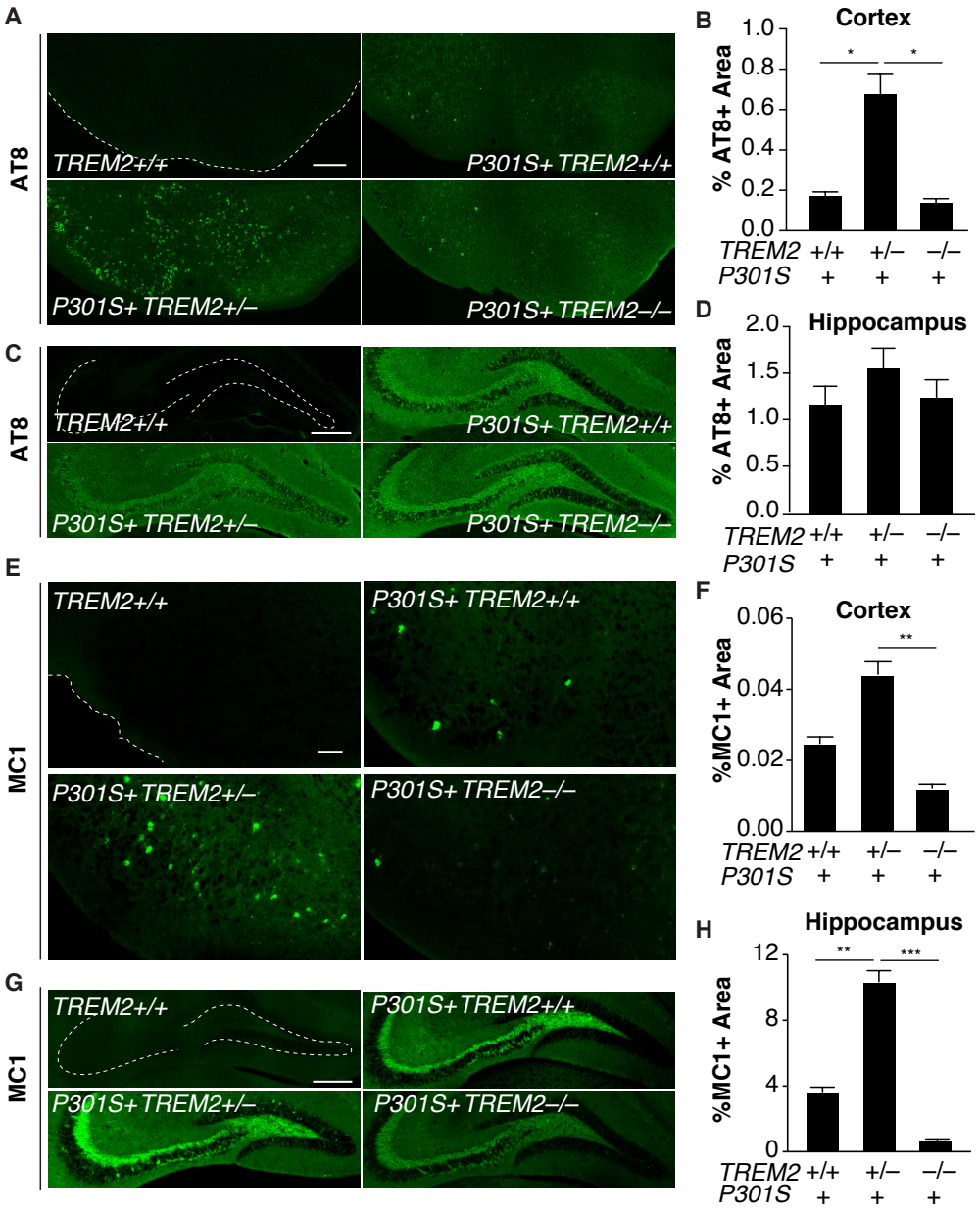

Figure 2.4 TREM2 haploinsufficiency exacerbates tau pathology in P301S+ mice. (A) Representative images of AT8 immunostaining in the cortex of 8- to 9-month-old mice. Scale bar: 100μm. (B) Quantification of the percentage of AT8+ area in the cortex of P301S+ *TREM2*$^{+/+}$, n=9 mice; P301S+ *TREM2*$^{+/–}$, n=25 mice; P301S+ *TREM2*$^{-/-}$, n=9 mice; 6-8 sections/mouse (*p<0.05, STATA mixed-effects modeling). (C) Representative images of AT8 immunostaining in the hippocampus of 8- to 9-month-old mice. Scale bar: 300μm. (D) Quantification of the percentage of AT8+ area in the hippocampus of P301S+ *TREM2*$^{+/+}$, n=9 mice; P301S+ *TREM2*$^{+/–}$, n=25 mice; P301S+ *TREM2*$^{-/-}$, n=10 mice; 6-8 sections/mouse. (E) Representative images of MC1 immunostaining in the cortex of 8- to 9-month-old mice. Scale bar: 300μm. (F) Quantification of the percentage of MC1+ area in the cortex of P301S+

TREM2$^{+/+}$, n=9 mice; P301S+ *TREM2*$^{+/-}$, n=25 mice; P301S+ *TREM2*$^{-/-}$, n=9 mice; 7-16 sections/mouse (**p<0.01, R mixed-effects modeling). (G) Representative images of MC1 immunostaining in the hippocampus of 8- to 9-month-old mice. Scale bar: 100µm. (H) Quantification of the percentage of MC1+ area in the hippocampus of P301S+ *TREM2*$^{+/+}$, n=9 mice; P301S+ *TREM2*$^{+/-}$, n=25 mice; P301S+ *TREM2*$^{-/-}$, n=10 mice; 7-16 sections/mouse (**p<0.01, ***p<0.001, R mixed-effects modeling). Values are expressed as mean ± SEM.

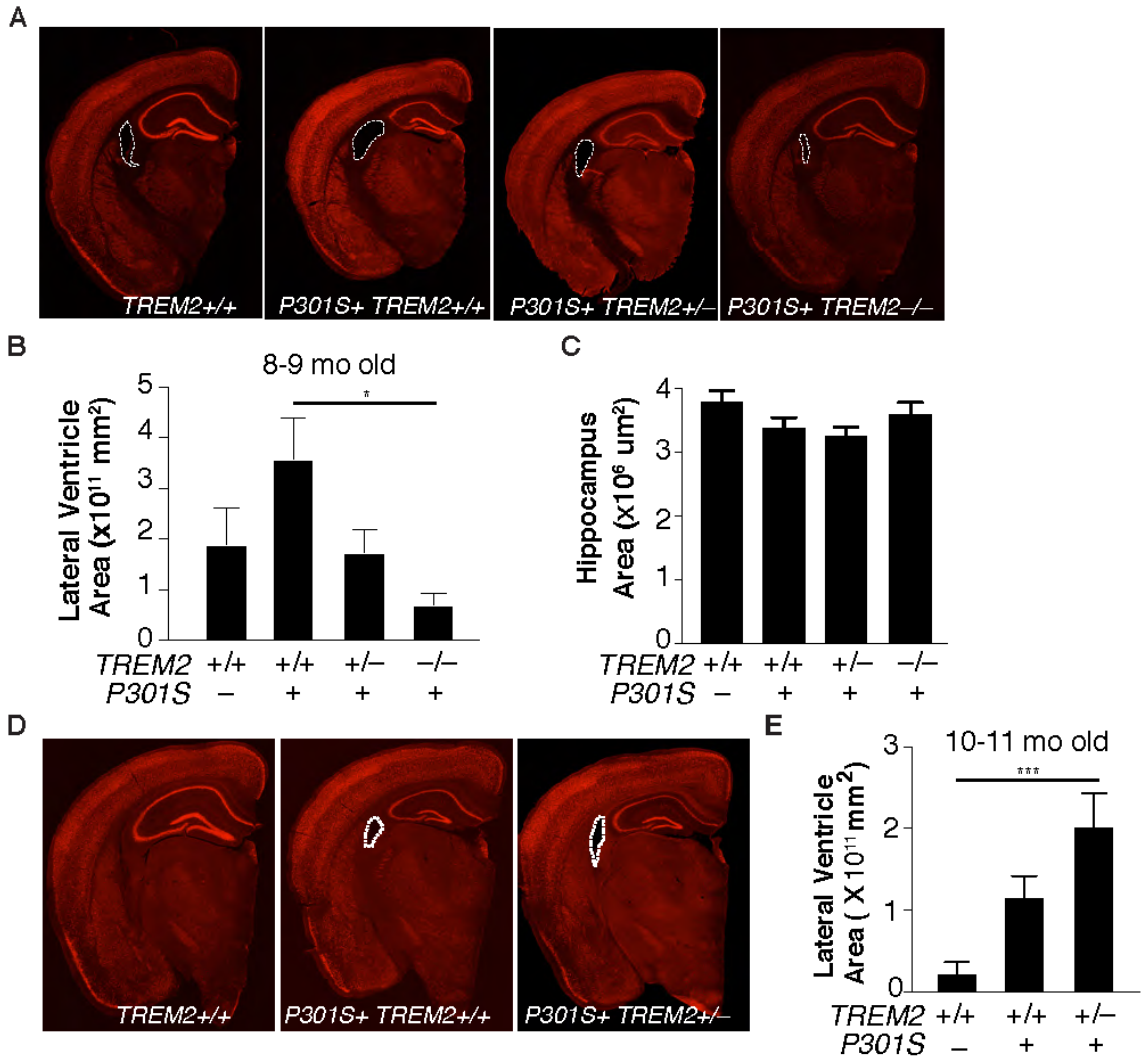

Figure 2.5 Differential effects of partial and complete loss of TREM2 on atrophy in P301S+ mice. (A) Representative images of NeuN immunostaining from 8- to 9-month-old mice. Lateral ventricle outlined with a white dashed line. (B) Quantification of the lateral ventricle area of *TREM2*$^{+/+}$, n=6 mice; P301S+ *TREM2*$^{+/+}$, n=9 mice; P301S+ *TREM2*$^{+/–}$, n=25 mice; P301S+ *TREM2*$^{-/-}$, n=10 mice, 6-17 sections/mouse (*p<0.05, one-way ANOVA with Bonferroni *post-hoc* analysis). (C) Quantification of the hippocampal area in 8- to 9-month-old *TREM2*$^{+/+}$, n=6; P301S+ *TREM2*$^{+/+}$, n=9; P301S+ *TREM2*$^{+/–}$, n=25; and P301S+ *TREM2*$^{-/-}$, n=10 mice, 6-17 sections/mouse. (D) Representative images of NeuN immunostaining from 10- to 11-month-old mice. Lateral ventricle outlined with a white dashed line. (E) Quantification of the lateral ventricle area of *TREM2*$^{+/+}$, n=12 mice; P301S+ *TREM2*$^{+/+}$, n=12 mice; P301S+ *TREM2*$^{+/–}$, n=11 mice; 6-8 sections/mouse (***p<0.001, one-way ANOVA with Bonferroni *post-hoc* analysis). Values are expressed as mean ± SEM.

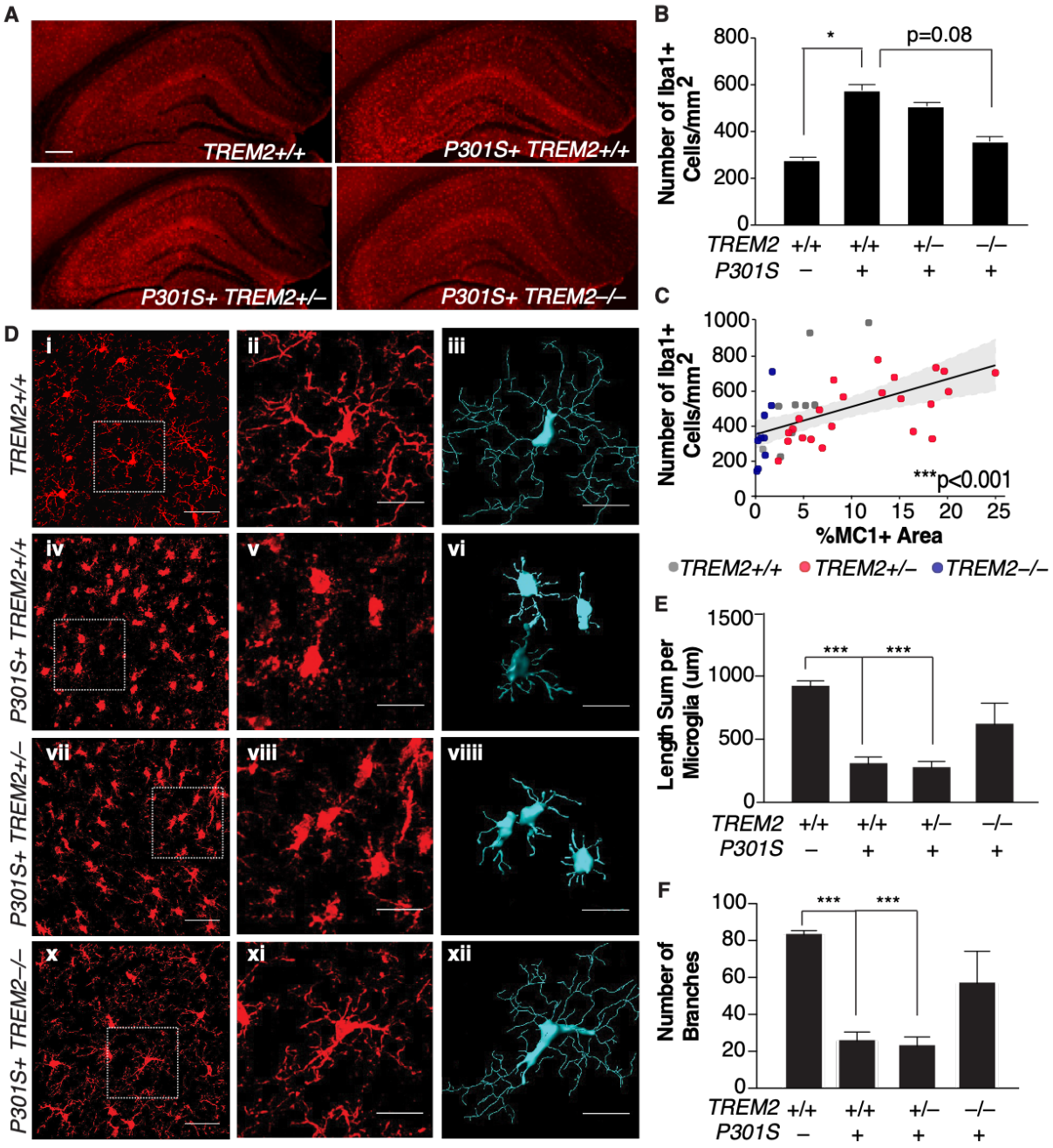

Figure 2.6 Differential regulation of inflammation by partial and complete loss of TREM2 in P301S+ mice. (A) Representative images of Iba1 immunostaining of microglia in the hippocampus of 8- to 9-month-old mice. Scale bar: 300μm. (B) Quantification of the number of microglia per millimeter squared in the hippocampus of *TREM2*$^{+/+}$, n=5 mice; P301S+ *TREM2*$^{+/+}$, n=9 mice; P301S+ *TREM2*$^{+/–}$, n=25 mice; P301S+ *TREM2*$^{-/-}$, n=10 mice; 6-17 sections/mouse (*p<0.05, R mixed-effects modeling). (C) Significant positive correlation between hippocampal percent MC1+ area and number of Iba1+ cells per mm^2 (***p<0.001, linear regression). Each dot represents one animal. Graph depicts mean and 95% confidence intervals. Genotypes are color-coded according to key. (D) Representative images of hippocampal Iba1 immunostaining

and the corresponding 3D reconstructions using Imaris. Scale bar for 1st column with full view images: 40µm. Scale bar for 2nd and 3rd columns with zoomed-in images: 20µm. (E) Quantification of the length sum of microglial processes and (F) number of microglial branches in *TREM2*$^{+/+}$, n=4 mice (35 cells); P301S+ *TREM2*$^{+/+}$, n=7 mice (123 cells); P301S+ *TREM2*$^{+/-}$, n=9 mice (169 cells); P301S+ *TREM2*$^{-/-}$, n=5 mice (64 cells) (*p<0.05, ***p<0.001, one-way ANOVA with Bonferroni *post-hoc* analysis). Values are expressed as mean ± SEM.

2.13 Supplementary Figures

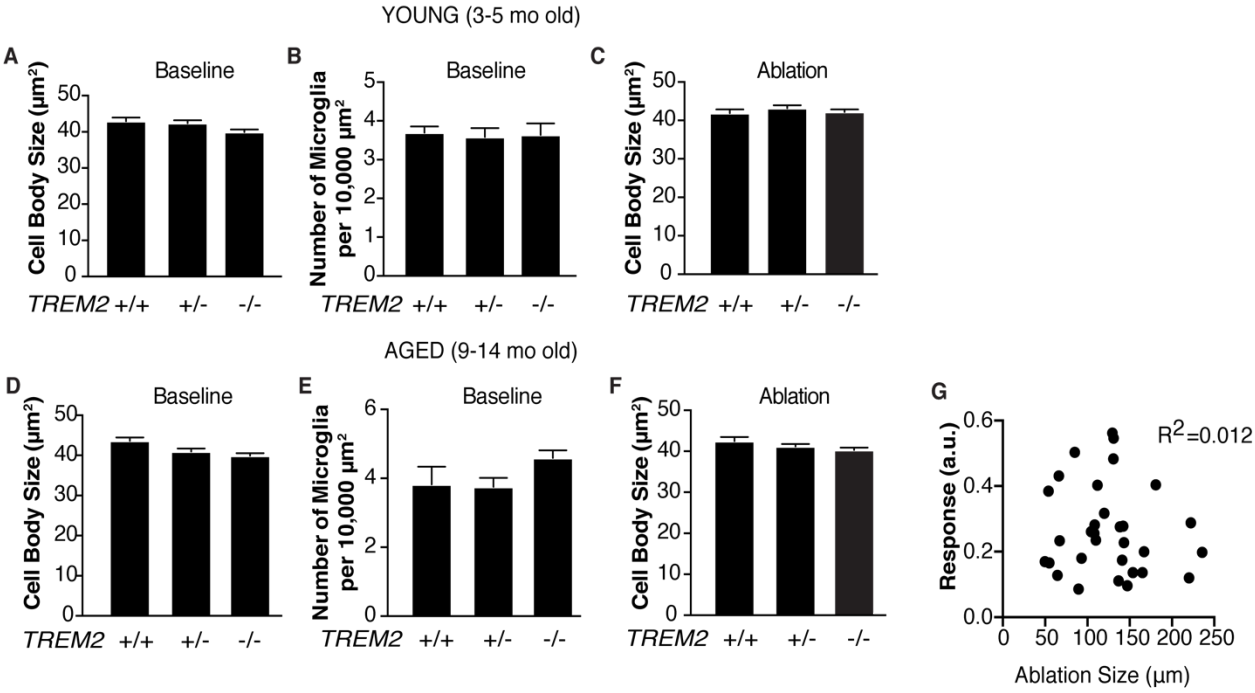

Figure S2.1 No difference in microglial cell density or cell body size across genotypes *in vivo.* (A) Microglial cell body size and (B) microglial cell density at baseline in young mice. *TREM2*$^{+/+}$, n=11 recordings from 10 mice; *TREM2*$^{+/-}$, n=12 recordings from 12 mice; *TREM2*$^{-/-}$, n=12 recordings from 11 mice. (C) Microglial cell body size during laser-induced injury in young mice. *TREM2*$^{+/+}$, n=10 recordings from 9 mice; *TREM2*$^{+/-}$, n=11 recordings from 10 mice; *TREM2*$^{-/-}$, n=12 recordings from 10 mice. (D) Microglial cell body size and (E) microglial cell density at baseline in aged mice. *TREM2*$^{+/+}$, n=8 recordings from 6 mice; *TREM2*$^{+/-}$, n=10 recordings from 9 mice; *TREM2*$^{-/-}$, n=14 recordings from 9 mice. (F) Microglial cell body size during ablation in aged mice. *TREM2*$^{+/+}$, n=7 recordings from 6 mice; *TREM2*$^{+/-}$, n=13 recordings from 10 mice; *TREM2*$^{-/-}$, n=12 recordings from 9 mice. Data were analyzed using one-way ANOVA with Bonferroni *post-hoc* analyses. (G) Lack of correlation between ablation size and response in aged mice, R^2=0.012. Values are expressed as mean ± SEM.

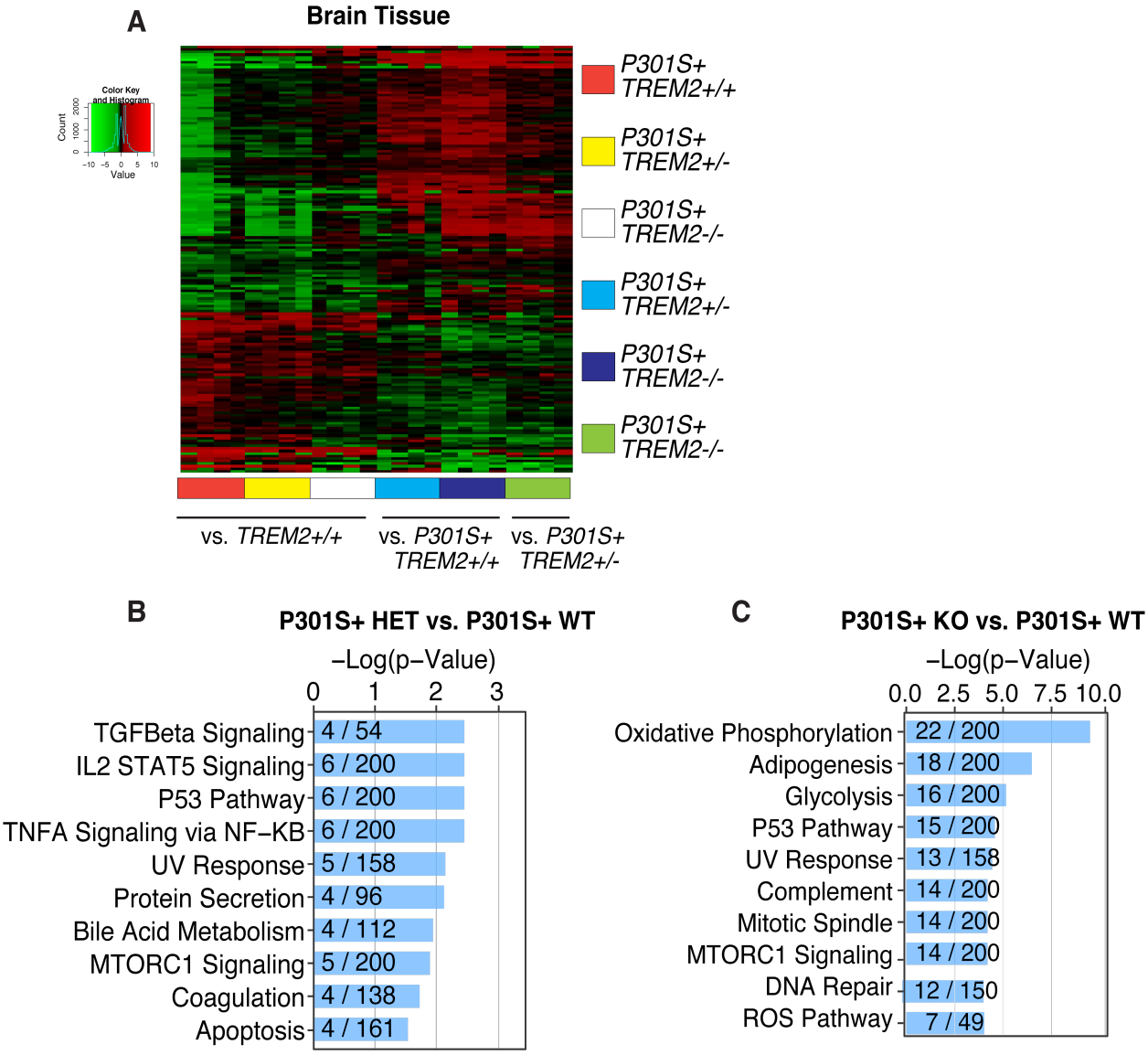

Figure S2.2 Differential effects of partial and complete loss of TREM2 on P301S-induced transcriptional changes. (A) RNA sequencing of brain tissue isolated from 8- to 9-month-old mice (4 mice/genotype, 1 mouse/sample). Heat map representing significantly altered transcripts ($p<0.005$) across all genotypes. Samples are in columns and genes are in rows. Shades of red represent upregulation, while shades of green represent downregulation. First three columns are all relative to *TREM2*$^{+/+}$. Next two columns are relative to P301S+ *TREM2*$^{+/+}$. Last column is a direct comparison between P301S+ *TREM2*$^{+/-}$ and P301S+ *TREM2*$^{-/-}$ (B–C) GSEA analyses using the hallmark database on significant differentially expressed genes between the indicated genotypes. The top 10 most enriched pathways are shown. The fraction on the bar graph indicates the total number of genes curated in the database for the specified term (denominator) and the number of overlapping genes in the inputted RNAseq dataset (numerator).

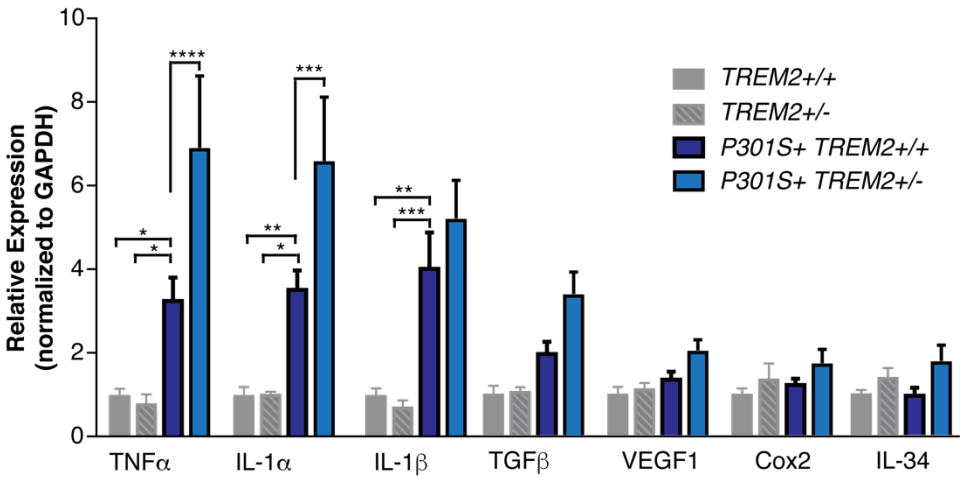

Figure S2.3 TREM2 haploinsufficiency increases levels of pro-inflammatory transcripts in P301S+ mice. Quantitative real-time PCR of pro- and anti-inflammatory markers in the cortex of 8- to 9-month-old *TREM2*$^{+/+}$, n=5 mice; *TREM2*$^{+/-}$, n=4 mice; P301S+ *TREM2*$^{+/+}$, n=7 mice; P301S+ *TREM2*$^{+/-}$, n=6 mice. Samples were run in triplicates and averages of the three wells were used for quantification, normalized to GAPDH (*p<0.05, **p<0.01, ***p<0.001, ****p<0.0001, two-way ANOVA with Bonferroni *post-hoc* analyses). Values are expressed as mean ± SEM.

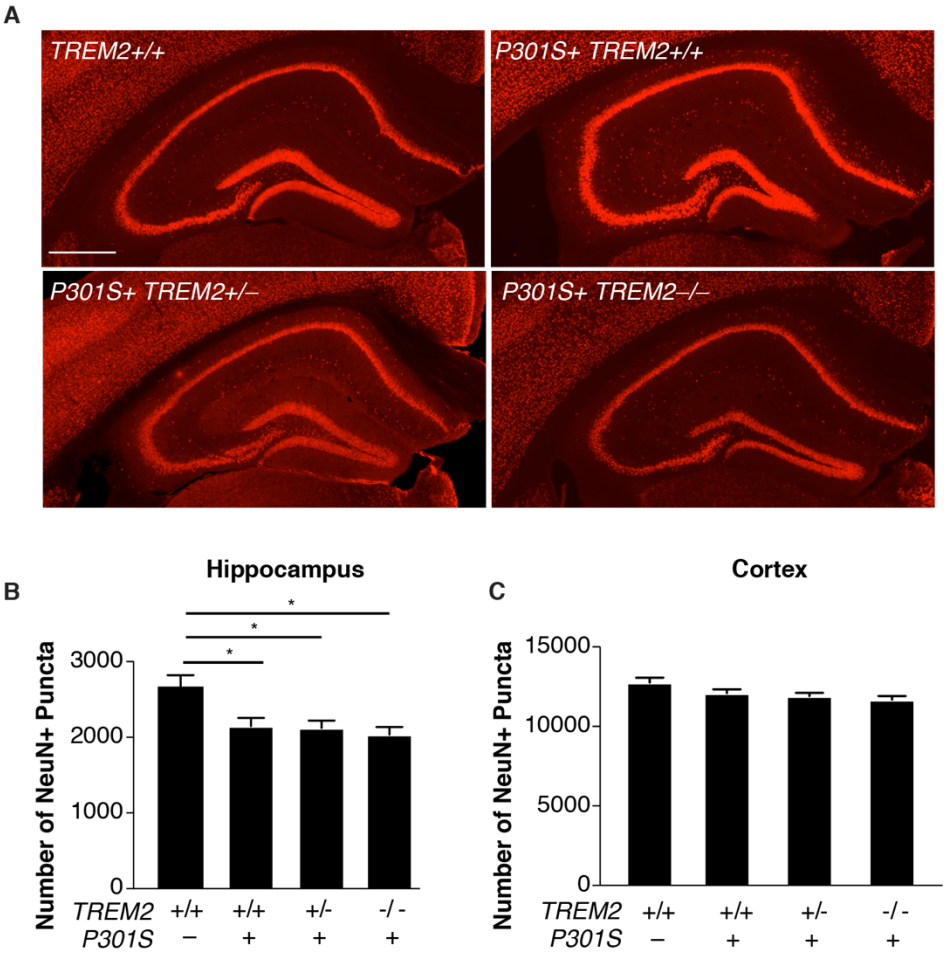

Figure S2.4 TREM2 deficiency does not affect the loss of NeuN-positive neurons in P301S+ mice. (A) Representative images of NeuN+ neuronal density in the hippocampus of 8- to 9-month-old mice. Scale bar: 300μm. (B) Quantification of the number of NeuN+ puncta in the hippocampus and (C) cortex in *TREM2*$^{+/+}$, n=6 mice; P301S+ *TREM2*$^{+/+}$, n=9 mice; P301S+ *TREM2*$^{+/-}$, n=25 mice; P301S+ *TREM2*$^{-/-}$, n=10 mice; 6-17 sections/mouse (*p<0.05, R mixed-effects modeling). Values are expressed as mean ± SEM.

Chapter 3: AD-linked TREM2 Mutation Induces Metabolic Changes in Neurons and Oligodendrocytes Associated with Toxicity

3.1 Abstract

The hemizygous R47H variant of *TREM2*, a microglia-specific gene in the brain, increases risk for late-onset Alzheimer's disease (AD). To understand its pathogenicity, we generated knock-in mice in which mouse *Trem2* was replaced with wild-type or R47H human *TREM2*. One allele of R47H-hTREM2 was sufficient to induce cognitive deficits and alter synaptic transmission. In knock-in mice with tau inclusions, R47H-hTREM2 exacerbated spatial learning and memory deficits only in female mice. Bulk, single-cell, and single-nuclei RNA-sequencing of hippocampal tissue from female mice revealed R47H-induced global non-cell autonomous effects. Single-nuclei RNA-sequencing of cortex from AD patients with and without R47H-TREM2 established transcriptomic changes in oligodendrocytes that correlated significantly with those observed in the R47H tauopathy mouse model. By unraveling disease-enhancing properties of the R47H mutation, our findings provide new directions for developing microglia-targeted AD therapies.

3.2 Introduction

Alzheimer's disease (AD) is the most common form of late-onset dementia. In addition to the pathological hallmarks of amyloid plaques and neurofibrillary tangles composed of hyperphosphorylated tau, AD is also characterized by increased microglial activation and an upregulation of cytokines in the brain. These aberrant microglial phenotypes in AD have been largely considered responses to the toxic buildup of plaques and tangles. However, genome-wide association studies have identified many risk alleles for late-onset sporadic AD that are highly expressed in microglia[1-4], suggesting that microglial dysfunction can contribute to AD

pathogenesis. Among these risk alleles is *TREM2*, the strongest immune-gene risk factor identified to date. A heterozygous point mutation in *TREM2*, the R47H variant, significantly increases risk for late-onset AD[1,2].

TREM2 is a single transmembrane receptor expressed exclusively in cells of the myeloid lineage, especially microglia[5,6]. Upon ligand engagement, TREM2 activates downstream protein tyrosine phosphorylation through its adaptor DAP12/TYROBP and stimulates proliferation, phagocytosis, survival, and mTOR signaling[7-13]. While the exact ligands in the brain remain elusive and are likely to be context-dependent, TREM2 binds *in vitro* to apoptotic cells[14], anionic ligands [9,15], apolipoproteins[16-18], and amyloid-beta[19]. Cleavage of TREM2 by metalloproteinases releases soluble TREM2[20-22], which may mediate microglial cell survival and inflammation[23,24].

TREM2 studies in amyloid or tau mouse models have largely focused on mouse *Trem2* (*mTrem2*) deficiency. In amyloid mouse models, *mTrem2* deficiency weakens the microglial response to amyloid plaques, impairs the microglial barrier, and worsens amyloid toxicity[25-27]. In tau mouse models, however, *mTrem2* deficiency protects against tau-induced atrophy[28,29], highlighting the complexity of the TREM2-mediated microglial response in AD brains.

Little is known about how the R47H mutation contributes to AD. The prevailing hypothesis is that R47H causes only a partial loss-of-function. For instance, *mTrem2* deficiency markedly reduces microglial coverage of amyloid plaques, whereas expression of R47H human *TREM2* (R47H-hTREM2) has a much milder effect[30]. The R47H variant also causes subtler deficits in the shedding and maturation of soluble TREM2, protein stability, phagocytosis, and surface TREM2 expression[21,31]. Moreover, *mTrem2* knockout macrophages have a more pronounced transcriptional response to reduced levels of CSF1 than homozygous R47H macrophages[12]. Of note, the R47H variant impairs ligand binding to a lesser extent than loss-of-function mutations linked to Nasu-Hakola disease[16-18]. Indeed, human genetics also suggests that the loss-of-function effects of the R47H variant do not fully explain its role in AD, as

homozygous loss-of-function mutations in *TREM2* cause Nasu-Hakola disease[32], whereas homozygous R47H-TREM2 carriers develop AD[33].

Understanding the pathogenic mechanisms of R47H-TREM2 in AD is of critical importance for microglia-targeted therapeutic approaches. If R47H-TREM2 induces AD risk through loss-of-function, TREM2-enhancing therapies would be effective. Conversely, if R47H-TREM2 induces AD risk through gain-of-toxic function, then those toxic pathways would need to be inhibited. In this study, we used CRISPR to knock-in WT or R47H-*hTREM2* to replace one allele of *mTrem2* in mice. Using a combination of behavioral, electrophysiological, and RNA-sequencing approaches, we sought to dissect the disease-enhancing mechanisms of the R47H mutation.

3.3 Results

Heterozygous R47H-hTREM2 Induces Aberrant Hippocampal Synaptic Transmission and Impairs Spatial Memory

Using CRISPR, we generated two knock-in mouse lines expressing one copy of WT (*hTREM2*$^{WT/+}$) or R47H-*hTREM2* (*hTREM2*$^{R47H/+}$) cDNA in place of *mTrem2* (Figure 1a). *hTREM2*$^{WT/+}$ and *hTREM2*$^{R47H/+}$ mice had equivalent levels of hTREM2 mRNA (Figure 1b) and protein (Figure 1c-d) and a dose-dependent reduction in mTrem2 mRNA levels (Figure 1e), indicating successful replacement of *mTrem2* by *hTREM2*. The matched levels of WT and R47H-hTREM2 mRNA and protein allowed us to assess the consequences of the AD-associated heterozygous R47H variant *in vivo*.

We first examined whether a single allele of R47H-*hTREM2* in mice causes hippocampal synaptic impairment. We performed field recordings in the molecular layer of the dentate gyrus while stimulating the perforant pathway in the hippocampus of 6.5- to 9-month-old mice. The synaptic response to increasing stimulus intensity was similar in *hTREM2*$^{WT/+}$ and *mTrem2*$^{+/+}$ (wild-type) controls, but was significantly greater in *hTREM2*$^{R47H/+}$ mice (Figure 1f). Thus,

synaptic transmission in the perforant pathway was increased by the R47H mutation specifically, and not simply by the expression of human TREM2. The mutation did not affect the mean amplitude of the fiber volley, consistent with the lack of effect on action potentials generated by the presynaptic fibers (Figure 1g). Nor did it affect the sustained increase in the postsynaptic response upon induction of long-term potentiation (Figure 1h), highlighting the highly specific alterations induced by R47H-*hTREM2* microglia on hippocampal circuitry.

To examine effects of R47H-*hTREM2* on spatial learning and memory, we tested *mTrem2*$^{+/+}$, *hTREM2*$^{WT/+}$, and *hTREM2*$^{R47H/+}$ mice in a hippocampus-dependent assay, the Morris water maze. At 7 to 9 months of age, all three genotypes had similar latencies to reach the target quadrant during training (Figure 1i), indicating normal spatial learning. However, during the 24-hour probe trial, R47H-*hTREM2* mice made more search errors (Figures 1j) and spent significantly less time in the target quadrant than wild-type mice (Figure 1k), indicating that R47H-*hTREM2* microglia impair spatial memory. Interestingly, female *hTREM2*$^{R47H/+}$ mice were significantly more impaired in spatial learning and memory than males (Supplementary Figure 1, a-f). The memory deficits were induced specifically by the R47H mutation, as *hTREM2*$^{WT/+}$ and *mTrem2*$^{+/+}$ mice performed identically regardless of sex (Supplementary Figure 1, g-l).

To rule out hyperactivity and anxiety, which could confound the spatial memory test results, we examined the mice in the open field and elevated plus maze assays. *hTREM2*$^{R47H/+}$, *hTREM2*$^{WT/+}$, and *Trem2*$^{+/+}$ mice did not differ in their activity levels in the open field (Supplementary Figure 2, a-d) nor in the percentage of time spent in the open arms of the elevated plus maze (Supplementary Figure 2, e-h). Taken together, our findings suggest that the hippocampal circuitry and spatial memory are particularly vulnerable in *hTREM2*$^{R47H/+}$ mice.

R47H-hTREM2 Induces Unique Transcriptional Changes in Neurons and Oligodendrocytes

To dissect how R47H induces functional deficits, we performed single-nuclei RNA-sequencing (snRNA-seq) of mouse hippocampal tissue isolated from 9-month-old *mTrem2*$^{+/+}$ and *hTREM2*$^{R47H/+}$ female mice. We sequenced 33,178 nuclei and used 31,783 cells that passed stringent quality control, including total gene count, total molecule count, and the percentage of mitochondrial RNA (Supplementary Figure 3), for downstream analysis. Unsupervised clustering revealed 11 transcriptionally distinct populations that were categorized as 8 major cell lineages using known cell type marker genes[34,35] (Figure 2a).

Visualizing the data by genotype revealed no differences in the densities of the cell types between genotypes (Figure 2b). We did not see many alterations in microglial transcriptome and number with the R47H mutation (Figure 2, c-d). Immunohistochemical findings also confirmed similar microglial densities and morphologies in 8- to 9-month-old *hTREM2*$^{WT/+}$ and *hTREM2*$^{R47H/+}$ mice (Supplementary Figure 4, a-g). Microglial motility, using *in vivo* imaging[29], also showed little difference at 12–17 months of age, regardless of hTREM2 mutation status. Baseline velocities of *hTREM2*$^{WT/+}$ and *hTREM2*$^{R47H/+}$ microglial processes were similar to those of *mTrem2*$^{+/+}$controls, as were the responses to laser-induced injury (Supplementary Figure 4, h-j, Supplementary Movie 1). This finding was in contrast to our observation in *mTrem2*$^{+/-}$ microglia, which exhibited a marked impairment in response to laser-induced injury[29], suggesting that the heterozygous R47H variant does not induce loss-of-function in the context of microglia's response to acute tissue injury.

Unlike microglia, neurons and oligodendrocytes showed dramatic changes in their transcriptional profiles (Figure 2d). Using Ingenuity pathway analysis, we identified the top upstream regulators for these cell types (Figure 2, e-g). Interestingly, the top two significantly activated upstream regulators across all three cell types modulate oxidative phosphorylation (CAB39L, HBA1/HAB2). The upstream regulator associated with the most significant decrease

in activity across all three cell types, RICTOR, modulates cell growth. Ingenuity pathway analysis of the differentially expressed genes (DEGs) in neurons and oligodendrocytes revealed a striking overlap in the top impacted pathways for each cell type (Figure 2h), in line with the overlap in upstream regulators. The most significantly enriched pathway in excitatory neurons, inhibitory neurons, and oligodendrocytes was oxidative phosphorylation (Figure 2h), suggesting altered cellular metabolism in these cell types. The other enriched pathways included EIF2, sirtuin, mTOR and synaptogenesis signaling pathways, highlighting the non-cell autonomous impact of R47H-hTREM2-expressing microglia.

R47H-hTREM2 Exacerbates Spatial Learning and Memory Deficits and Inflammatory Responses in Female Tauopathy Mice

The R47H variant significantly increases risk for AD, and cognitive deficits in AD correlate more strongly with tau load than with amyloid plaques[36,37]. To assess the effect of R47H-hTREM2 on tau pathology, we crossed *hTREM2*$^{WT/+}$ and *hTREM2*$^{R47H/+}$ mice with P301S mice, which express a mutant human tau gene and develop hallmarks of tauopathy, including gliosis, tau inclusions, and cognitive deficits[38]. At 7 to 9 months of age, when cognitive deficits manifest in P301S mice, the spatial learning curve of P301S *hTREM2*$^{WT/+}$ mice did not differ from that of P301S *mTrem2*$^{+/+}$ mice regardless of sex (Supplementary Figure 5), confirming again that WT-*hTREM2* behaves identically to *mTrem2*. In contrast, R47H-*hTREM2* significantly impaired spatial learning in female P301S mice, but had no effect in males (Figure 3, a–b). Female P301S *hTREM2*$^{R47H/+}$ mice also made significantly more search errors during the 72-hour probe trial than controls (Figure 3c). In contrast, male P301S *hTREM2*$^{R47H/+}$ mice trended toward fewer search errors during the probe trial (Figure 3d). Overall activity (Supplementary Figure 6, a-d) and anxiety levels (Supplementary Figure 6, e-h) were unaltered by the R47H mutation in either sex, suggesting that spatial learning and memory are specifically impacted by R47H-*hTREM2*.

These sex-dependent behavioral deficits were also associated with sex-dependent pathological findings. Tauopathy is characterized by an accumulation of insoluble tau aggregates detectable with a confirmation-specific antibody, such as MC1[39]. To directly compare the effects of R47H to WT hTREM2, we normalized tau loads to those of their respective P301S *mTrem2*$^{+/+}$ (P301S) littermate controls. For confirmation-specific tau aggregates (MC1), P301S *hTREM2*$^{R47H/+}$ males showed a modest trend toward increased MC1 density, while females showed a trend toward decreased density in the cortex (Supplementary Figure 7, a-c, j-l). Inflammation and alterations in microglial morphology occur early in P301S mice[38] and were also sex-dependent in R47H-hTREM2 mice. In males, there was a modest trend toward reduced microglial density in the cortex of P301S *hTREM2*$^{R47H/+}$ mice compared to P301S *hTREM2*$^{WT/+}$ mice (Supplementary Figure 7, d-f). Cell morphological analysis revealed that male P301S *hTREM2*$^{R47H/+}$ microglia had significantly longer processes and significantly more branches (Supplementary Figure 7, g-i), indicating a more resting microglial state. In female P301S mice, R47H-hTREM2 significantly reduced the number of microglia in the cortex without affecting microglial density or morphology in the hippocampus (Supplementary Figure 8, m-r). Thus, R47H-hTREM2 also affected microglia and tau pathology in a sex-dependent manner, similar to the behavioral deficits.

We next sought to identify potential molecular pathways underlying the sex-dependent effect of R47H-*hTREM2* on tau-mediated learning and memory deficits. We performed bulk RNA-sequencing (RNA-seq) of the hippocampus from 7- to 9-month-old male and female P301S *hTREM2*$^{R47H/+}$ mice and their littermate P301S *mTrem2*$^{+/+}$ controls. Analyses of the DEGs revealed that R47H-*hTREM2* induced significant transcriptomic changes in females, including upregulation of several disease-associated microglial (DAM) genes (e.g., Ccl6, Clec7a, Siglec5, Cd9, Cd63)[40] and other inflammatory genes (e.g., Cxcl5, Ccl9), and downregulation of neuron-associated genes (e.g., Adora2a, Syt6, Serpina9, Penk) (Figure 3e). In contrast, R47H-*hTREM2* induced few transcriptional changes in male P301S mice (Figure

3f), consistent with the lack of a significant effect of R47H-*hTREM2* on cognitive deficits in male P301S mice (Figure 3b,d). To identify biological networks associated with the detrimental effects of the R47H variant, we performed weighted gene-correlation network analysis (WGCNA) of the transcriptomes of female P301S *hTREM2*$^{WT/+}$ and P301S *hTREM2*$^{R47H/+}$ mice and their P301S *mTrem2*$^{+/+}$ littermate controls (Figure 3g). Two correlational modules exhibited statistically significant positive or negative correlations with the P301S *hTREM2*$^{R47H/+}$ mice (Figure 3g). The positive (brown) module was significantly enriched in microglial genes (Figure 3h), namely transcripts encoding cytokines, cytokine receptors, and chemokines (e.g., Ccr5, Ccl5, Ccl3, Cxcl5) (Figure 3, i-j). The negative (cyan) module was significantly enriched in neuronal genes (Figure 3h), such as transcripts encoding axon guidance molecules (e.g., Sema6b, Sema3f, Epha8, Ephb6) (Figure 3i). This downregulation of hippocampal neuronal transcripts is consistent with the worsened spatial learning and memory observed in P301S *hTREM2*$^{R47H/+}$ female mice.

R47H-hTREM2 Increases the Disease-Associated Microglia Signature in Female Tauopathy Mice

In AD mouse models with amyloid pathology, *mTrem2* deficiency blocked expression of a subset of DAM genes[40]. Interestingly, some of these TREM2-dependent DAM genes were significantly upregulated in P301S *hTREM2*$^{R47H/+}$ mice (e.g., Cd9, Clec7a, Ccl6) (Figure 3e), suggesting that the R47H mutation differs from the *mTrem2* deficiency model. To further probe these microglial signatures, we turned to deep single-cell RNA-seq[41]. We sorted microglia from the hippocampal tissue of 8-month-old female *mTrem2*$^{+/+}$, *hTREM2*$^{R47H/+}$, P301S, and P301S *hTREM2*$^{R47H/+}$ mice, gating on CD45^{low}CD11b^{+} (Supplementary Figure 8a). Out of the 1,480 cells that were sorted, 1,424 passed quality control (Supplementary Figure 8, b-d). Unsupervised clustering of these 1,424 cells yielded two clusters (Figure 4a). While cluster 1 microglia were found in all 4 genotypes, cluster 2 microglia were mainly found in the presence of

P301S (Figure 4b) and this population was further significantly enriched in P301S *hTREM2*$^{R47H/+}$ mice (Figure 4c). A more detailed analysis of cluster 2 revealed that the most significantly upregulated transcripts included several DAM transcripts, such as Clec7a, Ctsb, Axl, Cst7, Apoe, and Cd63 (Figure 4d). While both cluster 1 and 2 expressed homeostatic microglial genes, such as P2ry12 and Hexb, DAM transcripts Apoe and Cst7 were mainly localized to cluster 2 (Figure 4e). Indeed, there was a statistically significant correlation between cluster 2 DEGs and DAM transcripts, whereby all but four of the upregulated transcripts in cluster 2 were also upregulated in DAM (Figure 4f). Upregulation of Apoe in microglia was validated by RNAscope, whereby P301S *hTREM2*$^{R47H/+}$ exhibited a significant increase in the percentage of ApoE+ C1qa+ cells in the dentate gyrus (Figure 4, g-i). In sum, R47H-*hTREM2* expression in female tauopathy mice resulted in a significant increase in cluster 2 microglia, which were enriched for DAM-associated genes.

R47H-hTREM2 Induces Unique Transcriptional Changes in Neurons and Oligodendrocytes in Female Tauopathy Mice

To determine how these transcriptomic changes in *hTREM2*$^{R47H/+}$ microglia affected other cell types in the brain in the context of tauopathy, we performed single-nuclei RNA-seq (snRNA-seq) of mouse hippocampal tissue isolated from 9-month-old P301S and P301S *hTREM2*$^{R47H/+}$ female mice. We sequenced 33,178 nuclei and used 31,783 cells that passed quality control (Supplementary Figure 9) for downstream analysis. Unsupervised clustering revealed 11 transcriptionally distinct populations that were categorized as 8 major cell lineages using known cell type marker genes[34,35] (Figure 5a). R47H-*hTREM2* reduced the excitatory neuron cluster and expanded the oligodendrocyte cluster in female tauopathy mice (Figure 5, b–c). Compared to the single-nuclei data in the absence of tauopathy (Figure 2), we found greater numbers of DEGs induced by R47H-*hTREM2* across all cell types. However, similar to the data in the absence of tauopathy, we again found that neurons and oligodendrocytes had the

greatest number of DEGs (Figure 5d), suggesting that they are especially impacted by R47H-*hTREM2.*

Similar to what was observed in the absence of tauopathy, two of the top activated upstream regulators across excitatory neurons, inhibitory neurons, and oligodendrocytes were CAB39L and HBA1/HBA2, regulators of oxidative phosphorylation. Pathway analysis of the neuronal and oligodendrocyte DEGs showed similar changes in cellular pathways, with the exception of the mTOR signaling pathway which was upregulated in oligodendrocytes but downregulated in neurons (Figure 5h). Notably, sirtuin signaling oxidative phosphorylation showed the same directionality of change in nontransgenic and P301S mice in all cell types (Figure 2h, 5h). Altogether, these transcriptional changes highlight dysregulation of the oxidative phosphorylation pathway in neurons and oligodendrocytes in R47H-*hTREM2* mice.

R47H TREM2 Microglia Impact Metabolic Pathways in Oligodendrocytes in Human AD Brains

Lastly, we dissected cell-type-specific molecular pathways induced by R47H-TREM2 microglia in human AD and compared them with our R47H-TREM2 tauopathy mouse model. We performed snRNA-seq of frontal and temporal cortices from 3 AD brains, 3 R47H-AD brains, and 3 control brains from both men and women (Figure 6a). Using an established human snRNA-seq protocol[35], we sequenced 111,185 nuclei and used 102,702 cells that passed quality control (Supplementary Figure 10, a-b). for downstream analysis. Using reference gene sets for cluster annotations[42,43] (Supplementary Figure 10, c-d), we identified all the major cell types in the brain (Supplementary Figure 10e). Cells from frontal and temporal cortices contributed equally to all major cell types identified (Supplementary Figure 10f), with some variability across individuals in the proportion of cells in each cluster (Supplementary Figure 10g).

Plotting the three patient populations on separate t-SNEs revealed a differential distribution of cells across the 7 major clusters (Figure 6b). Notably, similar to what we observed in our mouse model, neurons and oligodendrocytes had the greatest number of DEGs in R47H-AD versus AD patients, with oligodendrocytes having close to 10,000 DEGs, 6,718 of which were upregulated (Figure 6c). To probe the transcriptional overlap between our mouse and human datasets, we focused on glial cells, as different neuronal populations were sampled between the mouse and human experiments. The greatest number of overlapping DEGs was in oligodendrocytes (Figure 6d). Ingenuity pathway analysis of the overlapping upregulated DEGs in oligodendrocytes highlighted the same pathways we observed in R47H-hTREM2 mice: EIF2, sirtuin, oxidative phosphorylation, and mTOR signaling, with mitochondrial dysfunction emerging as the most significantly enriched pathway, followed by oxidative phosphorylation (Figure 6e). Multiple components of the oxidative phosphorylation pathway were found in the overlapping dataset (Figure 6f), indicating that this pathway in oligodendrocytes is especially impacted by R47H-hTREM2. Overall, these findings indicate that oligodendrocytes are particularly affected by the R47H variant, and that the oligodendrocyte oxidative phosphorylation pathway altered by R47H appears to be conserved between our tauopathy mouse model and human patients.

3.4 Discussion

In this study, we generated hTREM2 knock-in mouse models with matched levels of WT and R47H hTREM2, which allowed us to model TREM2 R47H heterozygosity in mice to mimic human AD R47H carriers. We found that introduction of human TREM2 did not alter cellular transmission or behavior, as WT-hTREM2 mice behaved similarly to *mTrem2*$^{+/+}$ mice in both the presence and absence of tau pathology. These findings suggest that human TREM2 behaves similarly to mouse Trem2. The heterozygous R47H mutation alone was sufficient to cause behavioral and synaptic deficits and exacerbate tau-mediated spatial learning and memory, but only in female mice. Notably, these sex-dependent effects of R47H-*hTREM2* were associated

with sex-dependent transcriptomic changes. We also found that R47H-*hTREM2* mice differed from Trem2 haploinsufficient mice in microglia's response to injury, tau load, and global transcriptomics, which argues against the R47H variant as a pure loss-of-function mutation in the context of tauopathy. R47H-*hTREM2* altered the transcriptome of many cell types in the brain of female tauopathy mice, causing increased expression of DAM genes in microglia, and mitochondrial changes in neurons and oligodendrocytes. The single-nuclei RNA-seq analyses of cortices from AD patients with and without the R47H mutation revealed multiple pathways in oligodendrocytes that were altered by R47H-*hTREM2*. Moreover, there was a significant correlation between human oligodendrocyte DEGs and those in our P301S *hTREM2*$^{R47H/+}$ mouse model, underscoring the relevance of our new R47H-*hTREM2* mouse model for the study of AD.

Our mouse model is unique in that the matched mRNA and protein levels of the WT and R47H human TREM2 mouse lines allow us to specifically interrogate the effect of the R47H variant, in the absence of any overexpression or splicing artifacts. Two other R47H mouse models exist to date: a BAC transgenic overexpressing the common or R47H human TREM2 variant on a mouse Trem2 knockout background[30], and a CRISPR approach that introduced the single nucleotide change in the endogenous mouse Trem2 gene[44]. The latter model resulted in a 42% reduction in mouse Trem2 mRNA levels due to alternative splicing that occurs in mouse, but not human tissue, with the R47H variant[45]. Both models were used to study R47H-*hTREM2* in the context of amyloid pathology. Overall in both models, R47H exhibited mild deficits with respect to microglial density and cell survival, and did not impact overall plaque load[30,44]. Similarly, we found subtle effects of R47H-*hTREM2* on microglial density and tau pathology in our model.

R47H-*hTREM2* in microglia increased the size of the excitatory postsynaptic potentials evoked in the dentate granule cells and was associated with an enrichment of the synaptogenesis signaling pathway in excitatory neurons. The increase in EPSP slope could be

due to an increase in postsynaptic responsiveness or in the number of synapses. TREM2 promotes synapse pruning during development, and mice lacking Trem2 exhibit an increased frequency of miniature excitatory postsynaptic potentials[46]. Therefore, it is conceivable that R47H-*hTREM2* microglia could alter synaptic function by impairing TREM2's role in synapse pruning.

Using single-nuclei RNA-seq, we identified significant changes in neurons and oligodendrocytes in *hTREM2*$^{R47H/+}$ mice in the absence of tau pathology. These pathways were also altered in P301S *hTREM2*$^{R47H/+}$ mice, indicating that they may be key to understanding the pathogenicity of R47H-*hTREM2*. Oxidative phosphorylation was upregulated in oligodendrocytes and neurons from R47H-*hTREM2* mice in the absence and presence of tauopathy, suggesting altered metabolism in these cell types. Indeed, CAB39L and HBA1/HBA2, the top predicted upstream regulators in neurons and oligodendrocytes with and without tauopathy, are regulators of mitochondrial genes. Altogether, these transcriptional changes, along with the aberrant hippocampal synaptic transmission observed in R47H-*hTREM2* mice, point to metabolism as a pathway that may be particularly vulnerable to R47H-*hTREM2* expression and warrant further investigation.

Behaviorally, R47H-*hTREM2* exacerbated spatial learning and memory deficits in 7- to 9-month-old mice without affecting other cognitive domains, such as activity or anxiety levels. This finding is consistent with the vulnerability of hippocampal circuitry in AD patients. Curiously, R47H-*hTREM2* exacerbated tau-mediated deficits in female mice only, accompanied by a trend toward a lower tau load. In contrast, male P301S *hTREM2*$^{R47H/+}$ mice, which showed a trend toward improved performance on the water maze, had an increased tau load. This disconnect between tau load and behavioral performance has been observed before. For example, apolipoprotein E4 (ApoE4) exacerbated brain atrophy in P301S mice without increasing tau burden[47], and DAP12/TYROBP deficiency protected against tau-induced cognitive deficits while

elevating levels of hyperphosphorylated tau[48]. Thus, insoluble tau inclusions should be used with caution as the only biomarker of disease progression in tauopathy.

The sex-specific effects of R47H-*hTREM2* on tau-mediated cognitive deficits correlated strongly with the sex-specific transcriptional changes in these mice. R47H-*hTREM2* increased the DAM signature in female tauopathy mice, including Trem2-dependent DAM transcripts. This is distinct from *mTrem2* deficiency which blocked the transition from stage 1 to stage 2 DAM[40], suggesting that R47H may not be simply a loss-of-function variant. Moreover, R47H-*hTREM2* female tauopathy mice also exhibited an increase in inflammatory transcripts, which may contribute to the deficits observed in these mice.

These sex-dependent differences may reflect differences in disease severity. Trem2 deficiency appears to exert opposing effects on plaque load at early versus late stages of amyloid pathology[27], and, male and female P301S mice of the same age differ in microgliosis level and tau load[49]. However, sex differences in our *hTREM2*$^{R47H/+}$ mice were observed even in the absence of tau pathology, suggesting that the sex-dependent effects of R47H-*hTREM2* microglia do not depend on disease severity.

An alternative explanation for the sex-specific effects of R47H-*hTREM2* may be the differences between male and female microglial transcriptomes[50-52]. For example, ApoE4 increases risk for late-onset sporadic AD to a greater extent in women[53,54], and female ApoE4 knock-in mice have spatial memory deficits not seen in males[55]. Microglia-derived ApoE is a major source of plaque-associated ApoE[56], suggesting that sex-specific differences in microglia may impact the sex-dependent effect of ApoE4 in AD pathogenesis[57]. To our knowledge, sex-specific effects of R47H on AD pathology and progression have not been reported. A thorough assessment of the possibility of sex differences induced by R47H-*hTREM2* in human patients would require much larger sample sizes due to the rarity of this mutation.

We observed a striking correlation between mouse and human DEGs identified through single-nuclei RNA-seq in the oligodendrocyte cluster, suggesting some conserved mechanisms

between mouse and human glial cells in response to R47H-hTREM2 in the presence of tauopathy. The most significantly enriched pathways in the overlap between mouse and human oligodendrocytes were mitochondrial dysfunction and oxidative phosphorylation, suggesting altered metabolism in oligodendrocytes. Trem2 has been reported to modulate microglial metabolism through mTOR signaling[7], yet its impact on oligodendrocyte metabolism has not been investigated. Interestingly mTOR signaling is also impacted in oligodendrocytes and neurons in R47H-hTREM2 mice with and without tau. These novel findings warrant further investigation, as they can shed light on R47H-hTREM2's non-cell autonomous effects that may contribute to its pathogenicity.

Of note, all of our R47H-AD patients had at least one ApoE4 allele. How R47H-TREM2 and the ApoE genotype might interact to affect microglial function is unknown; however, AD pathology occurs in R47H-carriers in the absence of the ApoE4 allele suggesting that the E4 allele is not required for R47H's association with AD[58]. Due to our modest number of samples from R47H-AD patients, further studies are needed to confirm and extend the human sequencing findings.

The significant transcriptional correlation between our R47H tauopathy mouse model and the R47H-AD human carriers shows the strong relevance of our R47H knock-in mice as a model of human R47H-AD. Our findings also illustrate the causative role of microglia in driving AD pathogenesis. Indeed, a single mutation of a microglial gene had detrimental functional consequences associated with profound transcriptional changes in multiple cell types in the brain, especially in neurons and oligodendrocytes, in both the mouse and human brain regions we sampled. While the R47H mutation is rare, understanding how R47H causes pathogenicity can shed light on how microglial toxicity contributes to AD. By unraveling disease-enhancing properties of R47H-hTREM2 in mouse and human, our study opens new avenues for developing microglia-targeted AD therapies.

3.5 Methods

Mice

CRISPR/Cas9-mediated knock-in of wild-type or R47H human TREM2 cDNA in place of m*Trem2* was done by injecting embryos with Cas9, short-guide RNA (sgRNA), and donor vectors (generated by PNA Bio). The human TREM2 cDNA sequence was flanked on each side by 1-kb homology arms for the m*Trem2*. The sequences are as follows: *Trem2* targeted region 5′CCTGCTGCTGATCACAGGTGGGA and sgRNA sequence (antisense) 5′TCCCACCTGTGATCAGCAGCAGG. Potential off-target genes were identified with CRISPR off-target prediction software (http://www.crispor.tefor.net). There were no predicted off-targets for 1- or 2-basepair mismatches. WT hTREM2 and R47H hTREM2 lines were maintained independently and backcrossed to nontransgenic C57BL/6 mice for two to three generations, then crossed to *Cx3cr1*$^{GFP/GFP}$ or P301S mice. *Cx3cr1*$^{GFP/GFP}$ (https://www.jax.org/strain/005582) were crossed with WT or R47H hTREM2 knock-in lines to obtain *Cx3cr1*$^{GFP/+}$*hTREM*$^{R47H/+}$, *Cx3cr1*$^{GFP/+}$*hTREM2*$^{WT/+}$, and *Cx3cr1*$^{GFP/+}$*mTrem2*$^{+/+}$ littermates for both lines. P301S transgenic mice (https://www.jax.org/strain/008169) were crossed with WT or R47H human TREM2 knock-in mice to generate P301S *hTREM2*$^{R47H/+}$ and littermate P301S *mTrem2*$^{+/+}$ mice, as well as P301S *hTREM2*$^{WT/+}$ and littermate P301S *mTrem2*$^{+/+}$ mice. Mice of both sexes were used, and analyses based on sex are included in the main and supplemental figures. Mice underwent behavioral testing at 7 to 9 months of age and had not been used for any other experiments. At 8 to 9 months of age, the same mice were used for pathology and RNA-seq studies. *Cx3cr1*$^{GFP/+}$ mice were studied at 12 to 17 months of age. For electrophysiology studies, mice were 6.5 to 9 months old. All mouse protocols were approved by the Institutional Animal Care and Use Committee, University of California, San Francisco.

Human Postmortem Samples

Tissues from the superior frontal gyrus and temporal cortices from brains of donors with AD and the R47H mutation, donors with AD but without the R47H mutation, and non-AD controls (n = 3 donors per group, 2 samples per donor, one from each cortical region) were used for single-nuclear RNA-sequencing, for a total of 18 samples. Additional information about the donors can be found in Supplemental Table 10. Samples were from the Queen Square Brain Bank for Neurological Disorders at the University of College London Institute for Neurology (courtesy of Professor John Hardy and laboratory manager Linda Parsons). The NHS Health Research Authority, London-Central Research Ethics Committee approved the study and confirmed that informed consent was obtained from all subjects, REC Ref: 19/LO/0721, IRAS project ID: 246790.

In Vivo Imaging

For intravital imaging with two-photon microscopy, thinned-skull windows were made in 12–17-month-old *Cx3cr1*$^{GFP/+}$ *hTREM*$^{R47H/+}$, *Cx3cr1*$^{GFP/+}$ *hTREM2*$^{WT/+}$, and *Cx3cr1*$^{GFP/+}$ *mTrem2*$^{+/+}$ as described previously [29]. Briefly, mice were anesthetized, the skull was exposed, and a small area over the cortex was thinned manually and with a high-speed drill (K.1070 High Speed Rotary Micromotor drill; Foredom). Mice were fixed onto a custom-made head plate and imaged with an Ultima IV multiphoton microscope (Bruker) equipped with MaiTai DeepSee-eHP lasers (Spectra Physics) tuned to 920 nm for imaging and InSight X3 lasers (Spectra Physics) tuned to 880 nm for ablation. Z-stacks of images were acquired every 3 min in 1-µm steps with a 25x water-immersion objective at 2.4 optical zoom. Extensions and retractions of processes during baseline recordings were manually traced with the mTrackJ plugin. The movement of microglial cells toward a laser ablation site was analyzed by normalizing the number of processes near the injury site at each time point to the overall microglial density at that time point.

Acute Slice Preparation

Mice were anesthetized with isoflurane and decapitated. The brains were removed, placed in ice-cold dissection solution containing (in mM): 210 sucrose, 2.5 KCl, 1.25 NaH_2PO_4, 25 $NaHCO_3$, 7 glucose, 2 $MgSO_4$, and 0.5 $CaCl_2$ (gassed with 95% O_2/5% CO_2, pH ~7.4), and cut horizontally with a vibratome into 400-μm-thick slices in ice-cold dissection solution. The slices were warmed to 35°C for 1 hr in artificial cerebral spinal (ACSF) containing (in mM): 119 NaCl, 2.5 KCl, 26.2 $NaHCO_3$, 1 NaH_2PO_4, 11 glucose, 1.3 $MgSO_4$, and 2.5 $CaCl_2$ (gassed with 95% O_2/5% CO_2, pH ~7.4. Slices were then kept at room temperature in oxygenated ACSF until recordings were made.

Electrophysiology

The brain was quickly removed from mice that were anesthetized with isoflurane before decapitation. It was placed in ice-cold dissection solution containing (in mM): 210 sucrose, 2.5 KCl, 1.25 NaH2PO4, 25 NaHCO3, 7 glucose, 2 MgSO4, and 0.5 CaCl2 (gassed with 95% O2-5% CO_2, pH ~7.4). Horizontal brain slices (400 μm) were made on a vibratome in ice-cold dissection solution. Slices recovered for 1 hour in artificial cerebral spinal (ACSF) warmed to 35°C containing (in mM): 119 NaCl, 2.5 KCl, 26.2 NaHCO3, 1 NaH2PO4, 11 glucose, 1.3 MgSO4, and 2.5 CaCl2 (gassed with 95% O2-5% CO2, pH ~7.4). Then they were kept at room temperature in oxygenated ACSF. For recordings, slices were continuously perfused in ACSF at 30°C. Perforant pathway inputs to the dentate gyrus were stimulated with a bipolar tungsten electrode (FHC, Bowdoin, ME). An ACSF-filled recording electrode (~3 MΩ pipette resistance) was placed ~50 μm into the molecular layer of the dorsal dentate gyrus. A Model 2100 Isolated Pulse Stimulator (A-M Systems) was used to generate stimuli every 30 s and responses to 10–50 μA stimulus intensities were recorded with a 0.05-ms stimulus duration. LTP recordings were performed with picrotoxin (100 μM, Abcam), and the baseline stimulus intensity was set at 30% of the maximal fEPSP slope. Theta burst stimulation (TBS) was used to induce LTP, and the

stimulus intensity was set at 60% of the maximal fEPSP slope during TBS. Ten theta bursts were delivered every 15 sec, each consisting of 10 bursts of 4 100-Hz pulses every 200 ms.

Behavioral Tests

In all behavioral tests, hTREM2$^{WT/+}$ and *hTREM2*$^{R47H/+}$ mice were compared to their respective nontransgenic or P301S littermates. Experimenters were blinded to mouse genotypes throughout the experiments. Male and female mice were tested on separated days.

Morris Water Maze. The water maze consists of a pool (122 cm in diameter) containing opaque water (20 ± 1°C) and a platform (10 cm in diameter) 1.5 cm below the surface. Three different images were posted on the walls of the room as spatial cues. Hidden platform training (days 1–7) consisted of 14 sessions (two per day, 2 hrs apart), each with two trials. The mouse was placed into the pool at alternating quadrants for each trial. A trial ended when the mouse located the platform or after 60 sec had elapsed. At 24 and 72 hrs after training, the mice were tested in probe trials, in which the hidden platform was removed and mice were allowed to swim for 60 sec. Mice received 7 days of hidden platform training before the 24-hr and 72-hr probe trials. Visible platform testing was done 24 hrs after the last probe trial. Performance was measured with an EthoVision video tracking system (Noldus Information Technology).

Elevated Plus Maze. The maze consists of two 15 x 2-inch open arms without walls and two closed arms with walls 6.5 inches tall and is 30.5 inches above the ground. Mice were moved to the testing room 1 hr before testing to acclimate to the dim lighting. Mice were individually placed in the maze at the intersection of the open and closed arms and allowed to explore the maze for 10 min.

Open Field. Mice were individually placed into brightly lit automated activity chambers equipped with rows of infrared photocells connected to a computer (San Diego Instruments).

Open field activity was recorded for 5 min. Recorded beam breaks were used to calculate total time of activity.

Immunohistochemistry and Image Analysis

Mice were transcardially perfused with phosphate-buffered saline (PBS). The brains were cut vertically into hemibrains. Half of each brain was flash frozen at –80°C for RNA-seq analyses; the other half was placed first in 4% paraformaldehyde for 48 hr and then in a 30% sucrose solution for 48 hr at 4°C and cut into 30-µm-thick sections with a freezing microtome (Leica). Free-floating sections (8–10 per mouse) were washed in PBS, placed in sodium citrate buffer for 30 min at 90°C for antigen retrieval, permeabilized with PBS containing 0.5% Triton X-100 for 10 min, and blocked in PBS containing 10% normal goat serum for 1 hr. Sections were then placed in PBS with 5% normal goat serum and primary antibodies overnight at 4°C. The next day, sections were washed in PBS containing 0.1% Triton X-100, incubated with Alexa-conjugated secondary antibodies in PBS with 5% normal goat serum and washed in PBS containing 0.1% Triton X-100. Images were acquired with a Keyence BZ-X700 microscope and a 10x objective. Immunoreactivity was quantified with ImageJ software (NIH). Antibodies used for staining were anti-MC1 (1:500, kind gift from Dr. Peter Davies) and anti-Iba1 (1:500, Wako). Secondary antibodies used for staining were donkey anti-mouse 488 and donkey anti-rabbit 546 (both 1:500, ThermoFisher Scientific).

For 3D reconstruction of microglia, line-scanning confocal images of hippocampal CA3 region were obtained with a confocal microscope (LSM880, Carl Zeiss Microscopy, Thornwood, NY) and a 40x objective (1-µm focal plane intervals, one field of view per mouse). Images were examined by maximum intensity Z-projection and reconstructed in 3D with Imaris software. Branching morphological was analyzed using the “Filament Tracer” function. Experimenters were blinded to mouse genotype. Data from P301S *hTREM2*$^{WT/+}$ and P301S *hTREM2*$^{R47H/+}$ mice were normalized to data from their respective sex-specific P301S littermate controls.

Western Blot

Mouse brains were homogenized in RIPA buffer containing 50 mM Tris, pH 7.5, 150 mM NaCl, 0.5% Nonidet P-40, 1 mM EDTA (ThermoFisher Scientific), 1 mM phenylmethyl sulfonyl fluoride, protease inhibitor cocktail (Millipore Sigma) and phosphatase inhibitor cocktail (Millipore Sigma). After sonication, brain lysates were centrifuged at 18,000 *g* at 4°C for 30 min. Supernatants were collected and protein concentrations were measured with the Pierce BCA Protein Assay Kit (ThermoFisher Scientific). The same amount of protein was loaded onto a 4–12% SDS-PAGE gel (Invitrogen), transferred to nitrocellulose membranes (GE Healthcare), blocked with 5% milk, and immunoblotted in 2% milk. Bands in immunoblots were visualized by enhanced chemiluminescence (ThermoFisher Scientific) and quantified by densitometry with ImageJ (NIH). The antibody used for western blot was anti-TREM2 (1:500, Cell Signaling). Immunoreactivity was detected with goat anti-rabbit HRP (1:2000, Millipore Sigma).

Isolation of Adult Microglia

Adult microglia were isolated from 3- to 4-month-old *mTrem2*$^{+/+}$, *hTREM2*$^{R47H/+}$, and *hTREM2*$^{R47H/R47H}$ mice as described [29]. Briefly, after perfusion, brains were chopped with a razor blade, incubated with 3% collagenase type 3 (Worthington), 3 U/ml dispase (Worthington) and DNase (Millipore Sigma) at 37°C, inactivated with 2.5 mM EDTA (ThermoFisher Scientific) and 1% fetal bovine serum (FBS) (Invitrogen), filtered through a 70-μm filter, centrifuged at 300 *g* for 5 min at 18°C and resuspended in fluorescence-activated cell sorting (FACS) buffer. Samples were incubated with myelin-removal beads (Miltenyi Biotec) for 15 min at 4°C, passed through a magnetic LD column (Miltenyi Biotec), centrifuged at 300 *g* for 10 min, and resuspended in FACS buffer. Cells were magnetically separated and sorted with CD11b beads (Miltenyi Biotec) and a magnetic MS column (Miltenyi Biotec). CD11b-positive cells were centrifuged at 300 *g* for 10 min, and RNA was extracted for RNA-seq.

Isolation of Primary Microglia and *in vitro* Tau Fibril Stimulation Assay

Cortices were harvested from postnatal day 3 pups. The meninges were removed, and the cortical tissue was finely chopped with a razor blade and digested in 0.25% trypsin with DNAse (Millipore Sigma) at 37°C for 25 min. Digestion was stopped with DMEM containing 10% FBS. The tissue was then triturated and, spun at 200 *g* for 5 min, and the pellet was resuspended in DMEM and 10% FBS and plated in T75 flasks that had been pre-coated with poly-D-lysine (Millipore Sigma) and rinsed with water. Mixed cultures were maintained in flasks for 10–11 days. The flasks were then shaken for 2 hr, spun at 200 *g* for 15 min, and the cells were plated at a density of 150,000/well. After 24 hr, cells were treated or not with 1ug of 0N4R tau fibril per well (from Dr. Jason Gestwicki) for approximately 16 hr before lysis for RNA isolation.

RNA-Sequencing and Analysis of Bulk Hippocampal Tissue

Hippocampal RNA was isolated with the Qiagen RNeasy Mini Ki. After quality control analysis with a Bioanalyzer, the RNA was sent to Novogene for library preparation and PE150 sequencing with an Illumina HiSeq 4000 instrument. 48 samples were sent in for sequencing: 6 samples each from male and female P301S WT and R47H hTREM2 knock-in mice and P301S *mTrem2*$^{+/-}$ mice, and 3 samples each for male and female P301S *mTrem2*$^{+/+}$ littermates of the *hTREM2*$^{WT/+}$ line and male and female P301S *mTrem2*$^{+/+}$ littermates of the *hTREM2*$^{R47H/+}$ line.

Quality Control. We used multiple clustering methods to examine the quality of replicates and to identify possible outlier samples for exclusion if necessary. For the hTREM2 R47H line (LG72), three samples were excluded from further analysis based on clustering. Clustering techniques were applied to variance stabilizing transformed expression values, fragments per kilobase of transcript per million mapped reads, and values of log counts per million. The Pearson correlation coefficient was first used as a distance metric between samples. Hierarchical cluster analysis was then applied to measure similarity between the

Pearson correlations. The hierarchical clustering algorithm was an iterative process. Each iteration joined the two most similar clusters (based on Pearson correlation) and computed the distance between remaining clusters, continuing until there is just a single cluster. The distances between clusters were computed at each stage using the complete linkage clustering method (see manual for R hclust function).

Differential Expression Analysis. Differential gene expression was calculated with the R package DESeq2[59]. Counts were normalized with the trimmed mean normalization method[60]. Genes with <15 counts across all samples were excluded from analysis. The false discovery rate (FDR) was calculated with the Benjamini-Hochberg method[61]. Gene network analyses of RNA-seq data were done with gene set enrichment analysis (GSEA)[62]; cell types were defined by the top 100 genes expressed by each CNS cell type [63]. Pathway analysis was done with Gene Ontology (GO) biological processes[64,65] and the Kyoto Encyclopedia of Genes and Genomes (KEGG)[66]. Networks were visualized with Cytoscape (version 3.6.1)[67], the STRING database[68], and perfuse force directed layout.

Weighted Gene Co-expression Network Analysis. Weighted gene co-expression network analysis (WGCNA) was done on normalized expression data with the R package WGCNA v1.51[69]. The top 5000 most variable genes were used to create modules, and the soft-thresholding power parameter was set to 14. The minimum module size was 30 genes, and modules with a module eigengene dissimilarity below 0.2 were merged, creating 14 modules of 43–1361 genes each after removal of the module (gray) that contain genes that do not belong to any other module. KEGG and GO biological processes were used for pathway analysis as described above.

RNA-Seq and Analysis of Adult Microglia

RNA from adult microglia was extracted from *mTrem2*$^{+/+}$ (n = 7), *hTREM2*$^{R47H/+}$ (n = 6),

and *hTREM2*$^{R47H/R47H}$ (n = 7) mice with the Qiagen RNeasy Mini Kit. RNA concentration was determined with a NanoDrop, and RNA quality was measured with a Bioanalyzer and the Agilent RNA Pico Chip. Samples with an RNA integrity number >7 were considered of good quality and used for subsequent steps. Libraries were then prepared with the QuantSeq 3´ mRNA-Seq Library Prep Kit FWD for Illumina. Library quality was assessed with a Bioanalyzer and the Agilent High Sensitive DNA Chip. Individual library concentrations were measured with the Qubit dsDNA HS Assay Kit and submitted for SE50 sequencing on an Illumina HiSeq 4000. Quality control was done on base qualities and nucleotide composition of sequences. Alignment to the GRCm38.84 *Mus musculus* (mm10) refSeq (refFlat) reference gene annotation was done with the STAR spliced read aligner and default parameters. Differential gene expression analysis was done with the R package DESeq2. Counts were normalized with the trimmed mean normalization method. Genes with <15 counts across all samples were excluded from analysis. The FDR was calculated with the Benjamini-Hochberg method. Pathway analysis was done using Gene Set Enrichment Analysis referencing Gene Ontology Biological Processes dataset. Predicted upstream activators and inhibitors of the transcriptome were determined using Ingenuity Pathway Analysis software (Qiagen).

Quantitative Reverse-Transcription PCR

Flash-frozen cortices were thawed and homogenized with a 21G needle in RLT buffer with 1% β-mercaptoethanol. RNA was isolated with the RNeasy Mini-Kit (Qiagen), and the remaining DNA was removed by incubation with RNase-free DNase. Purified mRNA was then converted to cDNA with the iScript cDNA Synthesis Kit (Bio Rad). Quantitative RT-PCR was performed on the ABI 7900 HT sequence detector (Applied Biosystems) with PowerUp SYBR Green master mix (ThermoFisher Scientific). The average value of three replicates for each sample was expressed as a threshold cycle (C_t), the point at which the fluorescence signal starts to increase rapidly. Then, the difference (ΔC_t) between C_t values for the transcript of

interest and for mouse GAPDH was calculated for each sample. The relative gene expression for each sample was calculated as $2^{-\Delta Ct}$. The following primers were used:

Primer: Human TREM2 Fwd: CCGGCTGCTCATCTTACTCT

Primer: Human TREM2 Rev: GGAGTCATAGGGGCAAGACA

Primer: Mouse GAPDH Fwd: TGGCCTTCCGTGTTCCTAC

Primer: Mouse GAPDH Rev: GAGTTGCTGTTGAAGTCGCA

Isolation of Nuclei from Frozen Postmortem Human Brain Tissue

The protocol for isolating nuclei from frozen postmortem brain tissue was adapted from a previous study[35]. All procedures were done on ice or at 4°C. In brief, postmortem brain tissue was placed in 700 µl of homogenization buffer consisting of 320 mM sucrose, 5 mM $CaCl_2$, 3 mM $Mg(CH_3COO)_2$, 10 mM Tris HCl, pH 7.8, 0.1 mM EDTA pH 8.0, 0.1% IGEPAL CA-630, 1 mM ß-mercaptoethanol, and 0.4 U μl^{-1} recombinant RNase inhibitor (Clontech) and homogenized with a Wheaton Dounce tissue grinder (15 strokes with the loose pestle). The homogenized tissue was filtered through a 40-µm cell strainer, mixed with an equal volume of working solution (83% OptiPrep density gradient medium [Sigma-Aldrich], 5 mM $CaCl_2$, 3 mM $Mg(CH_3COO)_2$, 10 mM Tris HCl, pH 7.8, 0.1 mM EDTA pH 8.0, and 1 mM b-mercaptoethanol) and loaded on top of a two-layer OptiPrep density gradient: 750 ul of 30% OptiPrep solution (30% OptiPrep density gradient medium, 134 mM sucrose, 5 mM $CaCl_2$, 3 mM $Mg(CH_3COO)_2$, 10 mM Tris HCl, pH 7.8, 0.1 mM EDTA, pH 8.0, 1 mM ß-mercaptoethanol, 0.04% IGEPAL CA-630, and 0.17 U μl^{-1} recombinant RNase inhibitor), which was on top of 300 ul of 40% OptiPrep solution (40% OptiPrep density gradient medium, 96 mM sucrose, 5 mM $CaCl_2$, 3 mM $Mg(CH_3COO)_2$, 10 mM Tris HCl, pH 7.8, 0.1 mM EDTA, pH 8.0, 1 mM ß-mercaptoethanol, 0.03% IGEPAL CA-630, and 0.12 U μl^{-1} recombinant RNase inhibitor). The nuclei were separated by centrifugation at 10,000 *g* for 5 min at 4°C. A total of 100 ul of nuclei was collected from the 30%/40% interface and washed with 1 ml of PBS containing 0.04% BSA. The nuclei

were centrifuged at 300 *g* for 3 min at 4°C and washed with 1 ml of PBS containing 0.04% BSA. Then the nuclei were centrifuged at 300 *g* for 3 min at 4°C and re-suspended in 100 µl of PBS containing 0.04% BSA. The nuclei were counted and diluted to a concentration of 1000 nuclei per microliter in PBS containing 0.04% BSA.

Droplet-based Single-nuclei RNA-seq of Human Brain Tissue

For droplet-based snRNA-seq, libraries were prepared with Chromium Single Cell 3' Reagent Kits v3 (10x Genomics) according to the manufacturer's protocol. The snRNA-seq libraries were sequenced with NextSeq 500/550 High Output v2.5 kits (150 cycles).

Analysis of Droplet-Based Single-nuclei RNA-seq Data from Human Brain Tissue

Gene counts were obtained by aligning reads to the hg38 genome with Cell Ranger software (v.3.0.0) (10x Genomics). To account for unspliced nuclear transcripts, reads mapping to pre-mRNA were counted. After quantification of pre-mRNA with the Cell Ranger count pipeline, the Cell Ranger aggr pipeline was used to aggregate all libraries (without equalizing the read depth between groups) to generate a gene-count matrix. Cell Ranger 3.0 default parameters were used to call cell barcodes. To remove doublets and poor-quality cells, cells were excluded from analysis if they were extreme outliers (observations outside the range [Q1 – k(Q3 – Q1),Q3 + k(Q3-Q1)], with k = 3 and Q1 and Q3 as the lower and upper quartiles) in terms of the number of genes, the number of unique molecular identifiers (UMIs), and the percentage of mitochondrial genes. Specifically, cells with unique molecular identifier (UMI) counts above 5400 were removed, cells with less than 300 and more than 3200 genes were removed, and cells with more than 5% mitochondrial genes were removed.

Cell Clustering, Differential Expression Analysis, and Gene Set Enrichment Analysis of Human Brain Tissue

Normalization and clustering were done with the Seurat package[70]. In brief, counts for all nuclei were scaled by the total library size multiplied by a scale factor (10,000), and transformed to log space. A set of 2000 highly variable genes were identified with *SCTransform* from *sctransform* R package in the variable stabilization mode. This returned a corrected unique molecular identifiers (UMI) count matrix, a log-transformed data matrix, and Pearson residuals from the regularized negative binomial regression model. Principal component analysis (PCA) was done on all genes, and *t*-SNE was run on the top 23 PCs. Cell clusters were identified with the Seurat functions FindNeighbors (using the top 23 PCs) and FindClusters (resolution = 0.02). For each cluster, we assigned a cell-type label using statistical enrichment for sets of marker genes[42,43] and manual evaluation of gene expression for small sets of known marker genes. Enrichment was statistically assessed with the hypergeometric distribution (Fisher's exact test) using the R package GeneOverlap and multiple hypothesis correction over all marker gene sets and clusters. The differential gene expression analysis was done with the Wilcoxon rank-sum test and FDR multiple-testing corrections as implemented in the Seurat function FindMarkers. Gene set enrichment analysis to assess the overlap of human and mouse DEGs were done with the hypergeometric distribution (Fisher's exact test) as implemented in the R package GeneOverlap and with multiple hypothesis correction over all gene sets.

Isolation of Nuclei from Frozen Mouse Tissue for Single-nuclei RNA-seq

All steps were done on water-ice. The brain samples were chopped into pea-size pieces and transferred to a Dounce homogenizer (Sigma cat no. D8938) containing 2 ml of nuclei pure lysis buffer (Millipore Sigma, cat no. L9286). They were then homogenized by 20–25 strokes of a large clearance pestle and then with 20 strokes of a small clearance pestle. The resulting suspension was first filtered through the 70-μm mesh cap of a 5-ml Falcon tube (Corning) and

then through 35 µm mesh Cell Strainer Snap Cap, and collected to a 2.0-ml Eppendorf LoProtein binding tube. To confirm the quality of dissociated nuclei, 10 µl of the nuclei suspension was mixed with 10 µl of 0.5% (w/v) Trypan Blue and 1 µl of 20x DAPI dye and examined under bright-field and fluorescence microscope.

The remaining suspension was centrifuged at 600 *g* for 5 min at 4ºC in a swinging bucket centrifuge. The pellet was re-suspended in 1 ml of freshly prepared ice-cold nuclei wash buffer (1x PBS, 20 mM DTT, 1% (w/v) BSA, 0.2 U/µl RNAse Inhibitor (Ambion), DEPC-treated water), and passed through 35-µm mesh cap. To confirm the quality and number of single nuclei, 10 µl of the nuclei suspension was mixed with 10 µl of 0.5% (w/v) Trypan Blue dye and examined with a bright-field microscope. The suspension was considered high quality if it had isolated single DAPI+ nuclei with uniform round morphology. We excluded suspensions with nuclei that appeared to be clumped together or if the suspension had over 10% of nuclei with a breaking, elongated shape. The yield was ~10^6 single nuclei per 1 ml. Next, 50 µl of the nuclei suspension was diluted with 250 µl of nuclei wash buffer to be used as a negative reference for FACS. The remaining 900-950 µl of the suspension was stained with 10 µl of 100x DAPI dye and sorted on Aria III FACS instrument. Individual DAPI-positive nuclei were FACS sorted into collection tubes containing 1 ml of nuclei wash buffer. After FACS, nuclei were concentrated by centrifugation at 600 *g* for 5 min. The pellet was gently resuspended in ice-cold 1x PBS + 0.04% (w/v) BSA to achieve 2000 nuclei/µl. Finally, the single nuclei suspension was encapsulated and barcoded using 10x Genomics Chromium instrument.

Droplet-based Single-nuclei RNA-seq of Mouse Brain Tissue

The FACS-sorted suspension of DAPI-stained nuclei were washed once in ice-cold 1x PBS and 0.04% (w/v) BSA and loaded to microfluidic droplets with reagents provided in the Single Cell 3′ Reagents kit v2 (10x Genomics). mRNA barcoding was done at 53°C for 45 min, followed by heat inactivation at 85°C for 5 min. The barcoded-cDNA was PCR-amplified and

prepared for sequencing according to the Single Cell 3′ Reagent kit v2 User Guide (CG00052; Rev D). Next-generation sequencing was done on an Illumina NovaSeq 4000 instrument, using paired-end reads (R1 - 26 reads; R2 - 98 reads and index - 8 reads). FASTQ files containing the transcriptome and barcoding metadata were de-multiplexed with the SEQC pipeline[71]. In total, 33,178 individual nuclei were identified after sequencing and data filtering; an average of 1082–1759 UMIs per nucleus and 845–1194 genes per nucleus being detected. Sequencing depth was 2.59-6.76 reads per UMI.

Analysis of Droplet-based Single-nuclei RNA-seq of Mouse Brain Tissue

Preprocessing. The count matrix of all samples from 8 female mice (2 wild-type, 2 *hTREM2*$^{R47H/+}$, 2 P301S, and 2 P301S *hTREM2*$^{R47H/+}$) were pooled and normalized with a regularized negative binomial regression model implemented in *sctransform* R package (Hafemeister and Satija, 2019, bioRxiv). Cells with more than 300 detected genes were retained for downstream analysis. Other QC including mitochondrial count ratio and cell cycle effects were examined as well. We used the *Seurat v.3.0*[70] R package to analyze the data. After the preprocessing step, we retrieved 31,783 single cells out of 33,178 sequenced with 17,269 detected genes. We then identified a set of 3000 highly variable genes using the *SCTransform* from *sctransform* R package with the variable stabilization mode. This process returned a corrected unique molecular identifiers (UMI) count matrix, a log-transformed data matrix and Pearson residuals from the regularized negative binomial regression model. We then used *RunPCA* for principal component (PC) analysis of the Pearson residuals of the 3000 highly variable genes retained from previous steps. PCs were visually examined, and the first 20 PCs were selected for downstream clustering and dimensionality reduction analysis based off of the observed PC “elbow” using the *PCElbowPlot* function.

Dimensionality Reduction and Clustering. We selected first 20 PCs and used the tSNE[72] dimensionality reduction algorithm *RuntSNE*. For clustering of the first 20 PCs, we used

the modularity-based shared nearest neighbor clustering algorithm in Seurat's *FindClusters* with *resolution=0.2* and other default parameters. We retrieved 11 distinct cell clusters that encompassed 8 major cell types: astrocytes, excitatory neurons, inhibitory neurons, microglia, oligodendrocytes, oligodendrocyte precursor cells (OPCs), endothelial cells, and T cells. Cluster annotation was done manually by using established marker genes: SLC17A7, CAMK2A, NRGN (excitatory neurons), GAD1, GAD2 (inhibitory neurons), PLP1, MBP, MOBP (oligodendrocytes), SCRG1, PDGFRA, OLIG1 (OPCs), VTN, MGP, IGFBP7 (endothelial cells), C1QA, TYROBP, HEXB (microglia), CLU, ALDOC, PLA2G7 (astrocytes), and CD3D, CD3G, CCL5 (T lymphocytes). The significance of differences in the proportions of P301S and P301S *hTREM2*$^{R47H/+}$ cells in each cluster was determined by chi-square test.

Differential Expression Analysis. For differential expression analysis of cells annotated as "microglia", we used the Wilcoxon rank-sum test implemented with the *"wilcox"* method in Seurat's *FindAllMarkers* function. To identify DEGs among the 6 identified microglia clusters, we used the parameters *min.pct=0.25* and *logfc.threshold=0.25,* which considered only genes that were detected in at least 25% of the cells in a given cluster and had at least 0.25-fold difference (~1.25 times) in expression level.

Preparation of Mouse Hippocampus for Single-cell RNA-seq

Brain tissue was prepared using a previously published protocol[41]. Briefly, 8-month-old female mice were anesthetized with avertin and transcardially perfused with phosphate-buffered saline (PBS). The brain without the cerebellum was harvested and collected into cold media with 15mM HEPES, 0.5% glucose in 1XHBSS without phenol red on ice. The entire procedure was done on ice. The hippocampus was extracted and chopped into pieces using a razor blade then further homogenized using a 2ml douncer containing 2ml medium A with 80uL DNase (12500 units/mL) and 5ul recombinant RNase inhibitor (Takara Bio 2313B). Homogenized tissue

was filtered through a 70um strainers to obtain a single cell suspension. Cells were washed with medium A and resuspended in 850uL MACS buffer with 1.8uL RNase inhibitor (sterile-filtered 0.5% BSA, 2mM EDTA in 1 X PBS). Cells were incubated with 100uL myelin removal beads (MACS Miltenyl Biotec) for 10 min, and loaded onto LD columns (Miltenyi Biotec). Cells were collected and washed for FACS staining.

Single Cell Sorting for Single-cell RNA-seq

Cells were blocked in 5uL mouse Fc block for 5 min on ice then incubated with primary antibodies for 10 min then washed with FACS buffer (sterile-filtered 1% FCS, 2mM EDTA, 25mM HEPES in 1XPBS). Cells were incubated with secondary antibodies for 10min then washed with FACS buffer. Cells were resuspended in 500uL FACS buffer with RNase inhibitor (Takara Bio 2313B, 1:500) and 0.5ul Propidium Iodide (ThermoFisher Scientific P3566, 1:1000) for single cell index sorting. Cell sorting/flow cytometry analysis was done on the cell sorter (BD InFlux) at the Stanford FACS Facility. The following gates were used for sorting microglia: (1) forward scatter-area (FSC-A)/side scatter-area (SSC-A) (2) Trigger Pulse Width/ FSC (3) Live-Dead negative using PI (4) $CD45^{low}CD11b^{+}$ and $CD45^{hi}CD11b^{+}$. Single cells were sorted into 96-well plates containing 4uL lysis buffer containing 4U Recombinant RNase Inhibitor (Takara Bio 2313B), 0.05% Triton X-100, 2.5mM dNTP mix (ThermoFisher Scientific R0192), 2.5uM Oligo-dT30VN (50-AAGCAGTGGTATCAACGCAGAGTACT30VN-30), and ERCC Spike-ins (ThermoFisher Scientific 4456740) diluted at $1:2.4x10^{7}$. Plates were vortexed, spun down and frozen on dry ice, and plates were stored at −80°C freezer. Antibodies used for FACS: rabbit anti-mouse Tmem119 (Abcam ab210405, ~200ug/ul, 1:400 dilution), CD45-PE-Cy7 (ThermoFisher Scientific 25-0451-82, 1:300), CD11b-BV421 (BioLegend 101236, 1:300), goat anti-rabbit Alexa 488 (ThermoFisher Scientific 11034, 1:300).

Single-cell RNA-seq library preparation

Sequencing libraries were prepared following the Smart-seq2 published protocol[73]. Briefly, plates were thawed and incubated at 72°C for 3 min in order to anneal RNAs to the Oligo-dT30VN primer. The 6uL of the reverse transcription mixture was added to each well: 95U SMARTScribe Reverse Transcriptase (100U/µl, Clontech 639538), 10U RNase inhibitor (40U/µl), 1XFirst-Strand buffer, 5mM DTT, 1M Betaine, 6mM MgCl2, 1µM TSO (Exiqon, Rnase free HPLC purified). RT was performed at 42°C for 90 min, followed by 70°C, 5 min. 15ul of PCR amplification mix containing the following reagents was added to each well: 1X KAPA HIFI Hotstart Master Mix (Kapa Biosciences KK2602), 0.1uM ISPCR Oligo (AAGCAGTGGTAT CAACGCAGAGT), 0.56U Lambda Exonuclease (5U/ul, New England BioLabs M0262S). cDNA was amplified using the following PCR program: (1) 37°C 30 min; (2) 95°C 3 min; (3) 23 cycles of 98°C 20 s, 67°C 15 s, 72°C 4 min; (4) 72°C 5 min. cDNA samples were purified using PCRClean DX beads (0.7:1 ratio, Aline C-1003-50), and resuspended in 20ul EB buffer. cDNA quality was examined with a Fragment Analyzer (AATI, High Sensitivity NGS Fragment Analysis Kit:1 bp - 6000 bp). To make libraries, all samples were diluted down to 0.15ng/ul in 384-well plates using Mantis Liquid Handler (Formulatrix) and Mosquito X1 (TTP Labtech) with customized scripts. Nextera XT DNA Sample Prep Kit (Illumina FC-131-1096) was used at 1/10 of recommendation volume, with the help of a Mosquito HTS robot for liquid transfer. Tagmentation was done in 1.6ul (1.2ul Tagment enzyme mix, 0.4ul diluted cDNA) at 55°C, 10 min. 0.4ul Neutralization buffer was added to each well and incubated at room temperature for 5 min. 0.8ul Illumina Nextera XT 384 Indexes (0.4ul each, 5uM from 4 sets of 96 indexes) and 1.2ul PCR master mix were added to amplify whole transcriptomes using the following PCR program: (1) 72°C 3 min; (2) 95°C 30 s; (3) 10 cycles of 95°C 10 s, 55°C 30 s, 72°C 1 min; (4) 72°C 5 min. Libraries from one 384 plate were pooled into an Eppendorf tube and purified twice using PCRClean DX beads. Quality and concentrations of the final libraries were measured with

Bioanalyzer and Qubit, respectively. Libraries were sequences on the Illumina HiSeq 4000 at the Weill Cornell Medicine Genomics and Epigenomics Core Facility.

Processing of Single-cell RNA-seq Raw Data

Prinseq[74] was first used to filter sequencing reads shorter than 30 bp (-min_len 30), to trim the first 10 bp at the 50 end (-trim_left 10) of the reads, to trim reads with low quality from the 30 end (-trim_qual_right 25) and to remove low complexity reads (-lc_method entropy, -lc_threshold 65). Then, Trim Galore was applied to trim the Nextera adapters (–stringency 1). The remaining reads were aligned to the mm10 genome by calling STAR (Dobin et al., 2013) with the following options: –outFilterType BySJout,–outFilterMultimapNmax 20,–alignSJoverhangMin 8,–alignSJDBoverhangMin 1,– outFilterMismatchNmax 999,–outFilterMismatchNoverLmax 0.04,–alignIntronMin 20,–alignIntronMax 1000000,–alignMatesGapMax 1000000,–outSAMstrandField intronMotif. Picard was then used to remove the duplicate reads (VALIDATION_ STRINGENCY = LENIENT, REMOVE_DUPLICATES = true). Finally, the aligned reads were converted to counts for each gene by using HTSeq (-m intersection-nonempty, -s no)[75].

Quality Control for Single-cell RNA-seq Data

We used the following criteria to filter out cells with low sequencing quality. The distribution of total reads (in logarithmic scale) was fitted by a truncated Cauchy distribution, and data points in two tails of the estimated distribution were considered as outliers and eliminated. Fitting and elimination were then applied to the remaining data. This process was run iteratively until the estimated distribution became stable. The threshold was set to the value where the cumulative distribution function of the estimated distribution reaches 0.05. Cells with small numbers of detected genes and poor correlation coefficients for ERCC (low sequencing

accuracy) were dropped. 1424 cells were retained for downstream analysis after filtering from 1480 cells.

Clustering Analysis of Single-cell RNA-seq Data

The Seurat R package was used to perform unsupervised clustering analysis on the filtered scRNA-seq data[70,76]. Gene counts were normalized to the total expression and log-transformed. Principal component analysis was performed on the scaled data using highly variable genes as input. The JackStrawPlot function was used to determine the statistically significant principal components. These principal components were used to compute the distance metric and generate cell clusters. Non-linear dimensional reduction (t-SNE) was used to visualize clustering results. Differentially expressed genes were found using the FindAllMarkers function that ran Wilcoxon rank sum tests.

Quantification and Statistical Analysis

Data were analyzed with Graphpad Prism v.7, STATA12, or R. A multilevel mixed-effects linear regression model fitted with STATA12 was used to compare the response to injury of aged mice and analyze latency in the Morris water maze. R was used to calculate the area under the curve for cumulative search errors in the Morris water maze. Outliers were removed with Prism's outlier analysis algorithm. All statistical details can be found in the figures and figure legends. $P < 0.05$ and $FRD < 0.05$ was considered statistically significant, unless otherwise noted. All values are expressed as mean ± SEM, unless otherwise noted. A subset of mice from the behavior cohort was randomly selected for single-nuclei RNA-seq and bulk RNA-seq studies.

Data Availability

All RNA sequencing data will be deposited in the Gene Expression Omnibus (GEO).

3.6 Acknowledgments

We thank Dr. Junli Zhang from the Gladstone Institutes Transgenic Core for microinjections into embryos to generate knock-in human TREM2 mice; Allan Villanueva and Elizabeth Fan for assistance with genotyping; Dr. Jason Gestwicki for providing recombinant tau fibrils; and Stephen Ordway for manuscript editing. All *in vivo* imaging was done by L.K., with helpful advice from Dr. Mario Merlini and Dr. Katerina Akassoglou, at the Gladstone Center for In Vivo Imaging Research. All immunohistochemistry imaging was done by F.A.S. and L.K. using the Gladstone Histology Core microscopes. Behavioral assays were done by F.A.S. and D.L. using equipment from the Gladstone Behavioral Core. RNA-sequencing was done by the UCSF Center for Advanced Technology (bulk-seq) and Sloan-Kettering Cancer Center (SKCC) Genomics core (single-nuclei RNA-seq). This work was supported by the National Institute of Health Grants R01AG051390, U54NS100717, R01AG054214, and Rainwater Foundation (to L.G), the National Institute of Aging Grant F31 AG058505 (to F.A.S.), the National Institute of Aging Grant F30 AG062043-01 (to L.K.), the Cure Alzheimer's Fund, JBP Foundation, and NIH grants RF1AG054321, RF1AG062377, RF1AG054012, U01NS110453, R01AG062335, and R01AG058002 (to L.H.T), the Early Postdoctoral Mobility Fellowship from the Swiss National Science Foundation P2BSP3 151885 (to H.M.), and the Alan and Sandra Gerry Foundation (to L.M.). Authors are grateful to the Flow Cytometry Core and the Integrated Genomics Operation at MSKCC for their assistance.

3.7 References

1 Guerreiro, R. *et al.* TREM2 variants in Alzheimer's disease. *N Engl J Med* **368**, 117-127, doi:10.1056/NEJMoa1211851 (2013).

2 Jonsson, T. & Stefansson, K. TREM2 and neurodegenerative disease. *N Engl J Med* **369**, 1568-1569, doi:10.1056/NEJMc1306509 (2013).

3 Kunkle, B. W. *et al.* Genetic meta-analysis of diagnosed Alzheimer's disease identifies new risk loci and implicates Abeta, tau, immunity and lipid processing. *Nat Genet* **51**, 414-430, doi:10.1038/s41588-019-0358-2 (2019).

4 Sims, R. *et al.* Rare coding variants in PLCG2, ABI3, and TREM2 implicate microglial-mediated innate immunity in Alzheimer's disease. *Nat Genet* **49**, 1373-1384, doi:10.1038/ng.3916 (2017).

5 Butovsky, O. *et al.* Identification of a unique TGF-beta-dependent molecular and functional signature in microglia. *Nat Neurosci* **17**, 131-143, doi:10.1038/nn.3599 (2014).

6 Hickman, S. E. *et al.* The microglial sensome revealed by direct RNA sequencing. *Nat Neurosci* **16**, 1896-1905, doi:nn.3554 [pii]10.1038/nn.3554 (2013).

7 Ulland, T. K. *et al.* TREM2 maintains microglial metabolic fitness in Alzheimer's Disease. *Cell* **170**, 649-663 e613, doi:10.1016/j.cell.2017.07.023 (2017).

8 Poliani, P. L. *et al.* TREM2 sustains microglial expansion during aging and response to demyelination. *J Clin Invest* **125**, 2161-2170, doi:10.1172/JCI77983 (2015).

9 Wang, Y. *et al.* TREM2 lipid sensing sustains the microglial response in an Alzheimer's disease model. *Cell* **160**, 1061-1071, doi:10.1016/j.cell.2015.01.049 (2015).

10 Takahashi, K., Rochford, C. D. & Neumann, H. Clearance of apoptotic neurons without inflammation by microglial triggering receptor expressed on myeloid cells-2. *J Exp Med* **201**, 647-657, doi:10.1084/jem.20041611 (2005).

11 Bouchon, A., Hernandez-Munain, C., Cella, M. & Colonna, M. A DAP12-mediated pathway regulates expression of CC chemokine receptor 7 and maturation of human dendritic cells. *J Exp Med* **194**, 1111-1122, doi:10.1084/jem.194.8.1111 (2001).

12 Cheng, Q. *et al.* TREM2-activating antibodies abrogate the negative pleiotropic effects of the Alzheimer's disease variant Trem2(R47H) on murine myeloid cell function. *J Biol Chem* **293**, 12620-12633, doi:10.1074/jbc.RA118.001848 (2018).

13 Zheng, H. *et al.* TREM2 promotes microglial survival by activating wnt/beta-catenin pathway. *J Neurosci* **37**, 1772-1784, doi:10.1523/JNEUROSCI.2459-16.2017 (2017).

14 Hsieh, C. L. *et al.* A role for TREM2 ligands in the phagocytosis of apoptotic neuronal cells by microglia. *J Neurochem* **109**, 1144-1156, doi:10.1111/j.1471-4159.2009.06042.x (2009).

15 Daws, M. R. *et al.* Pattern recognition by TREM-2: binding of anionic ligands. *J Immunol* **171**, 594-599, doi:10.4049/jimmunol.171.2.594 (2003).

16 Bailey, C. C., DeVaux, L. B. & Farzan, M. The triggering receptor expressed on myeloid cells 2 binds apolipoprotein E. *J Biol Chem* **290**, 26033-26042, doi:10.1074/jbc.M115.677286 (2015).

17 Atagi, Y. *et al.* Apolipoprotein E Is a ligand for triggering receptor expressed on myeloid cells 2 (TREM2). *J Biol Chem* **290**, 26043-26050, doi:10.1074/jbc.M115.679043 (2015).

18 Yeh, F. L., Wang, Y., Tom, I., Gonzalez, L. C. & Sheng, M. TREM2 binds to apolipoproteins, including APOE and CLU/APOJ, and thereby facilitates uptake of amyloid-beta by microglia. *Neuron* **91**, 328-340, doi:10.1016/j.neuron.2016.06.015 (2016).

19 Zhao, Y. *et al.* TREM2 is a receptor for beta-amyloid that mediates microglial function. *Neuron* **97**, 1023-1031 e1027, doi:10.1016/j.neuron.2018.01.031 (2018).

20 Wunderlich, P. *et al.* Sequential proteolytic processing of the triggering receptor expressed on myeloid cells-2 (TREM2) protein by ectodomain shedding and gamma-

secretase-dependent intramembranous cleavage. *J Biol Chem* **288**, 33027-33036, doi:10.1074/jbc.M113.517540 (2013).

21 Kleinberger, G. *et al.* TREM2 mutations implicated in neurodegeneration impair cell surface transport and phagocytosis. *Sci Transl Med* **6**, 243ra286, doi:10.1126/scitranslmed.3009093 (2014).

22 Feuerbach, D. *et al.* ADAM17 is the main sheddase for the generation of human triggering receptor expressed in myeloid cells (hTREM2) ectodomain and cleaves TREM2 after Histidine 157. *Neurosci Lett* **660**, 109-114, doi:10.1016/j.neulet.2017.09.034 (2017).

23 Zhong, L. *et al.* Soluble TREM2 induces inflammatory responses and enhances microglial survival. *J Exp Med* **214**, 597-607, doi:10.1084/jem.20160844 (2017).

24 Zhong, L. *et al.* DAP12 stabilizes the C-terminal fragment of the triggering receptor expressed on myeloid cells-2 (TREM2) and protects against LPS-induced pro-inflammatory response. *J Biol Chem* **290**, 15866-15877, doi:10.1074/jbc.M115.645986 (2015).

25 Ulrich, J. D. *et al.* Altered microglial response to Abeta plaques in APPPS1-21 mice heterozygous for TREM2. *Mol Neurodegener* **9**, 20, doi:10.1186/1750-1326-9-20 (2014).

26 Wang, Y. *et al.* TREM2-mediated early microglial response limits diffusion and toxicity of amyloid plaques. *J Exp Med* **213**, 667-675, doi:10.1084/jem.20151948 (2016).

27 Jay, T. R. *et al.* Disease progression-dependent effects of TREM2 deficiency in a mouse model of Alzheimer's Disease. *J Neurosci* **37**, 637-647, doi:10.1523/JNEUROSCI.2110-16.2016 (2017).

28 Leyns, C. E. G. *et al.* TREM2 deficiency attenuates neuroinflammation and protects against neurodegeneration in a mouse model of tauopathy. *Proc Natl Acad Sci USA* **114**, 11524-11529, doi:10.1073/pnas.1710311114 (2017).

29 Sayed, F. A. *et al.* Differential effects of partial and complete loss of TREM2 on microglial injury response and tauopathy. *Proc Natl Acad Sci USA* **115**, 10172-10177, doi:10.1073/pnas.1811411115 (2018).

30 Song, W. M. *et al.* Humanized TREM2 mice reveal microglia-intrinsic and -extrinsic effects of R47H polymorphism. *J Exp Med* **215**, 745-760, doi:10.1084/jem.20171529 (2018).

31 Kober, D. L. *et al.* Neurodegenerative disease mutations in TREM2 reveal a functional surface and distinct loss-of-function mechanisms. *Elife* **5**, doi:10.7554/eLife.20391 (2016).

32 Paloneva, J. *et al.* Mutations in two genes encoding different subunits of a receptor signaling complex result in an identical disease phenotype. *Am J Hum Genet* **71**, 656-662, doi:10.1086/342259 (2002).

33 Slattery, C. F. *et al.* R47H TREM2 variant increases risk of typical early-onset Alzheimer's disease but not of prion or frontotemporal dementia. *Alzheimers Dement* **10**, 602-608 e604, doi:10.1016/j.jalz.2014.05.1751 (2014).

34 Rosenberg, A. B. *et al.* Single-cell profiling of the developing mouse brain and spinal cord with split-pool barcoding. *Science* **360**, 176-182, doi:10.1126/science.aam8999 (2018).

35 Mathys, H. *et al.* Single-cell transcriptomic analysis of Alzheimer's disease. *Nature*, doi:10.1038/s41586-019-1195-2 (2019).

36 Gomez-Isla, T. *et al.* Neuronal loss correlates with but exceeds neurofibrillary tangles in Alzheimer's disease. *Ann Neurol* **41**, 17-24, doi:10.1002/ana.410410106 (1997).

37 Giannakopoulos, P. *et al.* Tangle and neuron numbers, but not amyloid load, predict cognitive status in Alzheimer's disease. *Neurology* **60**, 1495-1500, doi:10.1212/01.wnl.0000063311.58879.01 (2003).

38 Yoshiyama, Y. *et al.* Synapse loss and microglial activation precede tangles in a P301S tauopathy mouse model. *Neuron* **53**, 337-351, doi:10.1016/j.neuron.2007.01.010 (2007).

39 Weaver, C. L., Espinoza, M., Kress, Y. & Davies, P. Conformational change as one of the earliest alterations of tau in Alzheimer's disease. *Neurobiol Aging* **21**, 719-727 (2000).

40 Keren-Shaul, H. *et al.* A unique microglia type associated with restricting development of Alzheimer's Disease. *Cell* **169**, 1276-1290 e1217, doi:10.1016/j.cell.2017.05.018 (2017).

41 Li, Q. *et al.* Developmental Heterogeneity of Microglia and Brain Myeloid Cells Revealed by Deep Single-Cell RNA Sequencing. *Neuron* **101**, 207-223 e210, doi:10.1016/j.neuron.2018.12.006 (2019).

42 Lake, B. B. *et al.* Integrative single-cell analysis of transcriptional and epigenetic states in the human adult brain. *Nat Biotechnol* **36**, 70-80, doi:10.1038/nbt.4038 (2018).

43 Wang, D. *et al.* Comprehensive functional genomic resource and integrative model for the human brain. *Science* **362**, doi:10.1126/science.aat8464 (2018).

44 Cheng-Hathaway, P. J. *et al.* The Trem2 R47H variant confers loss-of-function-like phenotypes in Alzheimer's disease. *Mol Neurodegener* **13**, 29, doi:10.1186/s13024-018-0262-8 (2018).

45 Xiang, X. *et al.* The Trem2 R47H Alzheimer's risk variant impairs splicing and reduces Trem2 mRNA and protein in mice but not in humans. *Mol Neurodegener* **13**, 49, doi:10.1186/s13024-018-0280-6 (2018).

46 Filipello, F. *et al.* The microglial innate iImmune receptor TREM2 is required for synapse elimination and normal brain connectivity. *Immunity* **48**, 979-991 e978, doi:10.1016/j.immuni.2018.04.016 (2018).

47 Shi, Y. *et al.* ApoE4 markedly exacerbates tau-mediated neurodegeneration in a mouse model of tauopathy. *Nature* **549**, 523-527, doi:10.1038/nature24016 (2017).

48 Audrain, M. *et al.* Integrative approach to sporadic Alzheimer's disease: deficiency of TYROBP in a tauopathy mouse model reduces C1q and normalizes clinical phenotype while increasing spread and state of phosphorylation of tau. *Mol Psychiatry*, doi:10.1038/s41380-018-0258-3 (2018).

49 Yanamandra, K. *et al.* Anti-tau antibodies that block tau aggregate seeding in vitro markedly decrease pathology and improve cognition in vivo. *Neuron* **80**, 402-414, doi:10.1016/j.neuron.2013.07.046 (2013).

50 Hanamsagar, R. & Bilbo, S. D. Environment matters: microglia function and dysfunction in a changing world. *Curr Opin Neurobiol* **47**, 146-155, doi:10.1016/j.conb.2017.10.007 (2017).

51 Villa, A. *et al.* Sex-specific features of microglia from adult mice. *Cell Rep* **23**, 3501-3511, doi:10.1016/j.celrep.2018.05.048 (2018).

52 Guneykaya, D. *et al.* Transcriptional and translational differences of microglia from male and female brains. *Cell Rep* **24**, 2773-2783 e2776, doi:10.1016/j.celrep.2018.08.001 (2018).

53 Farrer, L. A. *et al.* Effects of age, sex, and ethnicity on the association between apolipoprotein E genotype and Alzheimer disease. A meta-analysis. APOE and Alzheimer Disease Meta Analysis Consortium. *JAMA* **278**, 1349-1356 (1997).

54 Altmann, A., Tian, L., Henderson, V. W., Greicius, M. D. & Alzheimer's Disease Neuroimaging Initiative Investigators. Sex modifies the APOE-related risk of developing Alzheimer disease. *Ann Neurol* **75**, 563-573, doi:10.1002/ana.24135 (2014).

55 Raber, J. *et al.* Isoform-specific effects of human apolipoprotein E on brain function revealed in ApoE knockout mice: increased susceptibility of females. *Proc Natl Acad Sci USA* **95**, 10914-10919, doi:10.1073/pnas.95.18.10914 (1998).

56 Parhizkar, S. *et al.* Loss of TREM2 function increases amyloid seeding but reduces plaque-associated ApoE. *Nat Neurosci* **22**, 191-204, doi:10.1038/s41593-018-0296-9 (2019).

57 Kodama, L. & Gan, L. Do microglial sex differences contribute to sex differences in neurodegenerative diseases? *Trends Mol Med*, doi:10.1016/j.molmed.2019.05.001 (2019).

58 Guerreiro, R. *et al.* Is APOE epsilon4 required for Alzheimer's disease to develop in TREM2 p.R47H variant carriers? *Neuropathol Appl Neurobiol* **45**, 187-189, doi:10.1111/nan.12517 (2019).

59 Love, M. I., Huber, W. & Anders, S. Moderated estimation of fold change and dispersion for RNA-seq data with DESeq2. *Genome Biol* **15**, 550, doi:10.1186/s13059-014-0550-8 (2014).

60 Robinson, M. D. & Oshlack, A. A scaling normalization method for differential expression analysis of RNA-seq data. *Genome Biol* **11**, R25, doi:10.1186/gb-2010-11-3-r25 (2010).

61 Benjamini, Y. & Hochberg, Y. Controlling the false discovery rate - a practical and powerful approach to multiple testing. *J R Stat Soc B* **57**, 289-300 (1995).

62 Subramanian, A. *et al.* Gene set enrichment analysis: a knowledge-based approach for interpreting genome-wide expression profiles. *Proc Natl Acad Sci USA* **102**, 15545-15550, doi:10.1073/pnas.0506580102 (2005).

63 Zhang, Y. *et al.* An RNA-sequencing transcriptome and splicing database of glia, neurons, and vascular cells of the cerebral cortex. *J Neurosci* **34**, 11929-11947, doi:10.1523/JNEUROSCI.1860-14.2014 (2014).

64 Ashburner, M. *et al.* Gene ontology: tool for the unification of biology. The Gene Ontology Consortium. *Nat Genet* **25**, 25-29, doi:10.1038/75556 (2000).

65 The Gene Ontology, C. Expansion of the Gene Ontology knowledgebase and resources. *Nucleic Acids Res* **45**, D331-D338, doi:10.1093/nar/gkw1108 (2017).

66 Kanehisa, M. & Goto, S. KEGG: kyoto encyclopedia of genes and genomes. *Nucleic Acids Res* **28**, 27-30, doi:10.1093/nar/28.1.27 (2000).

67 Shannon, P. *et al.* Cytoscape: a software environment for integrated models of biomolecular interaction networks. *Genome Res* **13**, 2498-2504, doi:10.1101/gr.1239303 (2003).

68 Szklarczyk, D. *et al.* The STRING database in 2017: quality-controlled protein-protein association networks, made broadly accessible. *Nucleic Acids Res* **45**, D362-D368, doi:10.1093/nar/gkw937 (2017).

69 Langfelder, P. & Horvath, S. WGCNA: an R package for weighted correlation network analysis. *BMC Bioinformatics* **9**, 559, doi:10.1186/1471-2105-9-559 (2008).

70 Butler, A., Hoffman, P., Smibert, P., Papalexi, E. & Satija, R. Integrating single-cell transcriptomic data across different conditions, technologies, and species. *Nat Biotechnol* **36**, 411-420, doi:10.1038/nbt.4096 (2018).

71 Azizi, E. *et al.* Single-cell map of diverse immune phenotypes in the breast tumor microenvironment. *Cell* **174**, 1293-1308 e1236, doi:10.1016/j.cell.2018.05.060 (2018).

72 van der Maaten, L. Visualizing data using t-SNE. *Journal of Machine Learning Research* **9**, 2579-2605 (2008).

73 Picelli, S. *et al.* Full-length RNA-seq from single cells using Smart-seq2. *Nat Protoc* **9**, 171-181, doi:10.1038/nprot.2014.006 (2014).

74 Schmieder, R. & Edwards, R. Quality control and preprocessing of metagenomic datasets. *Bioinformatics* **27**, 863-864, doi:10.1093/bioinformatics/btr026 (2011).

75 Anders, S., Pyl, P. T. & Huber, W. HTSeq--a Python framework to work with high-throughput sequencing data. *Bioinformatics* **31**, 166-169, doi:10.1093/bioinformatics/btu638 (2015).

76 Stuart, T. *et al.* Comprehensive Integration of Single-Cell Data. *Cell* **177**, 1888-1902 e1821, doi:10.1016/j.cell.2019.05.031 (2019).

3.8 Main Figures

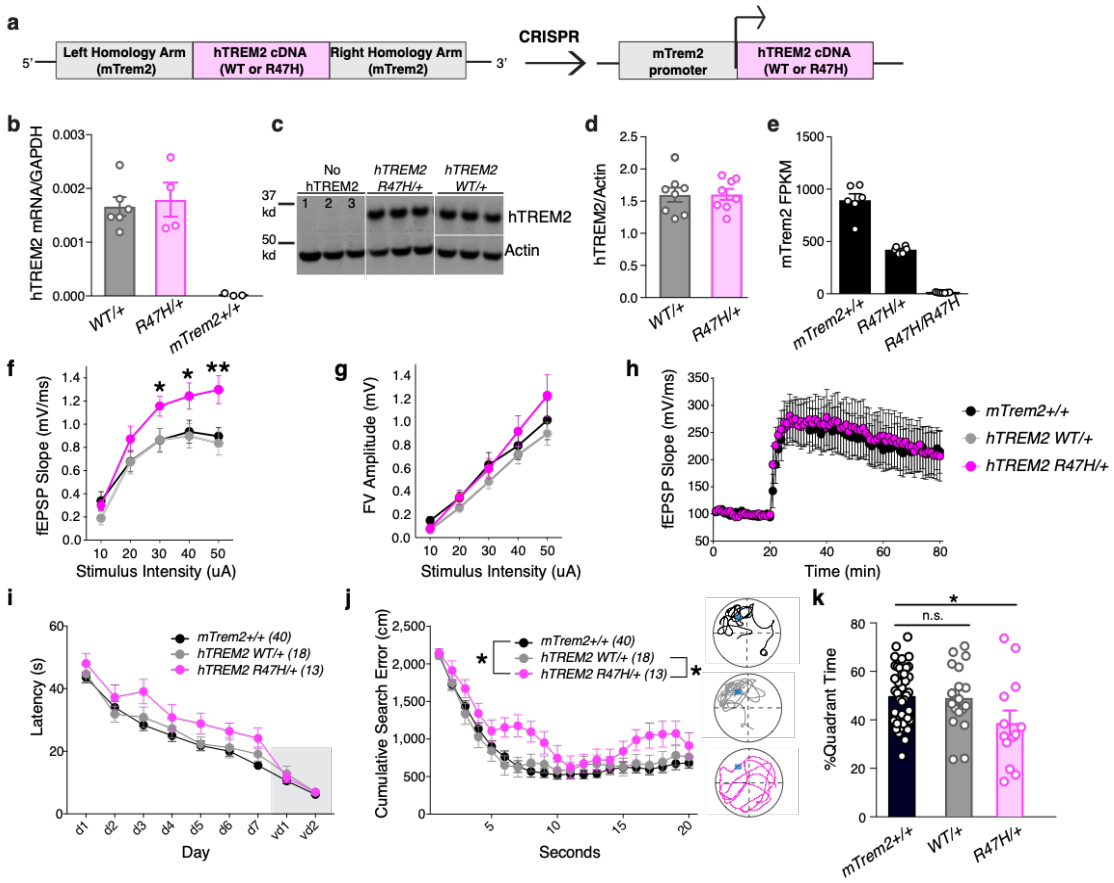

Figure 3.1 R47H-hTREM2 Induces Aberrant Synaptic Transmission and Spatial Memory Impairment.

a, The human TREM2 donor vector was designed with two 1-kilobase long arms homologous to mouse Trem2 flanking the wild-type or R47H human TREM2 cDNA sequence. When inserted into the genome, hTREM2 cDNA is driven by the endogenous mouse Trem2 promoter.

b, Quantitative real-time PCR analysis of cortical tissue from 3-4-month-old mice for human TREM2 mRNA. Samples were run in triplicate, and averages of the three wells were used for quantification, normalized to GAPDH. Puncta represent the average of three wells from one mouse. Two-tailed Mann-Whitney U-test comparing WT/+ and R47H/+.

c, RIPA-soluble cortical lysates from 8-9-month-old mice were immunoblotted for human TREM2 and actin. Lane 1=*mTrem2* KO, Lanes 2-3=$mTrem2^{+/+}$

d, Ratio of hTREM2/actin from western blot in (**c**). Student's two-tailed t-test.

e, RNA-sequencing of adult microglia isolated from 3-4-month-old mice. Mouse Trem2 (mTrem2) transcript levels decreased as human TREM2 levels increased. FPKM, fragments per kilobase of transcript per million mapped reads. Kruskal-Wallis statistic=16.01, p=1.289e-007, Kruskal-Wallis test with Dunn's post-hoc analysis.

f-h, Field recordings in the molecular layer of the dentate gyrus in response to stimulation of the perforant pathway in 6.5–9-month-old mice (n=12–13 slices from 4 mice/genotype). **f,** Mean field excitatory postsynaptic potential (fEPSP) slope calculated at increasing stimulus intensities. $hTREM2^{R47H/+}$ slices had significantly larger synaptic responses to stronger stimulus intensities compared to $mTrem2^{+/+}$ slices. F=2.529 (genotype x stimulus), p<0.013,

*t=2.299, p=0.049 (30uA), *t=2.402, p=0.038 (40uA), **t=3.136, p=0.005, two-way repeated-measures ANOVA with Bonferroni post-hoc analysis. **g,** Mean amplitude of the fiber volley (FV) was unaffected in *hTREM2*$^{R47H/+}$ slices. Two-way repeated-measures ANOVA with Bonferroni post-hoc analysis. **h**, Mean fEPSP slope during long-term potentiation (LTP) induced by theta-burst stimulation of the perforant pathway in dentate granule cells. LTP in *hTREM2*$^{R47H/+}$ mice was similar to that of *mTrem2*$^{+/+}$ mice (n = 8 slices from 3 mice/genotype). Two-way repeated-measures ANOVA with Bonferroni post-hoc analysis for data between 75-80 minutes.

i-k, Spatial learning and memory assessment of 7–9-month-old mice using the Morris water maze. **i,** Latency to reach the platform location did not differ by genotype during hidden (d1–d7) or visible platform trials (vd1–vd2). STATA mixed-effects modeling. **j,** (left) Cumulative search errors during the 24-hr probe trial were significantly greater in *hTREM2*$^{R47H/+}$ mice than in nontransgenic littermates or *hTREM2*$^{WT/+}$ mice. *Kruskal-Wallis statistic=7.671, p=0.0216, *t=2.615, p=0.02675 (mTrem2+/+ vs. hTREM2 R47H/+), *t=2.415, p=0.04723 (hTREM2 WT/+ vs. hTREM2 R47H/+), Kruskal-Wallis test with Dunn's post-hoc analysis on area under the curve. (right) Representative search tracks from one mouse of each genotype. The blue square indicates the hidden platform location in the upper left-hand quadrant. The four quadrants of the pool are delineated by dashed lines. **k,** Percentage of time spent in the target quadrants during the 24-hr probe trial. *hTREM2*$^{R47H/+}$ spent significantly less time in the target quadrant than *mTrem2*$^{+/+}$ and *hTREM2*$^{WT/+}$ mice. *F=3.462, p=0.03699, *t=2.581, p=0.02404, one-way ANOVA with Bonferroni post-hoc analysis. Data represent the combination of two behavioral cohorts that were run independently.

Values are mean ± SEM. See also Supplementary Figures 1-2.

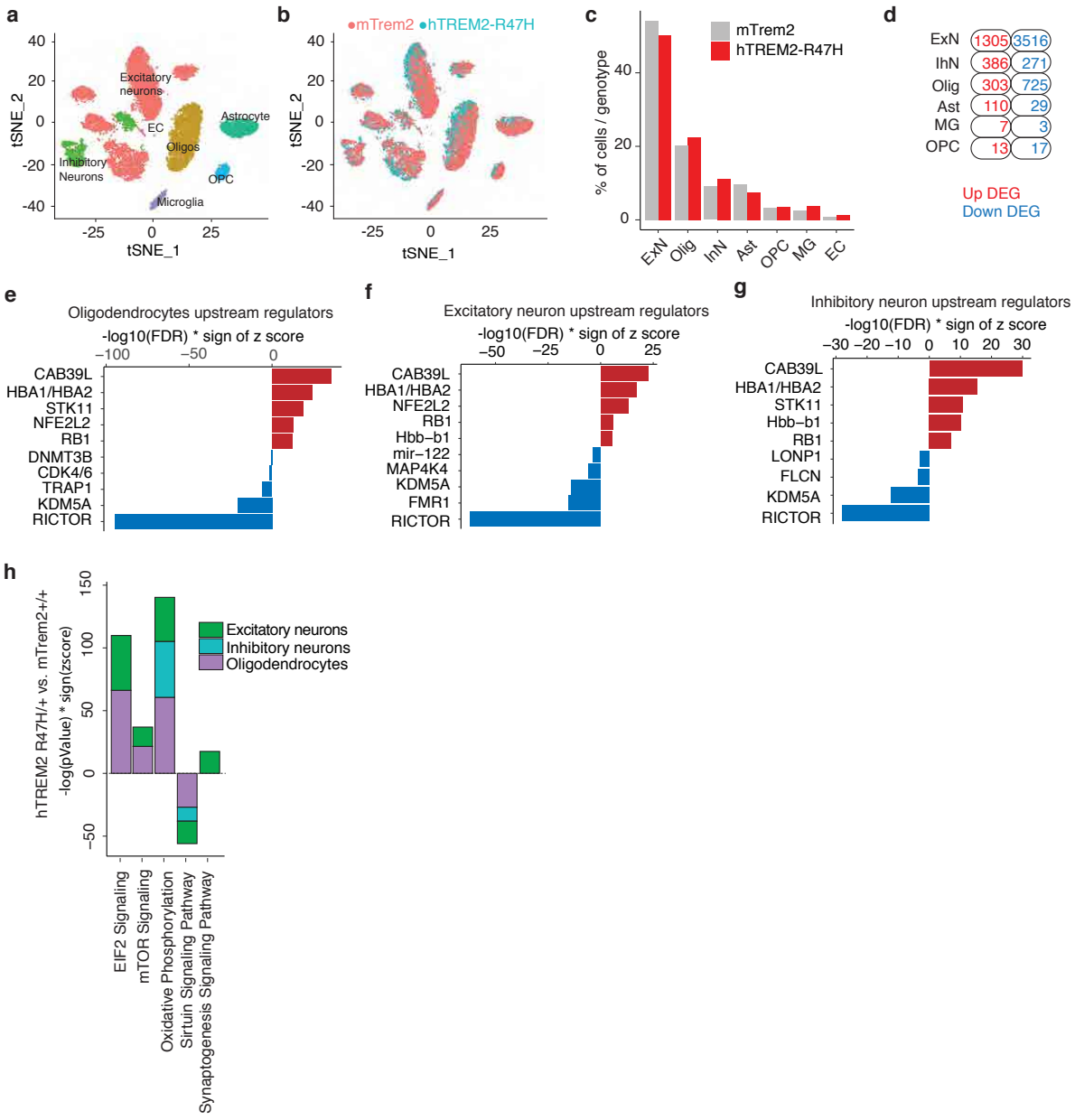

Figure 3.2 Microglial hTREM2-R47H Induces Unique Transcriptional States in Neurons and Oligodendrocytes

a, t-SNE plots of all single nuclei and their annotated cell types from 2 each of *mTrem2*$^{+/+}$ and *hTREM2*$^{R47H/+}$ 9-month-old female mice.

b, t-SNE plot split by genotype.

c, Proportion of each cell type for each genotype.

d, Total number of DEGs for each cell type for *hTREM2*$^{R47H/+}$ vs. *mTrem2*$^{+/+}$. FDR < 0.05.

e-g, Ingenuity pathway analysis's predicted upstream regulators for oligodendrocytes (**e**), excitatory neurons (**f**), and inhibitory neurons (**g**). Red and blue denote upstream regulators that are predicted to be activated or inhibited, respectively.

h, Ingenuity canonical pathway enrichment analysis of DEGs in *hTREM2*$^{R47H/+}$ vs. *mTrem2*$^{+/+}$ by specified cell type. See also Supplementary Figures 3-4.

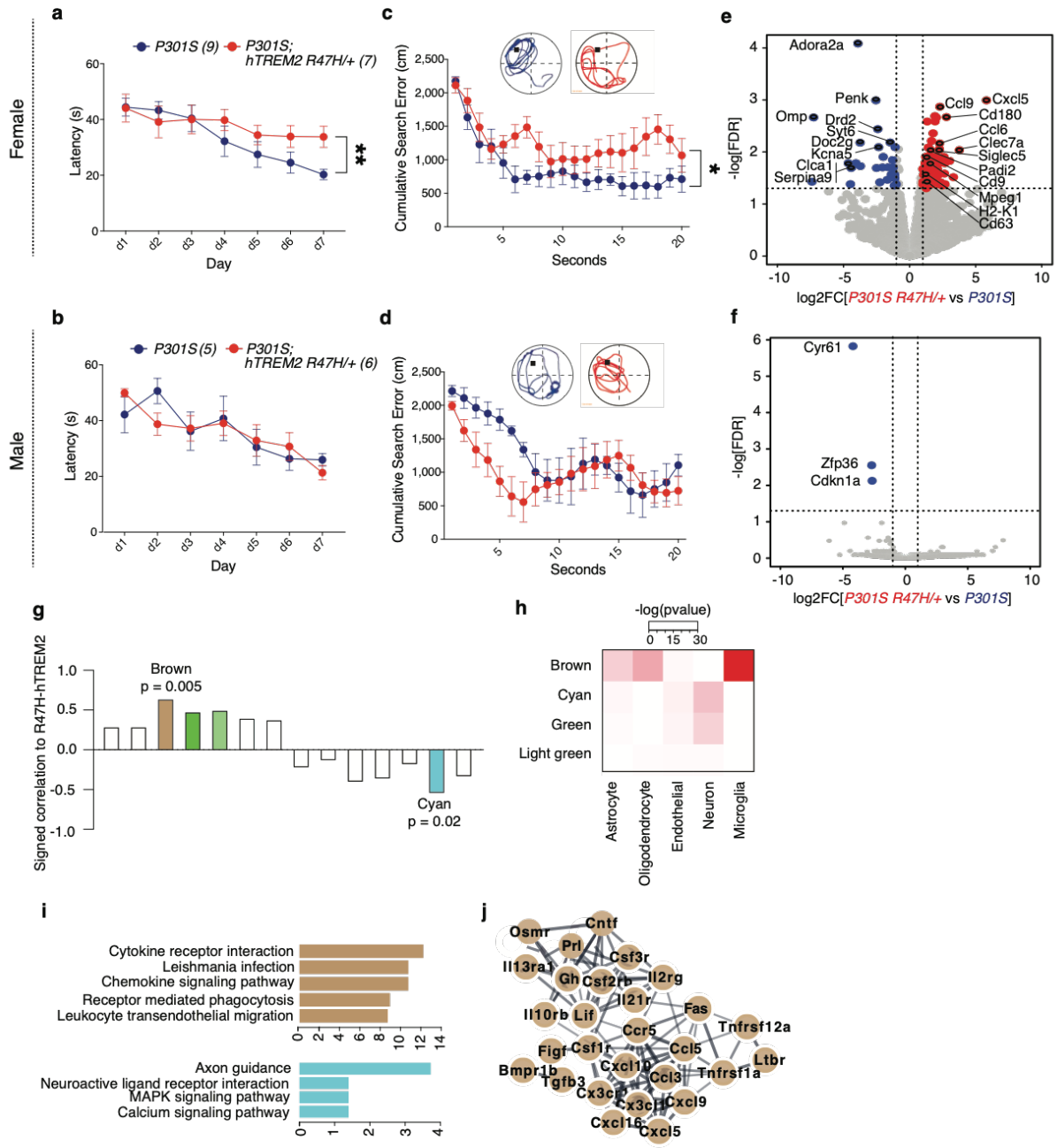

Figure 3.3 R47H-hTREM2 Exacerbates Tau-Induced Spatial Learning and Memory Deficits in Females Only

Spatial learning and memory assessment of 7–9-month-old mice using the Morris water maze.

a-b, Latency to reach the platform during hidden trials (d1-d7) was significantly greater in female P301S *hTREM2*$^{R47H/+}$ mice than in P301S littermates (**a**), but did not differ between male P301S *hTREM2*$^{R47H/+}$ mice and P301S littermates (**b**). **p=0.003, STATA mixed-effects modeling.

c-d, Cumulative search error was significantly greater in female P301S *hTREM2*$^{R47H/+}$ mice than in P301S littermates (**c**), but did not significantly differ between male P301S

hTREM2$^{R47H/+}$ mice and P301S littermates (**d**). *U=9, p=0.0164, two-tailed Mann-Whitney U-test of area under the curve. A representative search track is shown for each genotype. The black square indicates the platform location in the upper left quadrant. The four quadrants of the pool are delineated by dashed lines.

e, Volcano plot of RNA-sequencing data from bulk hippocampal tissue from 8–9-month-old female P301S *hTREM2*$^{R47H/+}$ mice and line-specific female P301S controls. Blue dots are genes with significantly higher normalized counts in P301S controls than in P301S *hTREM2*$^{R47H/+}$ samples (28 mRNAs). Red dots are genes with significantly higher normalized counts in P301S *hTREM2*$^{R47H/+}$ samples than P301S controls (94 mRNAs). Genes in red are disease-associated microglial (DAM) genes and genes involved in inflammation. Genes in blue are genes associated with neuronal function. (n = 3 mice for P301S; n = 5 mice for P301S *hTREM2*$^{R47H/+}$).

f, Volcano plot of RNA-sequencing data from bulk hippocampal tissue from male P301S *hTREM2*$^{R47H/+}$ and line-specific male P301S controls. Blue dots are genes with significantly higher normalized counts in P301S controls than *P301S hTREM2*$^{R47H/+}$ samples (3 mRNAs). (n = 2 mice for P301S; n = 5 mice for P301S *hTREM2*$^{R47H/+}$).

g, Weighted gene co-expression network analysis (WGCNA) of bulk RNA-sequencing data from (**e**) and 8–9-month-old female P301S *hTREM2*$^{WT/+}$ mice and line-specific female P301S controls. Significant modules are colored. White bars denote non-significant modules (n = 5 mice for P301S *hTREM2*$^{R47H/+}$; n = 6 mice for P301S *hTREM2*$^{WT/+}$; n = 3 mice for each P301S line-specific controls).

h, Cell-type enrichment analysis for significant WGCNA modules from (**g**).

i, Top 5 enriched KEGG (Kyoto Encyclopedia of Genes and Genomes) pathways of genes from the brown and cyan WGCNA modules in (**g**). Colors of the bars represent the WGCNA module.

j, Network analysis using STRING database on genes from the KEGG “cytokine receptor interaction” gene set of the brown module.

Values are mean ± SEM. Behavioral data represent the combination of two behavioral cohorts that were run independently. Sequencing data represent one independent sequencing experiment. For all volcano plots, the cut-offs used were $p<0.05$ with the Benjamini-Hochberg correction and log-2-fold change (log2FC) ≥ 1 or log2FC ≤ -1.

See also Supplementary Figures 5-7.

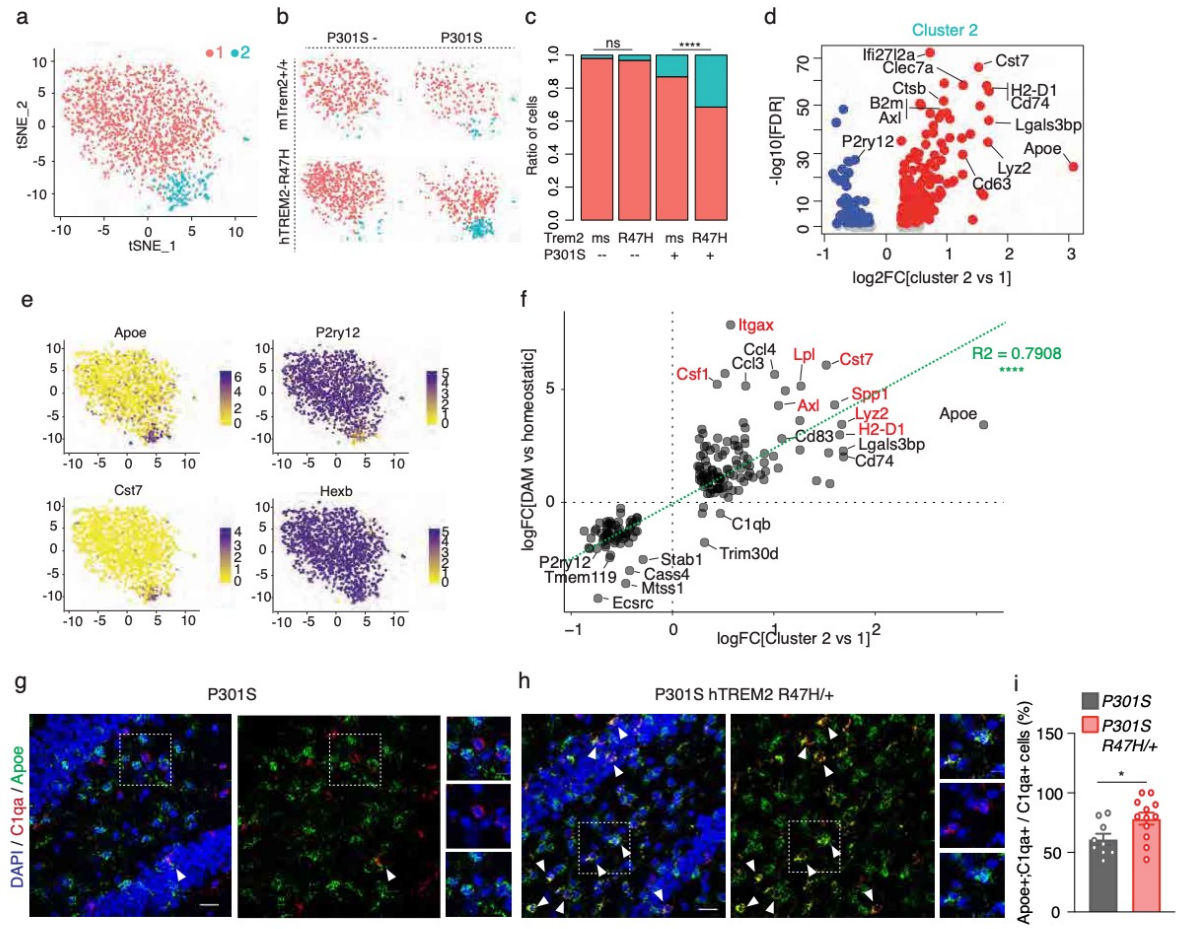

Figure 3.4 R47H-hTREM2 Increases the Disease-associated Microglia Signature in Female Tauopathy Mice.

a, t-SNE plot of all 1,424 microglial cells analyzed and clustered. (n = 2 mice/genotype, 8-month-old female mice).

b, t-SNE plots based on clustering from (**a**) split by genotype.

c, Ratio of cells in each cluster by genotype. ****p<0.0001, two-sided Fisher's exact test.

d, Volcano plot of DEGs defining cluster 2 compared to cluster 1.

e, Feature plots of transcript expression overlaid onto t-SNE of all microglial cells.

f, Correlation scatterplot of DEGs in cluster 2 vs. cluster 1 (x-axis) compared to disease-associated microglia (DAM) vs. homeostatic microglia (y-axis)[40]. R^2 = 0.7908, ****p < 2.2e-16.

g-h, RNA *in situ* (RNAscope) showing Apoe, C1qa, and DAPI signal in the dentate gyrus for P301S (**g**) and P301S *hTREM2*$^{R47H/+}$ (**h**) mice. Dashed square denotes location of insets. Arrows denote co-localization of Apoe+ and C1qa+ puncta.

i, Quantification of percentage of Apoe+ C1qa+ cells, normalized to total number of C1qa+ cells from **(g-h)**. *p<0.05 n=3 mice/genotype, 10-11-month-old female mice.

See also Supplementary Figure 8.

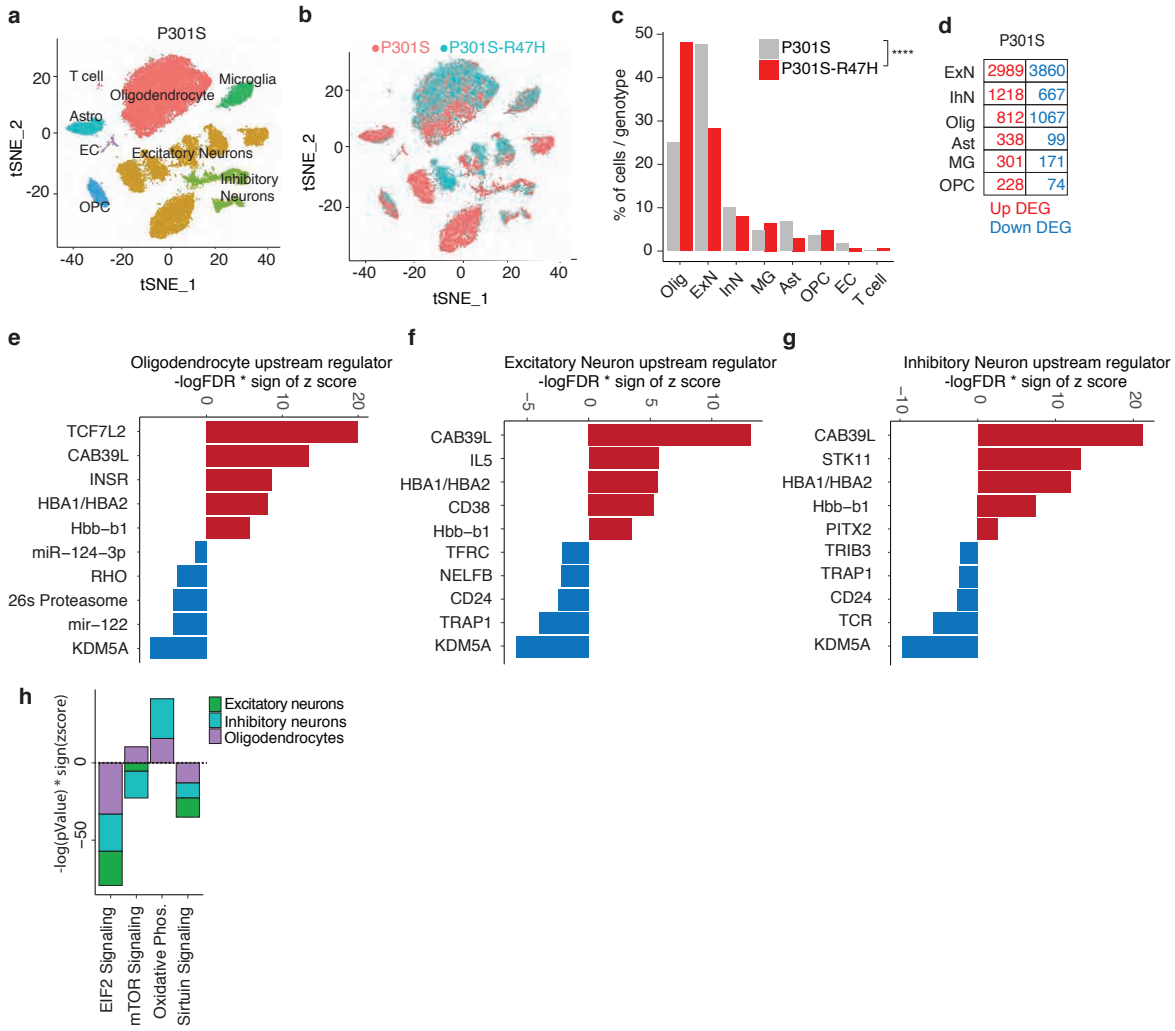

Figure 3.5 Microglial R47h-hTREM2 Induces Unique Transcriptional States in Neurons and Oligodendrocytes in Female Tauopathy Mice

a, t-SNE plots of all single nuclei and their annotated cell types from 2 each of P301S and P301S *hTREM2*$^{R47H/+}$ 9-month-old female mice.

b, t-SNE plot split by genotype.

c, Proportion of each cell type for each genotype.

d, Total number of DEGs for each cell type for P301S *hTREM2*$^{R47H/+}$ vs. P301S. FDR < 0.05.

e-g, Ingenuity pathway analysis's predicted upstream regulators for oligodendrocytes (**e**), excitatory neurons (**f**), and inhibitory neurons (**g**). Red and blue denote upstream regulators that are predicted to be activated or inhibited, respectively.

h, Ingenuity canonical pathway enrichment analysis of DEGs in P301S *hTREM2*$^{R47H/+}$ vs. P301S by specified cell type.

See also Supplementary Figure 9.

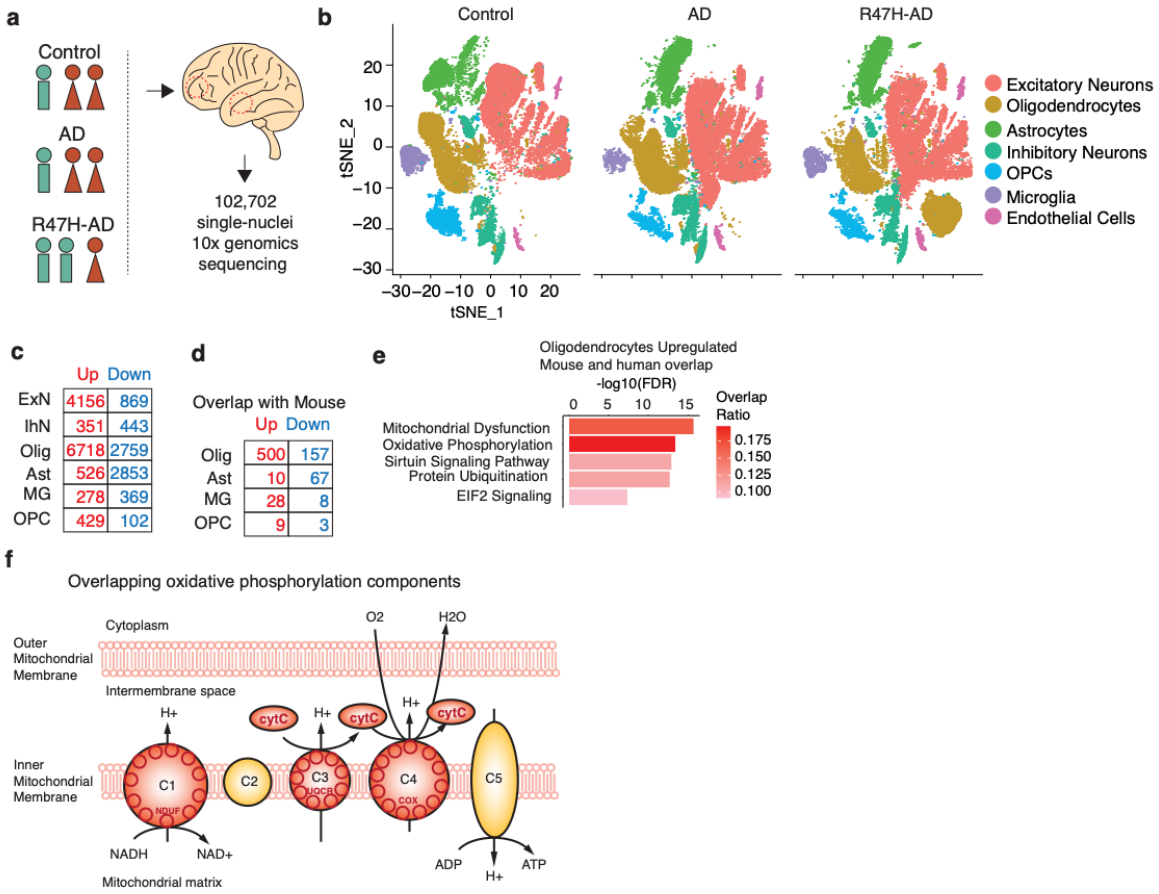

Figure 3.6 R47H-hTREM2 in Human and Mouse is Associated with Mitochondrial Changes in Oligodendrocytes

a, Schematic showing the sex and genotypes of age-matched human donors used for single-nuclei RNA-sequencing. n = 11,1185 cells from 3 control, 3 AD, and 3 R47H-AD patients; 102,702 cells were used for downstream analysis. Red and turquoise cartoons denote females and males, respectively. For each donor, a sample of brain tissue was obtained from both the temporal and frontal cortices. See also Supplementary Table 6.

b, t-SNE plots of all single nuclei and their annotated cell types from 3 control, 3 AD, and 3 R47H-AD donors plotted by genotype.

c, Number of DEGs between R47H-AD vs. AD samples for each cell type. FDR<0.05

d, Number of overlapping DEGs between R47H-AD vs. AD human and P301S-R47H vs. P301S mouse samples for glial cell types. FDR<0.05

e, Ingenuity canonical pathway enrichment analysis of overlapping upregulated oligodendrocyte DEGs found in (**d**).

f, Diagram of genes in the oxidative phosphorylation pathway found in (**e**), with red compartments representing upregulation in R47H human and mouse samples.

Data represent one independent sequencing experiment. See also Supplementary Figure 10.

3.9 Supplementary Figures

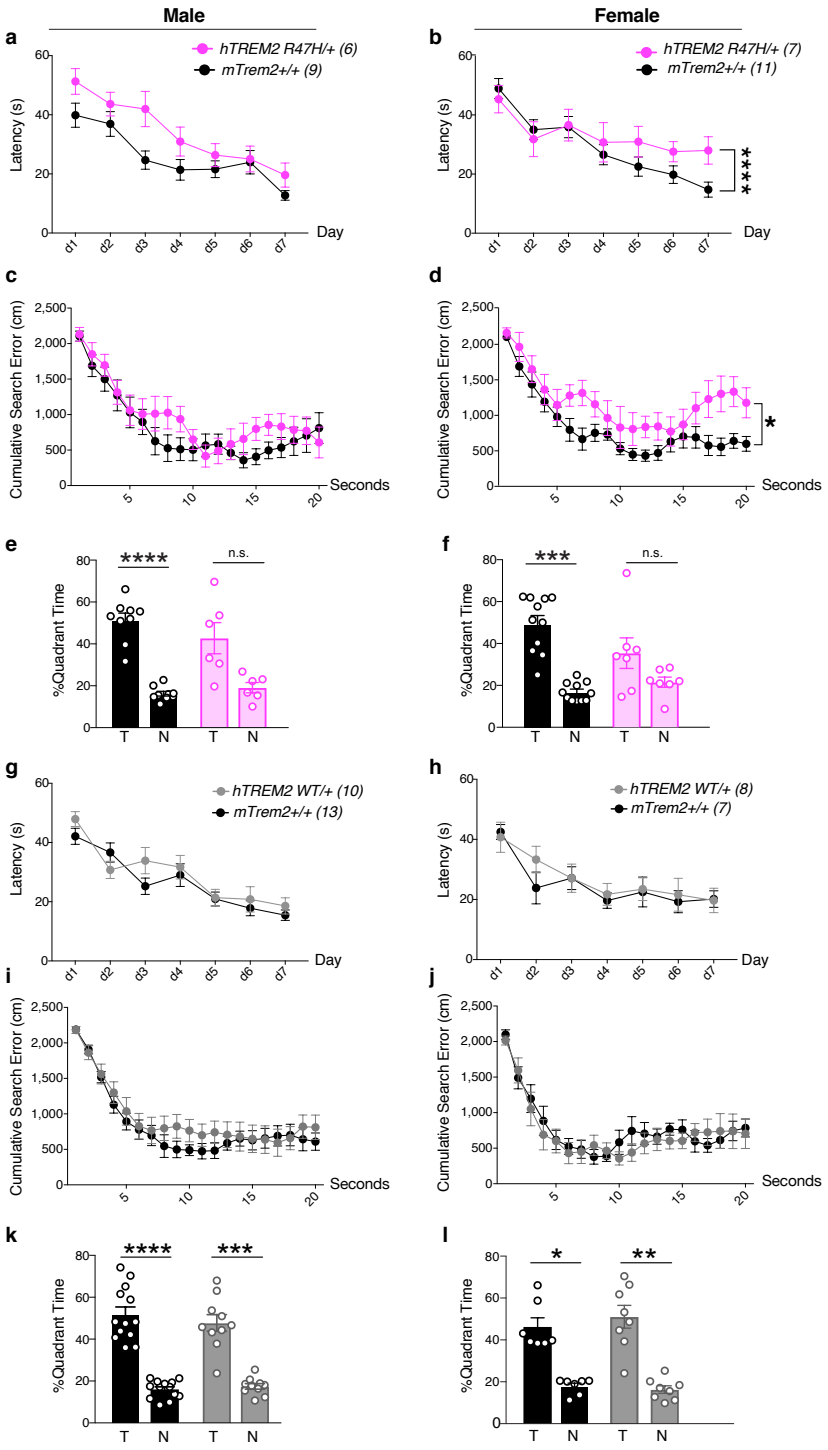

Supplementary Figure 3.1 R47H-hTREM2 Induces Spatial Learning and Memory Deficits in Female Mice (Related to Figure 1)

Morris water maze assessment of spatial learning and memory in 7–9-month-old *hTREM2*$^{R47H/+}$ *hTREM2*$^{WT/+}$ mice and littermate controls.

a-b, Latency to reach the platform during hidden trials (d1–d7) for *hTREM2*$^{R47H/+}$ males (**a**) and females (**b**) and their littermate sex-matched *mTrem2*$^{+/+}$ controls. Female *hTREM2*$^{R47H/+}$ mice exhibited greater latency to reach the platform than littermate controls, indicating impaired spatial learning. ****p=0.000, STATA mixed-effects modeling.
c-d, Cumulative search errors during the 24-hr probe trial for *hTREM2*$^{R47H/+}$ males (**c**) and females (**d**) and their littermate sex-matched *mTrem2*$^{+/+}$ controls. Female *hTREM2*$^{R47H/+}$mice had a significantly greater cumulative search error, suggesting impaired spatial memory. * U=13, p=0.0204, Two-tailed Mann-Whitney U-test of area under the curve.
e-f, Percentage of time spent in the target (T) or the average time spent in the nontarget (N) quadrants during the 24-hr probe trial for *hTREM2*$^{R47H/+}$ males (**e**) and females (**f**) and their littermate sex-matched *mTrem2*$^{+/+}$ controls. Neither male nor female *hTREM2*$^{R47H/+}$ spent significantly more time in the target quadrant compared to the nontarget quadrant, indicating impaired spatial memory. ***t=6.088, p=0.0001, ****t=7.834, p=5.077e-005, paired two-tailed Student's t-test for n>8, two-tailed Wilcoxon test for n<8.
g-h, Latency to reach the platform during hidden platform trials (d1–d7) for *hTREM2*$^{WT/+}$ males (**g**) and females (**h**) and their littermate sex-matched *mTrem2*$^{+/+}$ controls did not differ. STATA mixed-effects modeling.
i-j, Cumulative search errors during the 24-hr probe trial for *hTREM2*$^{WT/+}$ males (**i**) and females (**j**) and their littermate sex-matched *mTrem2*$^{+/+}$ controls were similar. Two-tailed Mann-Whitney U-test of area under the curve.
k-l, Percentage of time spent in the target (T) or the average time spent in the nontarget (N) quadrants during the 24-hr probe for *hTREM2*$^{WT/+}$ males (**k**) and females (**l**) and their littermate sex-matched *mTrem2*$^{+/+}$ controls. All groups spent significantly more time in the target quadrant. *W=-28, p=0.01563 (**l**), **t=4.810, p=0.001943, ***t=5.752, p=0.0002, ****t=7.503, p=7.208e-006, paired two-tailed Student's t-test for n>8, two-tailed Wilcoxon test for n<8.
Values are mean ± SEM.

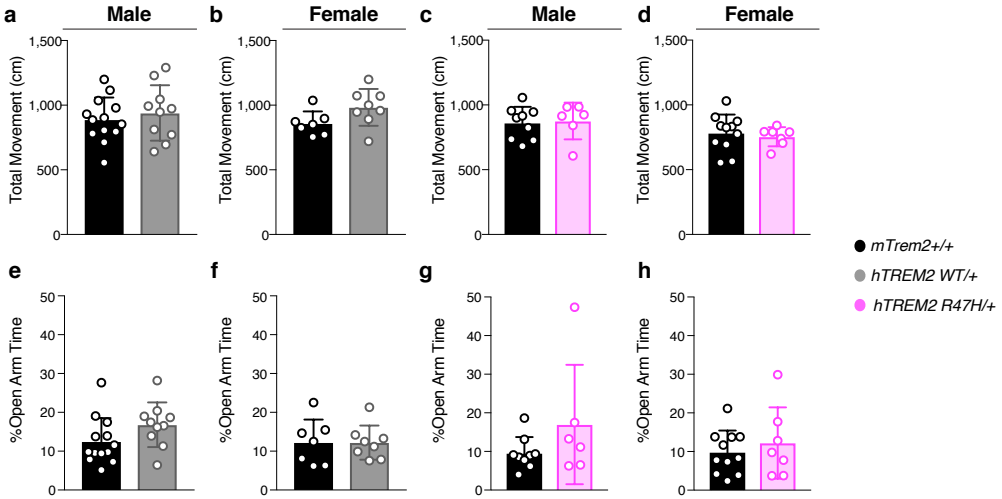

Supplementary Figure 3.2 Neither Human WT nor R47H hTREM2 Affect Overall Activity or Anxiety Levels (Related to Figure 1)

a-d, Open-field assessment of overall activity of 7–9-month-old *hTREM2*$^{WT/+}$ male (**a**) and female (**b**) mice and *hTREM2*$^{R47H/+}$ male (**c**) and female (**d**) mice and their littermate *mTrem2*$^{+/+}$ controls. Total activity was similar across all groups. Two-tailed Student's t-test for n>8, two-tailed Mann-Whitney U-test for n<8.

e-h, Elevated plus maze assessment of anxiety levels in 7–9-month-old *hTREM2*$^{WT/+}$ male (**e**) and female (**f**) mice and *hTREM2*$^{R47H/+}$ male (**g**) and female (**h**) mice and littermate *mTrem2*$^{+/+}$ controls. All groups spent a similar percentage of time in the open arms. Two-tailed Student's t-test for n>8, two-tailed Mann-Whitney U-test for n<8.

Values are mean ± SEM.

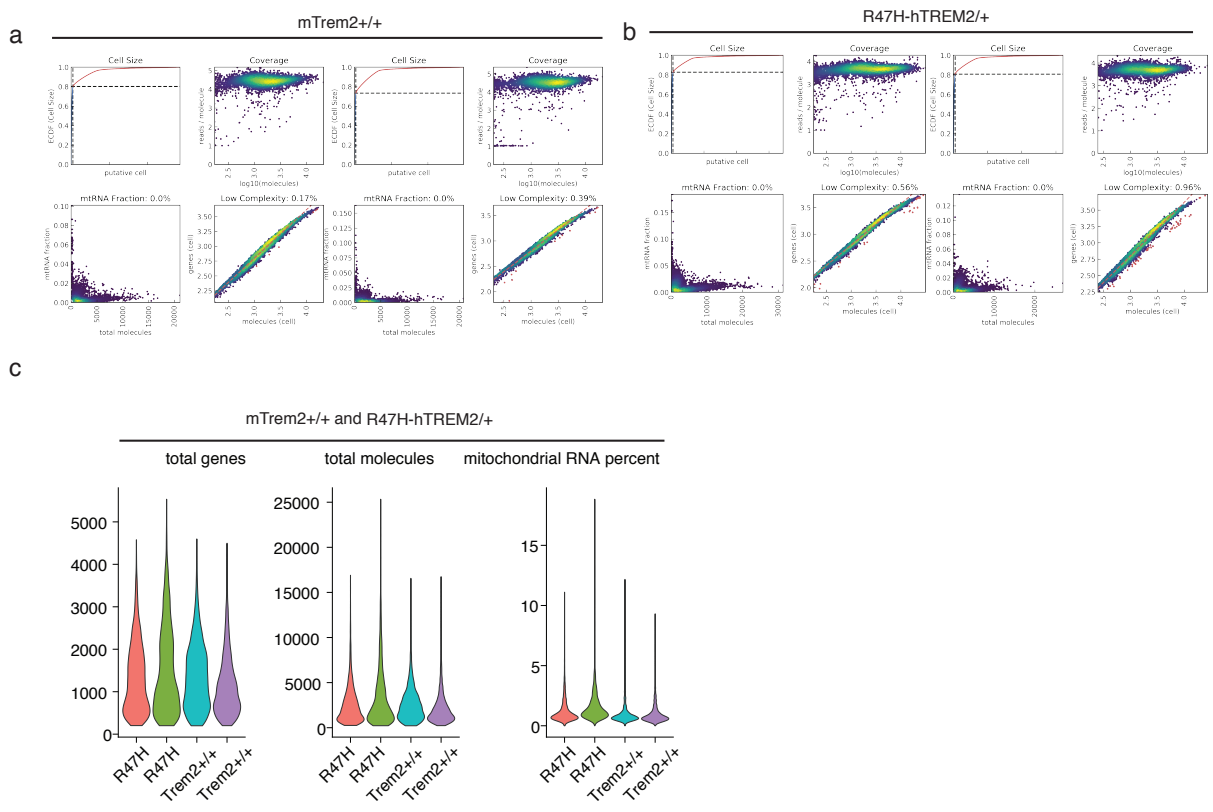

Supplementary Figure 3.3 Quality Control Assessment of Single-nuclei RNA-sequencing (Related to Figure 2)

a-b, Quality control metrics of cell size, coverage, correlation between mitochondrial RNA and total genes detected, and correlation between genes and total genes (UMI) detected for each sample. Single nuclei were isolated from 9–month-old female *mTrem2*$^{+/+}$and *hTREM2*$^{R47H/+}$ mouse hippocampal tissue for 10x Genomics single-nuclei sequencing. 31,783 cells were used for downstream analysis. (n = 2 mice/genotype).

c, Violin plots showing spread of total genes, total molecules detected, and percent of mitochondrial RNA.

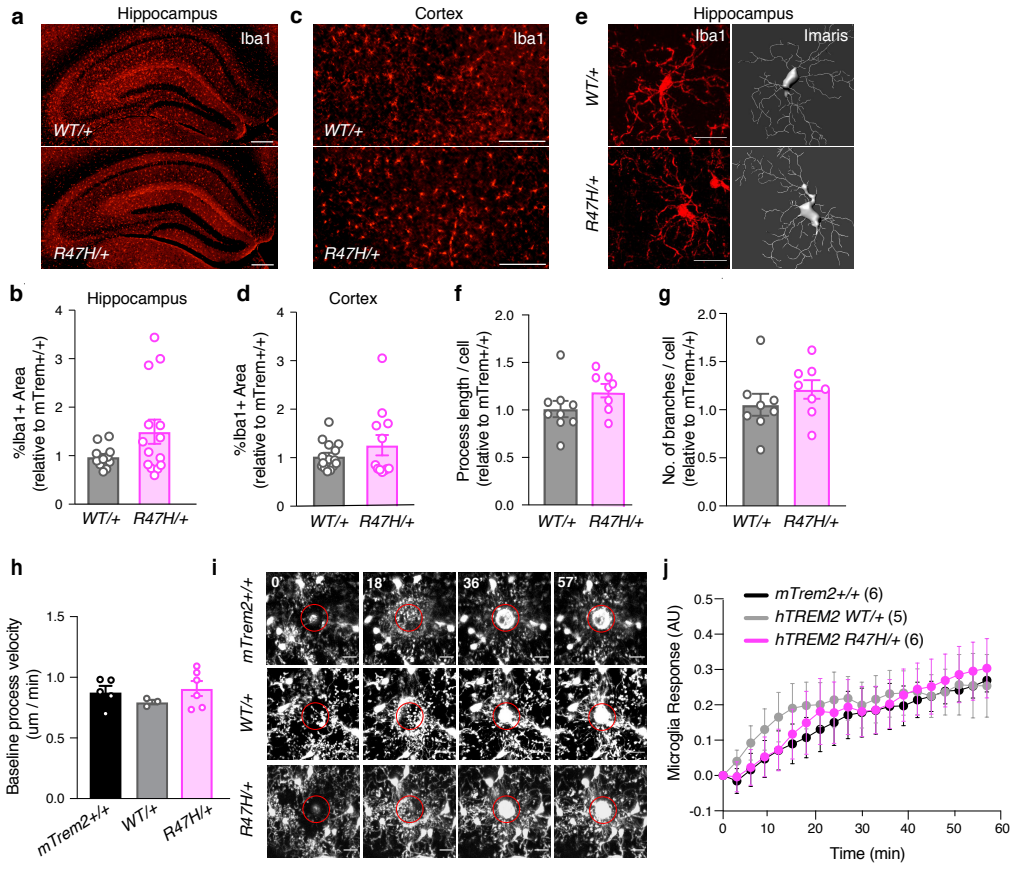

Supplementary Figure 3.4 R47H-hTREM2 Does Not Affect Microglial Morphology, Density, or Motility (Related to Figure 2)

Immunohistochemical analysis of 8–9-month-old mice. Circles in bar graphs represent data from one mouse, acquired by averaging all sections (8–10 per mouse) or microglia (~11 cells/mouse) traced for that mouse. For comparisons, data from *hTREM2*$^{WT/+}$ and *hTREM2*$^{R47H/+}$ mice were normalized to data from line-specific *mTrem2*$^{+/+}$ controls.

a, Representative images of Iba1 staining in the hippocampus.

b, Percentage of hippocampal area positive for Iba1. Entire hippocampus was quantified. Two-tailed Student's t-test.

c, Representative images of Iba1 staining in the cortex.

d, Percentage of cortical area positive for Iba1. Entire cortex was quantified. Two-tailed Student's t-test.

e, Representative images of Iba1 staining and Imaris 3D reconstruction of microglia in the CA3 hippocampal region.

f-g, Imaris quantification of total process length per cell (**f**) and number of branch points per cell for each genotype (**g**). Two-tailed student's t-test.

h, Quantification of microglial process velocity in 12-17-month-old mice during 10 min of baseline recordings (n = 5 *mTrem2*$^{+/+}$, n = 3 *hTREM2*$^{WT/+}$, n = 6 *hTREM2*$^{R47H/+}$ mice, ~25 processes/mouse). One-way ANOVA.

i, Representative images at 0, 18, 36, and 57 minutes after laser-induced injury. Red circle indicates region of injury.

j, Quantification of the normalized microglial response to focal laser-induced tissue injury for 60 min after injury. (n = 6 *mTrem2*$^{+/+}$, n = 5 *hTREM2*$^{WT/+}$, n = 6 *hTREM2*$^{R47H/+}$ mice). STATA

mixed-effects modeling.
Scale bars: hippocampus, 300 μm; cortex, 200 μm; hippocampal microglia, 20 μm, ablation, 15 μm.
Values are mean ± SEM. All data are from one independent experiment, unless otherwise noted. See also Supplementary Movie 1.

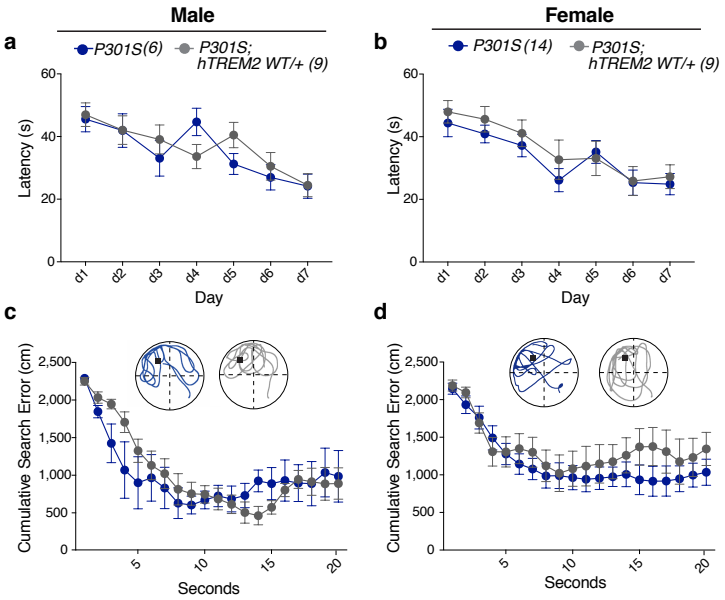

Supplementary Figure 3.5 WT-hTREM2 Phenocopies Mouse Trem2 in Tauopathy Mice (Related to Figure 3)

a-d, Latency to reach the platform during hidden trials (d1-d7) and cumulative search errors during the 72-hr probe trial did not differ significantly between male (**a,c**) and female (**b,d**) P301S and P301S *hTREM2*$^{WT/+}$ mice. A representative search track is shown for each genotype. The black square indicates the platform location in the upper left quadrant. The four quadrants of the pool are delineated by dashed lines. STATA mixed-effects modeling for **a,b**. Two-tailed Mann-Whitney U-test of area under the curve for **c,d**.

Values are mean ± SEM.

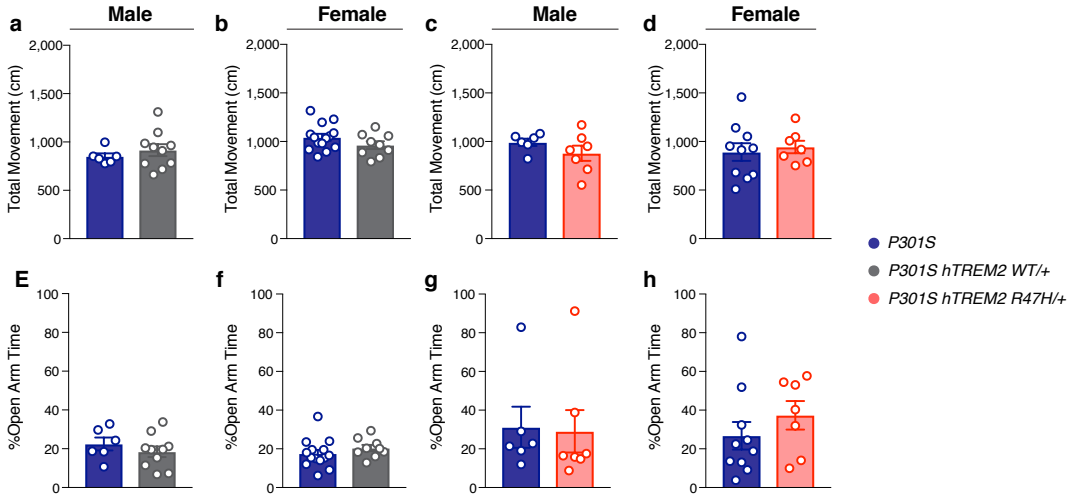

Supplementary Figure 3.6 Neither WT nor R47H hTREM2 Affect Overall Activity or Anxiety Levels in Tauopathy Mice (Related to Figure 3)

a-d, Open-field assessment of overall activity of 7–9-month-old P301S *hTREM2*$^{WT/+}$ male (**a**) and female (**b**) and P301S *hTREM2*$^{R47H/+}$ male (**c**) and female (**d**) mice and littermate P301S controls. Total activity was similar across all groups. Two-tailed Student's t-test for n>8, two-tailed Mann-Whitney U-test for n<8.

e-h, Elevated plus maze assessment of anxiety levels in 7–9-month-old *hTREM2*$^{WT/+}$ male (**e**) and female (**f**) mice and *hTREM2*$^{R47H/+}$ male (**g**) and female (**h**) mice and littermate P301S controls. All groups spent a similar percentage of time in the open arms. Two-tailed Student's t-test for n>8, two-tailed Mann-Whitney U-test for n<8.

Values are mean ± SEM.

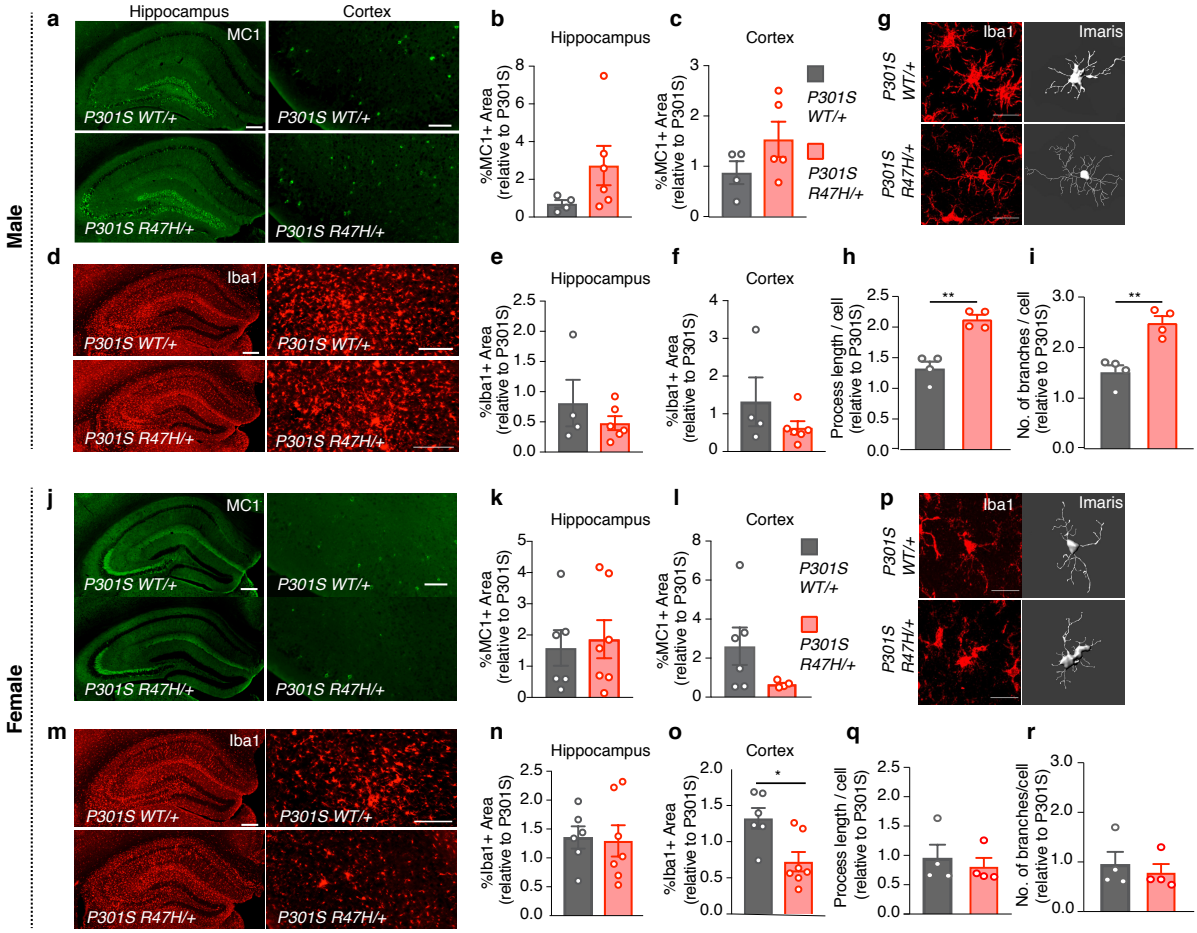

Supplementary Figure 3.7 R47H-hTREM2 Has Sex-Dependent Effects on Tau Load and Microgliosis in Tauopathy Mice (Related to Figure 3)

Immunohistochemical analysis of 8–9-month-old mice. In bar graphs, points represent the average of 8–10 sections per mouse, unless otherwise noted. Values are normalized to line-specific, sex-matched P301S *mTrem2*$^{+/+}$ littermate controls.

a and j, Representative images of MC1 immunostaining in the hippocampus and entorhinal cortex of male (**a**) and female (**j**) mice.

b,c,k,l, Percentage of MC1+ area in male hippocampus (**b**) and cortex (**c**) and female hippocampus (**k**) and cortex (**l**) of P301S *hTREM2*$^{WT/+}$ and P301S *hTREM2*$^{R47H/+}$ mice. Entire hippocampus and entire cortex were quantified. Two-tailed Mann-Whitney U-test.

d and m, Representative images of Iba1 immunostaining in the hippocampus and entorhinal cortex of male (**d**) and female (**m**) mice.

e,f,n,o, Percentage of Iba1+ area in male hippocampus (**e**) and cortex (**f**) and female hippocampus (**n**) and cortex (**o**) of P301S *hTREM2*$^{WT/+}$ and P301S *hTREM2*$^{R47H/+}$ mice. The percentage of Iba1+ area was significantly reduced in female P301S *hTREM2*$^{R47H/+}$ mice. Entire hippocampus and entire cortex were quantified. *U=4, p=0.0140, two-tailed Mann-Whitney U-test.

g and p, Representative Iba1 staining of CA3 hippocampal microglial cells and Imaris 3D reconstruction in males (**g**) and females (**p**) of P301S *hTREM2*$^{WT/+}$ and P301S *hTREM2*$^{R47H/+}$ mice.

h,i,q,r, Imaris-based automatic quantification of total process length per cell in male (**h**) and

female (**q**) P301S *hTREM2*$^{WT/+}$ and P301S *hTREM2*$^{R47H/+}$ mice and number of branch points per cell in male (**i**) and female (**r**) mice of those two genotypes. Microglia from male P301S *hTREM2*$^{R47H/+}$ had significantly longer processes (**h**) and more branch points (**i**) than controls. ** p = 0.0015, t = 6.097 (h), ** p = 0.0023, t = 5.064 (i), two-tailed, unpaired t-test with Welch's correction. Puncta represent the average of ~11 microglia/mouse. Scale bars: hippocampus, 300 μm; cortex, 200 μm; hippocampal microglia, 20 μm.
Values are mean ± SEM. Data represent the combination of two independent experiments.

a

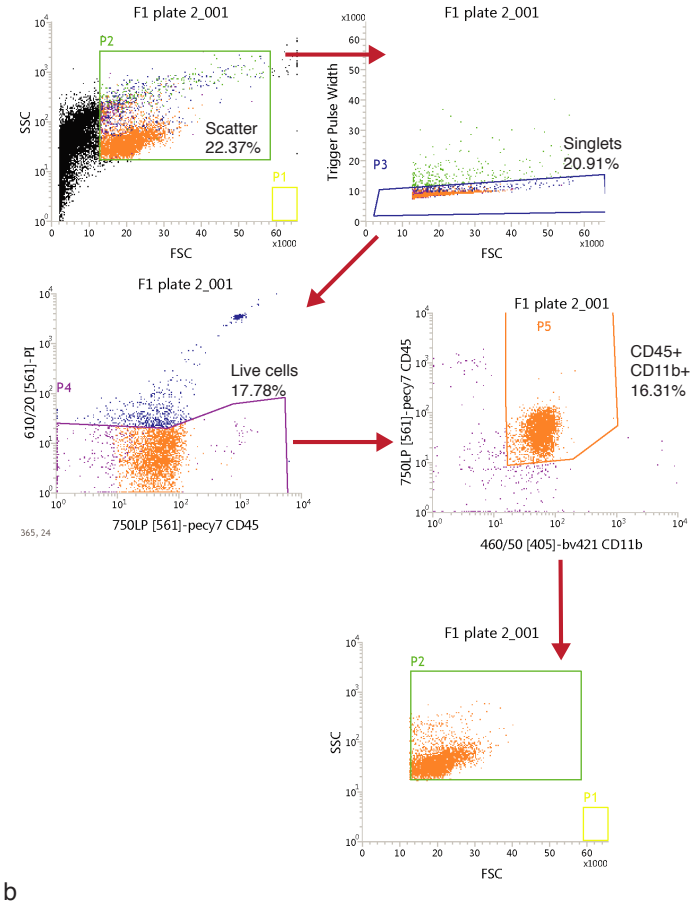

b

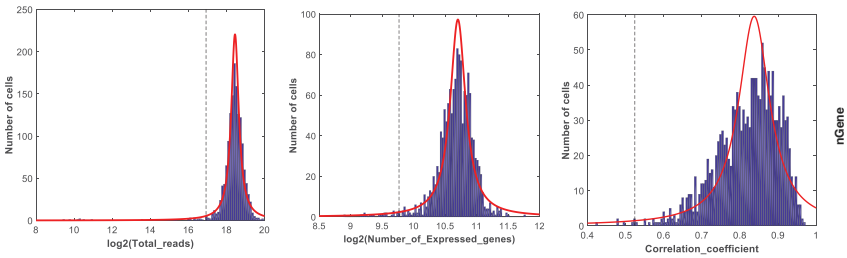

c

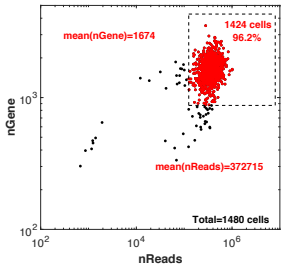

d

Single Cells	Sequenced	Passed QC
msTrem2	549	535
hTREM2-R47H/+	365	352
P301S; msTrem2	187	175
P301S; hTREM2-R47H/+	373	359
Subtotal	1480	1424

Supplementary Figure 3.8 Deep Single-Cell RNA-Sequencing of Microglia from Mouse Hippocampal Tissue (Related to Figure 4)
a, FACs gating strategy for microglia sorting.
b, Distributions for different quality control metrics.
c, Correlation between number of reads and number of genes detected, used to identify final 1424 cells used for analysis.
d, Table denoting for each sample, the number of cells sequenced and number of cells that passed quality control and were included in the final analysis.

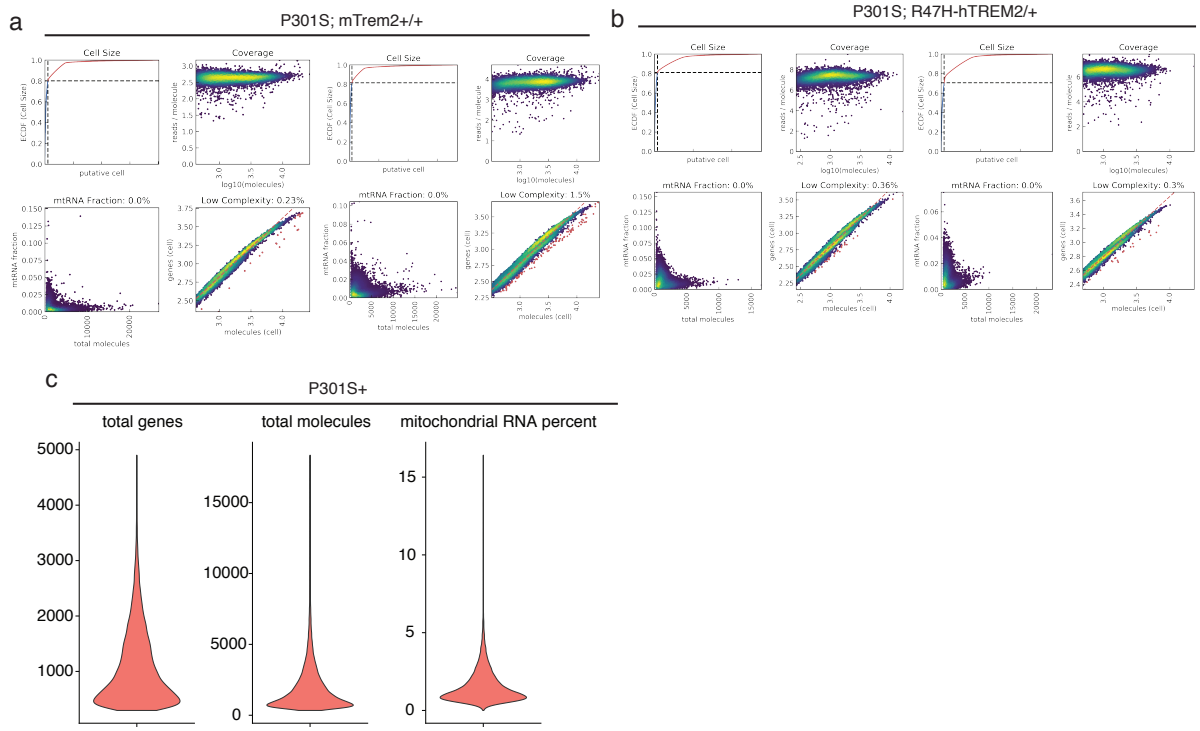

Supplementary Figure 3.9 Quality Control Assessment of Single-nuclei RNA-sequencing from Tauopathy Mouse Hippocampal Tissue (Related to Figure 5)

a-b, Quality control metrics of cell size, coverage, correlation between mitochondrial RNA and total genes detected, and correlation between genes and total genes (UMI) detected for each sample. Single nuclei were isolated from 9–month-old female P301S and P301S *hTREM2*$^{R47H/+}$ mouse hippocampal tissue for 10x Genomics single-nuclei sequencing. 31,783 cells were used for downstream analysis. (n = 2 mice/genotype).

c, Violin plots showing spread of total genes, total molecules detected, and percent of mitochondrial RNA.

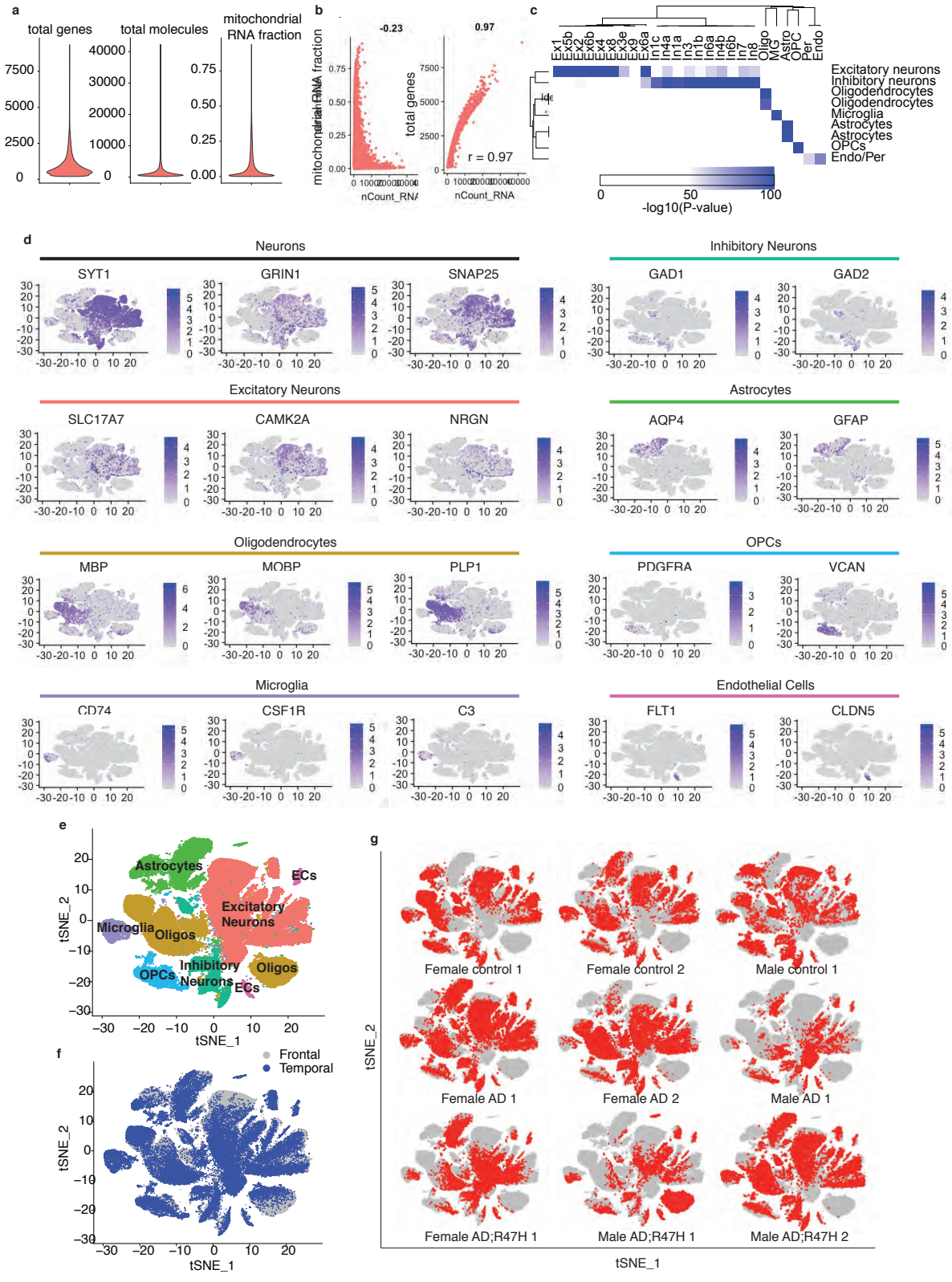
a
total genes
total molecules
mitochondrial RNA fraction
b
-0.23
0.97
mitochondrial RNA fraction
total genes
r = 0.97
nCount_RNA
c
Excitatory neurons
Inhibitory neurons
Oligodendrocytes
Oligodendrocytes
Microglia
Astrocytes
Astrocytes
OPCs
Endo/Per
-log10(P-value)
d
Neurons
SYT1
GRIN1
SNAP25
Inhibitory Neurons
GAD1
GAD2
Excitatory Neurons
SLC17A7
CAMK2A
NRGN
Astrocytes
AQP4
GFAP
Oligodendrocytes
MBP
MOBP
PLP1
OPCs
PDGFRA
VCAN
Microglia
CD74
CSF1R
C3
Endothelial Cells
FLT1
CLDN5
e
Astrocytes
ECs
Excitatory Neurons
Microglia
Oligos
Inhibitory Neurons
OPCs
Oligos
ECs
tSNE_1
tSNE_2
f
Frontal
Temporal
tSNE_1
tSNE_2
g
Female control 1
Female control 2
Male control 1
Female AD 1
Female AD 2
Male AD 1
Female AD;R47H 1
Male AD;R47H 1
Male AD;R47H 2
tSNE_1
tSNE_2

Supplementary Figure 3.10 Single-Nuclei RNA-Sequencing of Human Cortical Tissue (Related to Figure 6)
a, Violin plots of quality control metrics for sequencing.
b, Correlation scatterplot of quality control metrics for sequencing.
c, Overrepresentation analysis between cluster marker genes identified for each cell type in this dataset (rows) and published marker genes (columns) (Lake et al. 2018, Wang et al. 2018) (PsychENCODE). p-values have been adjusted for multiple hypothesis testing (-log10 (Bonferroni corrected p values) are shown).
d, Feature plots showing expression of cell type marker genes for each cell type.
e, t-SNE plot of all single nuclei and their annotated cell types (n = 102,702 cells) from 3 control, 3 AD and 3 R47H-AD donors
f, t-SNE plot of all single nuclei and their brain region locations.
g, t-SNE plots of single nuclei showing cells from each donor (red) overlaid on all cells analyzed (gray).

3.10 Legend for Supplementary Movie

Supplementary Movie 3.1 R47H-hTREM2 Does Not Affect Microglial Response to Injury (Related to Figure 2)

Video file of microglial responses of 12-17-month-old *Cx3cr1*$^{GFP/+}$ *mTrem2*$^{+/+}$, *hTREM2*$^{WT/+}$, and *hTREM2*$^{R47H/+}$ mice to an acute laser-induced injury *in vivo* over a 60-min time period, played one after the other. Scale bar: 15 μm.

Chapter 4: Discussion and Future Directions

4.1 Questions Remaining about Basic Trem2 Biology

Despite 6 years of research since the identification of the R47H AD-risk variant, little is known about Trem2 biology in the brain and how it is altered by the R47H variant. The field has been plagued by contradictory findings in different mouse models and many unresolved puzzles. While studies have attempted to address some of the contradictions (i.e. by proposing that Trem2's effects on pathology are time-sensitive), many observations remain a mystery.

Several questions about basic Trem2 biology are unresolved. These include Trem2's spatial localization in the brain, whether Trem2 levels are developmentally regulated, and its heterogeneous expression in microglial populations in the healthy brain. Studies in human and mouse tissue suggest that Trem2 is differentially expressed across the brain, with the highest Trem2 expression predominantly in the white matter and basal ganglia[24,34,35]. Why is Trem2 upregulated in these regions? Trem2 binds components of myelin[41]. Does its upregulation in the white matter pertain to the high density of myelin in this region? Despite its abundant expression in the basal ganglia, we have yet to understand the consequences of Trem2 deficiency on this brain region. In the context of pathology, studies have found region-specific effects of Trem2 on amyloid pathology[33,41,51]. Are these region-specific effects due to Trem2's putative regional distribution in the parenchyma, rendering certain areas more sensitive to low Trem2 levels? More careful characterizations of Trem2 expression in the brain throughout the lifespan of a mouse and human in health and disease are needed to solidify Trem2's spatial localization and the consequences of this regional specificity on brain function.

Trem2 appears to be developmentally downregulated, such that Trem2 is barely detectable at baseline in the healthy mouse brain[30,31,35]. Moreover, only small subset of microglia expresses Trem2 at baseline[31]. What are the roles of these rare Trem2+ microglia in the healthy brain and where are they located? What is the signal that increases microglial

Trem2 expression during disease? Through transcriptomic and proteomic studies of these Trem2+ microglia in the healthy brain, particularly in the human brain, we may unravel key Trem2 functions during homeostasis that could serve as therapeutic targets. Moreover, we can identify transcripts and signaling pathways that regulate Trem2 and that are regulated by Trem2, which would improve our understanding of Trem2 biology and how it regulates chemotaxis, cell survival, proliferation, phagocytosis, inflammation, and synapse pruning in the brain.

4.2 Questions Remaining about Trem2 Biology in the Context of Alzheimer's Disease

In addition to understanding these fundamental aspects of Trem2 biology, unraveling the ramifications of Trem2-deficient and Trem2-mutant microglia in disease models is also needed to advance our understanding of Trem2 biology. Given the low levels of Trem2 expression in the healthy brain, it may be challenging to uncover its function without presenting the brain with a challenge that relies on Trem2 signaling. Yet, we were able to observe synaptic and behavioral deficits in heterozygous R47H-hTREM2 mice in the absence of any other genetic manipulations or challenges. These findings indicate that this mutation is detrimental enough on its own over time, despite the reported low baseline levels of Trem2 expression in microglia. Moreover, they highlight the importance of this gene such that a single amino acid mutation in its ligand-binding domain causes global non-cell autonomous effects, ultimately resulting in cognitive deficits.

Trem2 deficiency reduces microgliosis and protects again tau-induced degeneration, while increasing amyloid-associated neurite toxicity[41,46,51,55,61,70,82,84]. Does Trem2 indeed have opposing effects on tau and amyloid load? Do these opposing effects result in opposing functional outcomes, i.e. cognitive deficits? Future studies looking at the consequences of Trem2 deficiency and R47H-Trem2 at multiple time points throughout disease progression could address the prevailing hypothesis that Trem2's differential effects on tau and amyloid are due to the different times at which these pathologies arise. In addition, studies aimed at unraveling the

effects of Trem2 in a mouse model that expresses both amyloid and tau pathology may help shed light on what occurs in AD patients who have both forms of protein aggregates. Would Trem2 preferentially exacerbate the accumulation of one aggregate over the other, or would it affect both aggregates the same way, or show no effect on aggregate load? More importantly, what would the functional consequences be? Very few studies have utilized functional assays and have instead relied on tau or amyloid load as a proxy for toxicity. However, protein aggregates may not reflect actual toxicity. In Huntington's disease, for example, neuronal inclusions are considered a protective mechanism – a way for neurons to sequester protein aggregates to reduce their toxicity[85]. In tauopathy mice, Trem2 deficiency protects against cortical degeneration, but has no effect on tau load[46,61], demonstrating a disconnect between tau burden and toxicity. Thus, future studies should incorporate functional readouts, such as survival curves, electrophysiology, and behavior, to directly interrogate the pathogenicity of Trem2 deficiency in amyloid and tau models.

Based on work presented in chapter three, understanding how Trem2 regulates crosstalk between microglia, oligodendrocytes, and neurons may shed light on R47H's toxicity. Are microglia communicating directly to oligodendrocytes, neurons, or both? sTREM2 staining is found on neurons[26,33], and is reduced in the R47H-TREM2 mice[33], suggesting that Trem2 may signal to neurons directly and that this signaling is likely disrupted in R47H-TREM2 mice. Neuronal binding of sTREM2 may be because the neurons are unhealthy and therefore have exposed phosphatidylserine on the cell surface, which is a known ligand for Trem2. However, the nuclei of sTrem2+ neurons appear healthy[33], suggesting that neurons express an unknown sTrem2 receptor. Future studies aimed at more carefully characterizing the health of sTrem2+ neurons and identifying potential sTrem2 receptors on neurons will be key. Furthermore, it is unclear why R47H-hTREM2 binds poorly to neurons. Overall TREM2 levels are similar between wild-type and R47H-hTREM2, indicating that similar amounts of TREM2 are available to be shed. Moreover, it is shed as effectively as wild-type human TREM2 *in vitro*[33], but perhaps

shedding is impaired *in vivo*. It may be that mutant sTREM2 binds more weakly to neurons, and therefore less mutant sTREM2 is present on neurons at a single point in time. Or perhaps it binds just as effectively as wild-type hTREM2, but is degraded faster. This striking observation will require further work to unravel.

Trem2-regulated microglial communication with other cell types may occur through other signaling molecules aside from sTrem2. Characterizing the microglia secretome (molecules released by microglia to communicate with their surroundings) in wild-type, Trem2-deficient, and R47H-hTREM2 mice may help to identify how this crosstalk is occurring, and how the secretome is modified by the R47H variant. Moreover, transcriptomic profiling sTrem2+ and sTrem2- neurons may help us understand how sTrem2 affects neuronal function beyond its role in synapse pruning during development[58,59], and may shed light on the increased synaptic transmission we observed in the R47h-hTREM2 mice. As Trem2 is part of the microglial sensome (microglial molecules used to detect endogenous ligands and microbes)[28], it may impact expression of other microglial sensome markers through its downstream signaling cascades. Profiling the microglial sensome in Trem2-deficient and R47H-Trem2 microglia can highlight Trem2-regulated pathways in microglia that are dysregulated in R47H-carriers.

Microglia, as the phagocytes of the brain, take up myelin debris and secrete factors that promote differentiation of oligodendrocyte precursor cells (OPCs) and subsequent migration to the site of injury and remyelination[45]. Studies suggest that Trem2 is important for myelin cleanup and remyelination[45,86]. Yet, the underlying signaling mechanisms are unknown. Moreover, it is unclear whether Trem2 can regulate OPC differentiation or migration, which could also contribute to exacerbated disease progression in Trem2-deficient mouse models of demyelination.

The R47H variant is purported to be a partial loss-of-function mutation[33,36,37,40,42,44,78]. This hypothesis is primarily based off of R47H-Trem2's impairment in ligand-binding. Moreover, these studies compared R47H-overexpressing microglia to Trem2-deficient microglia, when it is

R47H heterozygosity that increases risk for AD. Thus, studies are needed to determine whether R47H is simply a loss-of-function, or whether it may also exhibit gain-of-function phenotypes such as binding to ectopic ligands or increased downstream signaling. Preliminary work from our R47H-hTREM2 and WT-hTREM2 mice suggests that R47H-hTREM2 microglia increase expression of the disease-associated microglia (DAM) signature, which is downregulated in Trem2-deficient microglia[62]. This finding suggests a gain-of-function effect of the mutation with respect to DAM genes. To more accurately determine whether R47H causes gain-of-function effects, phosphoproteomics of R47H heterozygous microglia and Trem2-haploinsufficient microglia could identify whether any signaling pathways that are downregulated in Trem2-haploinsufficient microglia are upregulated in R47H-hTREM2.

Like R47H-TREM2, ApoE4 is also a single amino acid change compared to its counterpart ApoE3, which is not a risk factor for AD. The TREM2 field may benefit from observing how the ApoE4 field identified its pathogenicity. One important note that has not been addressed in the field is the presence of Trem3. In humans, Trem3 is a pseudogene. However, in mice, Trem3 is functional. In the periphery, it associates with Dap12 and promotes macrophage activation[87]. Its function in the brain is unknown. If Trem3 phenocopies Trem2, then this redundancy may explain why Trem2 knockout mice do not recapitulate hallmarks of Nasu-Hakola disease, even at old age[45]. A better understanding of Trem3 function may be required to determine whether we need to remove Trem3 from mouse models in order to unmask hidden phenotypes in Trem2-deficient or Trem2-mutant microglia.

Lastly, the field has been slowed down by the use of different mutant and knockout Trem2 mouse models that were recently found to exhibit different artifacts from the way the lines were generated (i.e. the cryptic splice site in R47H mouse Trem2[83], or significant upregulation of Trem-like genes[88]). These artifacts likely, in part, contribute to the contradictory findings related to Trem2's roles in health and disease. The field may benefit from focusing its efforts on the mouse model that most closely mimics the human condition. To do this, more

research is needed on Trem2 expression and function in both healthy and diseased human brain tissue. Once the field adopts a consistent mouse model, reproducibility will hopefully increase and we will unravel more key insights into Trem2 function and dysfunction, and consequently microglia function and dysfunction, in health and disease.

Chapter 5: Conclusion

R47H-TREM2 increases risk for AD and several neurodegenerative diseases, but it does not cause any of them. Indeed, causal mutations for Nasu-Hakola disease that result in complete lack of Trem2 exhibit dramatic phenotypes, creating non-functional or truncated proteins that fail to mature and reach the cell surface. R47H-TREM2, on the other hand, is able to mature normally and be expressed at the cell surface. This suggests that R47H-TREM2's toxic effects in the brain may be small, but as the toxicity accumulates in the brain over many decades, it may tip the brain into a state of vulnerability for disease. Thus, unraveling the mystery behind this risk variant's strong association with AD may require aging for the accumulated deficits to manifest in a mouse, or challenges to speed up the process of accumulation and uncover deficits earlier on. Overall, the most promising findings in the field so far implicate Trem2 in lipid sensing, plaque compaction, and allowing microglia to shift from homeostatic to reactive in response to stimuli. Our work highlights the importance of studying Trem2 haploinsufficient mice, as they do not always phenocopy Trem2 deficient mice – potentially due to compensation from Trem3 or other microglial genes. Our work also shows that R47H-hTREM2 is sufficient to cause synaptic and cognitive abnormalities along with significant transcriptional changes in neurons and oligodendrocytes that may underlie these deficits.

This is just the beginning. The better we understand this key microglial gene with pleiotropic functions, the more insight we will have into the ways in which microglial dysfunction exacerbates disease pathogenesis. Future work profiling the brains of R47H-AD carriers will be critical in order to identify dysregulated pathways to focus on. These pathways can then be dissected mechanistically using animal models and used to identify therapeutic targets not only for R47H-carriers, but for AD patients in general.

References for Chapters 1, 4 and 5

1 Gaugler, J. *et al.* 2019 Alzheimer's disease facts and figures. *Alzheimers Dement* **15**, 321-387, doi:10.1016/j.jalz.2019.01.010 (2019).

2 Alzheimer, A., Stelzmann, R. A., Schnitzlein, H. N. & Murtagh, F. R. An English translation of Alzheimer's 1907 paper, "Uber eine eigenartige Erkankung der Hirnrinde". *Clin Anat* **8**, 429-431, doi:10.1002/ca.980080612 (1995).

3 Nimmerjahn, A., Kirchhoff, F. & Helmchen, F. Resting microglial cells are highly dynamic surveillants of brain parenchyma in vivo. *Science* **308**, 1314-1318, doi:1110647 [pii] 10.1126/science.1110647 (2005).

4 Davalos, D. *et al.* ATP mediates rapid microglial response to local brain injury in vivo. *Nat Neurosci* **8**, 752-758, doi:10.1038/nn1472 (2005).

5 Butovsky, O. & Weiner, H. L. Microglial signatures and their role in health and disease. *Nat Rev Neurosci* **19**, 622-635, doi:10.1038/s41583-018-0057-5 (2018).

6 Schafer, D. P. *et al.* Microglia sculpt postnatal neural circuits in an activity and complement-dependent manner. *Neuron* **74**, 691-705, doi:10.1016/j.neuron.2012.03.026 (2012).

7 Paolicelli, R. C. *et al.* Synaptic pruning by microglia is necessary for normal brain development. *Science* **333**, 1456-1458, doi:10.1126/science.1202529 (2011).

8 Zhan, Y. *et al.* Deficient neuron-microglia signaling results in impaired functional brain connectivity and social behavior. *Nat Neurosci* **17**, 400-406, doi:10.1038/nn.3641 (2014).

9 Parkhurst, C. N. *et al.* Microglia promote learning-dependent synapse formation through brain-derived neurotrophic factor. *Cell* **155**, 1596-1609, doi:10.1016/j.cell.2013.11.030 (2013).

10 Ginhoux, F. *et al.* Fate mapping analysis reveals that adult microglia derive from primitive macrophages. *Science* **330**, 841-845, doi:science.1194637 [pii] 10.1126/science.1194637 [doi] (2010).

11 Ransohoff, R. M. & Cardona, A. E. The myeloid cells of the central nervous system parenchyma. *Nature* **468**, 253-262, doi:10.1038/nature09615 (2010).

12 Zhan, L. *et al.* Proximal recolonization by self-renewing microglia re-establishes microglial homeostasis in the adult mouse brain. *PLoS Biol* **17**, e3000134, doi:10.1371/journal.pbio.3000134 (2019).

13 Condello, C., Yuan, P., Schain, A. & Grutzendler, J. Microglia constitute a barrier that prevents neurotoxic protofibrillar Abeta42 hotspots around plaques. *Nat Commun* **6**, 6176, doi:10.1038/ncomms7176 (2015).

14 Wes, P. D., Sayed, F. A., Bard, F. & Gan, L. Targeting microglia for the treatment of Alzheimer's Disease. *Glia* **64**, 1710-1732, doi:10.1002/glia.22988 (2016).

15 Efthymiou, A. G. & Goate, A. M. Late onset Alzheimer's disease genetics implicates microglial pathways in disease risk. *Mol Neurodegener* **12**, 43, doi:10.1186/s13024-017-0184-x (2017).

16 Sims, R. *et al.* Rare coding variants in PLCG2, ABI3, and TREM2 implicate microglial-mediated innate immunity in Alzheimer's disease. *Nat Genet* **49**, 1373-1384, doi:10.1038/ng.3916 (2017).

17 Guerreiro, R. *et al.* TREM2 variants in Alzheimer's disease. *N Engl J Med* **368**, 117-127, doi:10.1056/NEJMoa1211851 (2013).

18 Jonsson, T. *et al.* Variant of TREM2 associated with the risk of Alzheimer's disease. *N Engl J Med* **368**, 107-116, doi:10.1056/NEJMoa1211103 (2013).

19 Strittmatter, W. J. *et al.* Apolipoprotein E: high-avidity binding to beta-amyloid and increased frequency of type 4 allele in late-onset familial Alzheimer disease. *Proc Natl Acad Sci U S A* **90**, 1977-1981 (1993).

20 Saunders, A. M. *et al.* Association of apolipoprotein E allele epsilon 4 with late-onset familial and sporadic Alzheimer's disease. *Neurology* **43**, 1467-1472, doi:10.1212/wnl.43.8.1467 (1993).

21 Ruiz, A. *et al.* Assessing the role of the TREM2 p.R47H variant as a risk factor for Alzheimer's disease and frontotemporal dementia. *Neurobiol Aging* **35**, 444 e441-444, doi:10.1016/j.neurobiolaging.2013.08.011 (2014).

22 Hamerman, J. A. *et al.* Cutting edge: inhibition of TLR and FcR responses in macrophages by triggering receptor expressed on myeloid cells (TREM)-2 and DAP12. *J Immunol* **177**, 2051-2055, doi:10.4049/jimmunol.177.4.2051 (2006).

23 Daws, M. R., Lanier, L. L., Seaman, W. E. & Ryan, J. C. Cloning and characterization of a novel mouse myeloid DAP12-associated receptor family. *Eur J Immunol* **31**, 783-791, doi:10.1002/1521-4141(200103)31:3<783::AID-IMMU783gt;3.0.CO;2-U (2001).

24 Forabosco, P. *et al.* Insights into TREM2 biology by network analysis of human brain gene expression data. *Neurobiol Aging* **34**, 2699-2714, doi:10.1016/j.neurobiolaging.2013.05.001 (2013).

25 Turnbull, I. R. *et al.* Cutting edge: TREM-2 attenuates macrophage activation. *J Immunol* **177**, 3520-3524 (2006).

26 Hsieh, C. L. *et al.* A role for TREM2 ligands in the phagocytosis of apoptotic neuronal cells by microglia. *J Neurochem* **109**, 1144-1156, doi:10.1111/j.1471-4159.2009.06042.x (2009).

27 Takahashi, K., Rochford, C. D. & Neumann, H. Clearance of apoptotic neurons without inflammation by microglial triggering receptor expressed on myeloid cells-2. *J Exp Med* **201**, 647-657, doi:10.1084/jem.20041611 (2005).

28 Hickman, S. E. *et al.* The microglial sensome revealed by direct RNA sequencing. *Nat Neurosci* **16**, 1896-1905, doi:nn.3554 [pii] 10.1038/nn.3554 (2013).

29 Butovsky, O. *et al.* Identification of a unique TGF-beta-dependent molecular and functional signature in microglia. *Nat Neurosci* **17**, 131-143, doi:10.1038/nn.3599 (2014).

30 Jay, T. R. *et al.* TREM2 deficiency eliminates TREM2+ inflammatory macrophages and ameliorates pathology in Alzheimer's disease mouse models. *J Exp Med* **212**, 287-295, doi:10.1084/jem.20142322 (2015).

31 Lee, C. Y. D. *et al.* Elevated TREM2 Gene Dosage Reprograms Microglia Responsivity and Ameliorates Pathological Phenotypes in Alzheimer's Disease Models. *Neuron* **97**, 1032-1048 e1035, doi:10.1016/j.neuron.2018.02.002 (2018).

32 Sessa, G. *et al.* Distribution and signaling of TREM2/DAP12, the receptor system mutated in human polycystic lipomembraneous osteodysplasia with sclerosing leukoencephalopathy dementia. *Eur J Neurosci* **20**, 2617-2628, doi:10.1111/j.1460-9568.2004.03729.x (2004).

33 Song, W. M. *et al.* Humanized TREM2 mice reveal microglia-intrinsic and -extrinsic effects of R47H polymorphism. *J Exp Med* **215**, 745-760, doi:10.1084/jem.20171529 (2018).

34 Paloneva, J. *et al.* Mutations in two genes encoding different subunits of a receptor signaling complex result in an identical disease phenotype. *Am J Hum Genet* **71**, 656-662, doi:10.1086/342259 (2002).

35 Chertoff, M., Shrivastava, K., Gonzalez, B., Acarin, L. & Gimenez-Llort, L. Differential modulation of TREM2 protein during postnatal brain development in mice. *PLoS One* **8**, e72083, doi:10.1371/journal.pone.0072083 (2013).

36 Atagi, Y. *et al.* Apolipoprotein E Is a ligand for triggering receptor expressed on myeloid cells 2 (TREM2). *J Biol Chem* **290**, 26043-26050, doi:10.1074/jbc.M115.679043 (2015).

37 Bailey, C. C., DeVaux, L. B. & Farzan, M. The triggering receptor expressed on myeloid cells 2 binds apolipoprotein E. *J Biol Chem* **290**, 26033-26042, doi:10.1074/jbc.M115.677286 (2015).

38 Daws, M. R. *et al.* Pattern recognition by TREM-2: binding of anionic ligands. *J Immunol* **171**, 594-599, doi:10.4049/jimmunol.171.2.594 (2003).

39 Kawabori, M. *et al.* Triggering receptor expressed on myeloid cells 2 (TREM2) deficiency attenuates phagocytic activities of microglia and exacerbates ischemic damage in experimental stroke. *J Neurosci* **35**, 3384-3396, doi:10.1523/JNEUROSCI.2620-14.2015 (2015).

40 Kober, D. L. *et al.* Neurodegenerative disease mutations in TREM2 reveal a functional surface and distinct loss-of-function mechanisms. *Elife* **5**, doi:10.7554/eLife.20391 (2016).

41 Wang, Y. *et al.* TREM2 lipid sensing sustains the microglial response in an Alzheimer's disease model. *Cell* **160**, 1061-1071, doi:10.1016/j.cell.2015.01.049 (2015).

42 Yeh, F. L., Wang, Y., Tom, I., Gonzalez, L. C. & Sheng, M. TREM2 binds to apolipoproteins, including APOE and CLU/APOJ, and thereby facilitates uptake of amyloid-beta by microglia. *Neuron* **91**, 328-340, doi:10.1016/j.neuron.2016.06.015 (2016).

43 Zhao, Y. *et al.* TREM2 is a receptor for beta-amyloid that mediates microglial function. *Neuron* **97**, 1023-1031 e1027, doi:10.1016/j.neuron.2018.01.031 (2018).

44 Zhong, L. *et al.* Amyloid-beta modulates microglial responses by binding to the triggering receptor expressed on myeloid cells 2 (TREM2). *Mol Neurodegener* **13**, 15, doi:10.1186/s13024-018-0247-7 (2018).

45 Poliani, P. L. *et al.* TREM2 sustains microglial expansion during aging and response to demyelination. *J Clin Invest* **125**, 2161-2170, doi:10.1172/JCI77983 (2015).

46 Sayed, F. A. *et al.* Differential effects of partial and complete loss of TREM2 on microglial injury response and tauopathy. *Proc Natl Acad Sci USA* **115**, 10172-10177, doi:10.1073/pnas.1811411115 (2018).

47 Mazaheri, F. *et al.* TREM2 deficiency impairs chemotaxis and microglial responses to neuronal injury. *EMBO Rep* **18**, 1186-1198, doi:10.15252/embr.201743922 (2017).

48 Takahashi, K., Prinz, M., Stagi, M., Chechneva, O. & Neumann, H. TREM2-transduced myeloid precursors mediate nervous tissue debris clearance and facilitate recovery in an animal model of multiple sclerosis. *PLoS Med* **4**, e124, doi:10.1371/journal.pmed.0040124 (2007).

49 N'Diaye, E. N. *et al.* TREM-2 (triggering receptor expressed on myeloid cells 2) is a phagocytic receptor for bacteria. *J Cell Biol* **184**, 215-223, doi:10.1083/jcb.200808080 (2009).

50 Kleinberger, G. *et al.* TREM2 mutations implicated in neurodegeneration impair cell surface transport and phagocytosis. *Sci Transl Med* **6**, 243ra286, doi:10.1126/scitranslmed.3009093 (2014).

51 Jay, T. R. *et al.* Disease progression-dependent effects of TREM2 deficiency in a mouse model of Alzheimer's Disease. *J Neurosci* **37**, 637-647, doi:10.1523/JNEUROSCI.2110-16.2016 (2017).

52 Zheng, H. *et al.* TREM2 promotes microglial survival by activating wnt/beta-catenin pathway. *J Neurosci* **37**, 1772-1784, doi:10.1523/JNEUROSCI.2459-16.2017 (2017).

53 Otero, K. *et al.* TREM2 and beta-catenin regulate bone homeostasis by controlling the rate of osteoclastogenesis. *J Immunol* **188**, 2612-2621, doi:10.4049/jimmunol.1102836 (2012).

54 Mosher, K. I. & Wyss-Coray, T. Microglial dysfunction in brain aging and Alzheimer's disease. *Biochem Pharmacol* **88**, 594-604, doi:S0006-2952(14)00032-X [pii] 10.1016/j.bcp.2014.01.008 (2014).

55 Wang, Y. *et al.* TREM2-mediated early microglial response limits diffusion and toxicity of amyloid plaques. *J Exp Med* **213**, 667-675, doi:10.1084/jem.20151948 (2016).

56 Zhong, L. *et al.* Soluble TREM2 induces inflammatory responses and enhances microglial survival. *J Exp Med* **214**, 597-607, doi:10.1084/jem.20160844 (2017).

57 Erblich, B., Zhu, L., Etgen, A. M., Dobrenis, K. & Pollard, J. W. Absence of colony stimulation factor-1 receptor results in loss of microglia, disrupted brain development and olfactory deficits. *PLoS One* **6**, e26317, doi:10.1371/journal.pone.0026317 (2011).

58 Filipello, F. *et al.* The microglial innate iImmune receptor TREM2 is required for synapse elimination and normal brain connectivity. *Immunity* **48**, 979-991 e978, doi:10.1016/j.immuni.2018.04.016 (2018).

59 Jay, T. R. *et al.* TREM2 is required for microglial instruction of astrocytic synaptic engulfment in neurodevelopment. *Glia* **67**, 1873-1892, doi:10.1002/glia.23664 (2019).

60 Linnartz-Gerlach, B. *et al.* TREM2 triggers microglial density and age-related neuronal loss. *Glia* **67**, 539-550, doi:10.1002/glia.23563 (2019).

61 Leyns, C. E. G. *et al.* TREM2 deficiency attenuates neuroinflammation and protects against neurodegeneration in a mouse model of tauopathy. *Proc Natl Acad Sci USA* **114**, 11524-11529, doi:10.1073/pnas.1710311114 (2017).

62 Keren-Shaul, H. *et al.* A unique microglia type associated with restricting development of Alzheimer's Disease. *Cell* **169**, 1276-1290 e1217, doi:10.1016/j.cell.2017.05.018 (2017).

63 Borroni, B. *et al.* Heterozygous TREM2 mutations in frontotemporal dementia. *Neurobiol Aging* **35**, 934 e937-910, doi:10.1016/j.neurobiolaging.2013.09.017 (2014).

64 Cady, J. *et al.* TREM2 variant p.R47H as a risk factor for sporadic amyotrophic lateral sclerosis. *JAMA Neurol* **71**, 449-453, doi:10.1001/jamaneurol.2013.6237 (2014).

65 Guerreiro, R. & Hardy, J. TREM2 and neurodegenerative disease. *N Engl J Med* **369**, 1569-1570 (2013).

66 Rayaprolu, S. *et al.* TREM2 in neurodegeneration: evidence for association of the p.R47H variant with frontotemporal dementia and Parkinson's disease. *Mol Neurodegener* **8**, 19, doi:10.1186/1750-1326-8-19 (2013).

67 Paloneva, J. *et al.* CNS manifestations of Nasu-Hakola disease: a frontal dementia with bone cysts. *Neurology* **56**, 1552-1558, doi:10.1212/wnl.56.11.1552 (2001).

68 Nasu, T., Tsukahara, Y. & Terayama, K. A lipid metabolic disease-"membranous lipodystrophy"-an autopsy case demonstrating numerous peculiar membrane-structures composed of compound lipid in bone and bone marrow and various adipose tissues. *Acta Pathol Jpn* **23**, 539-558, doi:10.1111/j.1440-1827.1973.tb01223.x (1973).

69 Ulrich, J. D. *et al.* Altered microglial response to Abeta plaques in APPPS1-21 mice heterozygous for TREM2. *Mol Neurodegener* **9**, 20, doi:10.1186/1750-1326-9-20 (2014).

70 Yuan, P. *et al.* TREM2 Haplodeficiency in Mice and Humans Impairs the Microglia Barrier Function Leading to Decreased Amyloid Compaction and Severe Axonal Dystrophy. *Neuron* **90**, 724-739, doi:10.1016/j.neuron.2016.05.003 (2016).

71 Ulland, T. K. *et al.* TREM2 maintains microglial metabolic fitness in Alzheimer's Disease. *Cell* **170**, 649-663 e613, doi:10.1016/j.cell.2017.07.023 (2017).

72 Krasemann, S. *et al.* The TREM2-APOE pathway drives the transcriptional phenotype of dysfunctional microglia in neurodegenerative diseases. *Immunity* **47**, 566-581, doi:10.1016/j.immuni.2017.08.008 (2017).

73 Yuan, P. *et al.* TREM2 Haplodeficiency in Mice and Humans Impairs the Microglia Barrier Function Leading to Decreased Amyloid Compaction and Severe Axonal Dystrophy. *Neuron* **92**, 252-264, doi:10.1016/j.neuron.2016.09.016 (2016).

74 Bemiller, S. M. *et al.* TREM2 deficiency exacerbates tau pathology through dysregulated kinase signaling in a mouse model of tauopathy. *Mol Neurodegener* **12**, 74, doi:10.1186/s13024-017-0216-6 (2017).

75 Prinz, M., Priller, J., Sisodia, S. S. & Ransohoff, R. M. Heterogeneity of CNS myeloid cells and their roles in neurodegeneration. *Nat Neurosci* **14**, 1227-1235, doi:10.1038/nn.2923 (2011).

76 Perry, V. H., Nicoll, J. A. & Holmes, C. Microglia in neurodegenerative disease. *Nat Rev Neurol* **6**, 193-201, doi:10.1038/nrneurol.2010.17 (2010).

77 Song, W. *et al.* Alzheimer's disease-associated TREM2 variants exhibit either decreased or increased ligand-dependent activation. *Alzheimers Dement* **13**, 381-387, doi:10.1016/j.jalz.2016.07.004 (2017).

78 Sudom, A. *et al.* Molecular basis for the loss-of-function effects of the Alzheimer's disease-associated R47H variant of the immune receptor TREM2. *J Biol Chem* **293**, 12634-12646, doi:10.1074/jbc.RA118.002352 (2018).

79 Park, J. S., Ji, I. J., Kim, D. H., An, H. J. & Yoon, S. Y. The Alzheimer's Disease-Associated R47H Variant of TREM2 Has an Altered Glycosylation Pattern and Protein Stability. *Front Neurosci* **10**, 618, doi:10.3389/fnins.2016.00618 (2016).

80 Cheng, Q. *et al.* TREM2-activating antibodies abrogate the negative pleiotropic effects of the Alzheimer's disease variant Trem2(R47H) on murine myeloid cell function. *J Biol Chem* **293**, 12620-12633, doi:10.1074/jbc.RA118.001848 (2018).

81 Ma, L. *et al.* Expression and processing analyses of wild type and p.R47H TREM2 variant in Alzheimer's disease brains. *Mol Neurodegener* **11**, 72, doi:10.1186/s13024-016-0137-9 (2016).

82 Cheng-Hathaway, P. J. *et al.* The Trem2 R47H variant confers loss-of-function-like phenotypes in Alzheimer's disease. *Mol Neurodegener* **13**, 29, doi:10.1186/s13024-018-0262-8 (2018).

83 Xiang, X. *et al.* The Trem2 R47H Alzheimer's risk variant impairs splicing and reduces Trem2 mRNA and protein in mice but not in humans. *Mol Neurodegener* **13**, 49, doi:10.1186/s13024-018-0280-6 (2018).

84 Audrain, M. *et al.* Integrative approach to sporadic Alzheimer's disease: deficiency of TYROBP in a tauopathy mouse model reduces C1q and normalizes clinical phenotype

while increasing spread and state of phosphorylation of tau. *Mol Psychiatry*, doi:10.1038/s41380-018-0258-3 (2018).

85 Arrasate, M., Mitra, S., Schweitzer, E. S., Segal, M. R. & Finkbeiner, S. Inclusion body formation reduces levels of mutant huntingtin and the risk of neuronal death. *Nature* **431**, 805-810, doi:10.1038/nature02998 (2004).

86 Piccio, L. *et al.* Blockade of TREM-2 exacerbates experimental autoimmune encephalomyelitis. *Eur J Immunol* **37**, 1290-1301, doi:10.1002/eji.200636837 (2007).

87 Colonna, M. TREMs in the immune system and beyond. *Nat Rev Immunol* **3**, 445-453, doi:10.1038/nri1106 (2003).

88 Kang, S. S. *et al.* Behavioral and transcriptomic analysis of Trem2-null mice: not all knockout mice are created equal. *Hum Mol Genet*, doi:10.1093/hmg/ddx366 (2017).

Publishing Agreement

It is the policy of the University to encourage the distribution of all theses, dissertations, and manuscripts. Copies of all UCSF theses, dissertations, and manuscripts will be routed to the library via the Graduate Division. The library will make all theses, dissertations, and manuscripts accessible to the public and will preserve these to the best of their abilities, in perpetuity.

Please sign the following statement:

I hereby grant permission to the Graduate Division of the University of California, San Francisco to release copies of my thesis, dissertation, or manuscript to the Campus Library to provide access and preservation, in whole or in part, in perpetuity.

DocuSigned by:
Faten Sayed
78AC61EFB32B401...
Author Signature

10/28/2019
Date